

In the Matter of:

Entergy Nuclear Operations, Inc.  
(Indian Point Nuclear Generating Units 2 and 3)



**ASLBP #:** 07-858-03-LR-BD01  
**Docket #:** 05000247 | 05000286  
**Exhibit #:** NYS00490A-00-BD01  
**Admitted:** 11/5/2015  
**Rejected:**  
**Other:**

**Identified:** 11/5/2015  
**Withdrawn:**  
**Stricken:**

**NYS000490A**

**Submitted: June 9, 2015**



NUREG/CR-6909, Rev. 1  
ANL-12/60

# Effect of LWR Coolant Environments on the Fatigue Life of Reactor Materials

Draft Report for Comment



## AVAILABILITY OF REFERENCE MATERIALS IN NRC PUBLICATIONS

### NRC Reference Material

As of November 1999, you may electronically access NUREG-series publications and other NRC records at NRC's Public Electronic Reading Room at <http://www.nrc.gov/reading-rm.html>. Publicly released records include, to name a few, NUREG-series publications; *Federal Register* notices; applicant, licensee, and vendor documents and correspondence; NRC correspondence and internal memoranda; bulletins and information notices; inspection and investigative reports; licensee event reports; and Commission papers and their attachments.

NRC publications in the NUREG series, NRC regulations, and Title 10, "Energy," in the *Code of Federal Regulations* may also be purchased from one of these two sources.

1. The Superintendent of Documents  
U.S. Government Printing Office Mail Stop SSOP  
Washington, DC 20402-0001  
Internet: [bookstore.gpo.gov](http://bookstore.gpo.gov)  
Telephone: 202-512-1800  
Fax: 202-512-2250
2. The National Technical Information Service  
Springfield, VA 22161-0002  
[www.ntis.gov](http://www.ntis.gov)  
1-800-553-6847 or, locally, 703-605-6000

A single copy of each NRC draft report for comment is available free, to the extent of supply, upon written request as follows:

Address: U.S. Nuclear Regulatory Commission  
Office of Administration  
Publications Branch  
Washington, DC 20555-0001

E-mail: [DISTRIBUTION.RESOURCE@NRC.GOV](mailto:DISTRIBUTION.RESOURCE@NRC.GOV)  
Facsimile: 301-415-2289

Some publications in the NUREG series that are posted at NRC's Web site address <http://www.nrc.gov/reading-rm/doc-collections/nuregs> are updated periodically and may differ from the last printed version. Although references to material found on a Web site bear the date the material was accessed, the material available on the date cited may subsequently be removed from the site.

### Non-NRC Reference Material

Documents available from public and special technical libraries include all open literature items, such as books, journal articles, transactions, *Federal Register* notices, Federal and State legislation, and congressional reports. Such documents as theses, dissertations, foreign reports and translations, and non-NRC conference proceedings may be purchased from their sponsoring organization.

Copies of industry codes and standards used in a substantive manner in the NRC regulatory process are maintained at—

The NRC Technical Library  
Two White Flint North  
11545 Rockville Pike  
Rockville, MD 20852-2738

These standards are available in the library for reference use by the public. Codes and standards are usually copyrighted and may be purchased from the originating organization or, if they are American National Standards, from—

American National Standards Institute  
11 West 42<sup>nd</sup> Street  
New York, NY 10036-8002  
[www.ansi.org](http://www.ansi.org)  
212-642-4900

Legally binding regulatory requirements are stated only in laws; NRC regulations; licenses, including technical specifications; or orders, not in NUREG-series publications. The views expressed in contractor-prepared publications in this series are not necessarily those of the NRC.

The NUREG series comprises (1) technical and administrative reports and books prepared by the staff (NUREG-XXXX) or agency contractors (NUREG/CR-XXXX), (2) proceedings of conferences (NUREG/CP-XXXX), (3) reports resulting from international agreements (NUREG/IA-XXXX), (4) brochures (NUREG/BR-XXXX), and (5) compilations of legal decisions and orders of the Commission and Atomic and Safety Licensing Boards and of Directors' decisions under Section 2.206 of NRC's regulations (NUREG-0750).

**DISCLAIMER:** This report was prepared as an account of work sponsored by an agency of the U.S. Government. Neither the U.S. Government nor any agency thereof, nor any employee, makes any warranty, expressed or implied, or assumes any legal liability or responsibility for any third party's use, or the results of such use, of any information, apparatus, product, or process disclosed in this publication, or represents that its use by such third party would not infringe privately owned rights.

# Effect of LWR Coolant Environments on the Fatigue Life of Reactor Materials

## Draft Report for Comment

Manuscript Completed: March 2014  
Date Published: March 2014

Prepared by:  
Omesh Chopra<sup>1</sup> and Gary L. Stevens<sup>2</sup>

<sup>1</sup>Argonne National Laboratory  
9700 South Cass Avenue  
Argonne, IL 60439

<sup>2</sup>U.S. Nuclear Regulatory Commission

G. Stevens, NRC Project Manager

NRC Job Codes V6069 & V6269

Office of Nuclear Regulatory Research

## COMMENTS ON DRAFT REPORT

Any interested party may submit comments on this report for consideration by the NRC staff. Comments may be accompanied by additional relevant information or supporting data. Please specify the report number **NUREG/CR-6909 Rev. 1** in your comments, and send them by the end of the comment period specified in the *Federal Register* notice announcing the availability of this report.

**Addresses:** You may submit comments by any one of the following methods. Please include Docket ID **NRC-2014-0023** in the subject line of your comments. Comments submitted in writing or in electronic form will be posted on the NRC website and on the Federal rulemaking website <http://www.regulations.gov>.

**Federal Rulemaking Website:** Go to <http://www.regulations.gov> and search for documents filed under Docket ID **NRC-2014-0023**. Address questions about NRC dockets to Carol Gallagher at 301-287-3422 or by e-mail at [Carol.Gallagher@nrc.gov](mailto:Carol.Gallagher@nrc.gov).

**Mail comments to:** Cindy Bladey, Chief, Rules, Announcements, and Directives Branch (RADB), Division of Administrative Services, Office of Administration, Mail Stop: 3WFN-06-A44MP, U.S. Nuclear Regulatory Commission, Washington, DC 20555-0001. Faxes may be sent to RADB at 301-287-9368.

For any questions about the material in this report, please contact: Gary L. Stevens, Senior Materials Engineer at (301) 251-7569 or by e-mail at [Gary.Stevens@nrc.gov](mailto:Gary.Stevens@nrc.gov).

Please be aware that any comments that you submit to the NRC will be considered a public record and entered into the Agencywide Documents Access and Management System (ADAMS). Do not provide information you would not want to be publicly available.

## Abstract

The ASME Boiler and Pressure Vessel Code provides rules for the design of Class 1 components of nuclear power plants. Figures I–9.1 through I–9.6 of Appendix I to Section III of the Code specify fatigue design curves for applicable structural materials. However, the effects of light water reactor (LWR) coolant environments are not explicitly addressed by the Code design curves. The existing fatigue strain–vs.–life ( $\epsilon$ – $N$ ) data illustrate potentially significant effects of LWR coolant environments on the fatigue resistance of pressure vessel and piping steels. Under certain environmental and loading conditions, fatigue lives in water relative to those in air can be a factor of approximately 12 lower for austenitic stainless steels, approximately 3 lower for Ni-Cr-Fe alloys, and approximately 17 lower for carbon and low-alloy steels. In 2007, the original version of NUREG/CR-6909, which is the technical basis document for NRC Regulatory Guide 1.207, summarized the work performed at Argonne National Laboratory on the fatigue of piping and pressure vessel steels in LWR environments. In that document, the existing fatigue  $\epsilon$ – $N$  data were evaluated to identify the various material, environmental, and loading parameters that influence fatigue crack initiation, and to establish the effects of key parameters on the fatigue lives of these steels. The report presented fatigue life models for estimating fatigue lives as a function of material, loading, and environmental conditions, and described the environmental fatigue correction factor,  $F_{en}$ , for incorporating the effects of LWR environments into ASME Section III fatigue evaluations. The report also presented a critical review of the ASME Code Section III fatigue adjustment factors of 2 on stress (or strain) and 20 on life and assessed the possible conservatism in the choice of these adjustment factors.

This report provides updates and improvements to the environmental fatigue correction factor approach based on an extensive update to the fatigue  $\epsilon$ – $N$  data from testing and results available over the past decade since this report was first published. The updated expressions also address concerns from interested stakeholders related to: (a) the constants in the  $F_{en}$  expressions that result in  $F_{en}$  values of approximately 2 even when the strain rate is very high or the temperature is very low, (b) the temperature dependence of  $F_{en}$  for carbon and low-alloy steels, and (c) the dependence of  $F_{en}$  on water chemistry for austenitic SSs. The  $F_{en}$  methodology was validated by comparing the results of five different experimental data sets obtained from fatigue tests that simulate actual plant conditions with estimates of fatigue usage adjusted for environmental effects using the updated  $F_{en}$  expressions. The potential effects of dynamic strain aging on cyclic deformation and environmental effects are also discussed.



## FOREWORD

---

This report summarizes, reviews, and quantifies the effects of the light-water reactor (LWR) environments on the fatigue lives of reactor materials, including carbon steels, low-alloy steels, nickel-chromium-iron (Ni-Cr-Fe) alloys, and austenitic stainless steels. The primary purpose of this report is to provide the background and technical bases to support Regulatory Guide 1.207, "Guidelines for Evaluating Fatigue Analyses Incorporating the Life Reduction of Metal Components Due to the Effects of the Light-Water Reactor Environment for New Reactors."

The initial revision of this report included a review of the fatigue  $\epsilon$ -N data available at that time for carbon steels, low-alloy steels, Ni-Cr-Fe alloys, and austenitic stainless steels to define the potential effects of key material, loading, and environmental parameters on the fatigue lives of the steels. By drawing upon a larger database than was used in earlier published reports, the U.S. Nuclear Regulatory Commission (NRC) updated the Argonne National Laboratory (ANL) fatigue life models used to estimate the fatigue curves as a function of those parameters, and presented a procedure for incorporating environmental effects into fatigue evaluations. In this revision, additional fatigue  $\epsilon$ -N data available since the original publication of this report, most particularly from Japan, was incorporated into the database and the fatigue life models were updated. In addition, feedback from interested stakeholders obtained since the original publication of this report were evaluated and incorporated, where appropriate.

The database described in this report reinforces the position espoused by the NRC that the previously published guideline for incorporating the LWR environmental effects in fatigue life evaluations should be revised. Toward that end, this report maintains the previously established methods for establishing reference air fatigue curves, and defines updated environmental correction factors for use in evaluating the fatigue lives of reactor components exposed to LWR coolants and operational experience.

The data described in this updated review were used to verify the previously developed fatigue design curves in air that are consistent with the available fatigue data. The published data indicate that the existing ASME Code Section III curves are appropriate for austenitic stainless steels (e.g., Types 304, 316, and 316NG), and are conservative for carbon and low-alloy steels. Regulatory Guide 1.207 endorses the fatigue design curves presented herein for incorporation in fatigue analyses for new and operating reactors.

Brian W. Sheron, Director  
Office of Nuclear Regulatory Research  
U.S. Nuclear Regulatory Commission



# CONTENTS

---

Abstract .....	iii
Foreword .....	v
Contents .....	vii
Figures .....	xiii
Tables .....	xxi
Executive Summary .....	xxiii
Abbreviations .....	xxvii
Acknowledgments .....	xxxix
1. Introduction .....	1
1.1 Definition of Fatigue Life .....	1
1.2 Air Fatigue Design Curves in Section III of the ASME Code .....	3
1.3 Subfactors Included in ASME Section III Air Fatigue Design Curves .....	5
1.3.1 Effects of Reactor Coolant Environment on Fatigue Lives .....	6
1.3.2 Effects of Neutron Irradiation .....	9
1.4 Modeling of Environmental Effects .....	13
2. Mechanism of Fatigue .....	17
2.1 Formation of an Engineering Crack in Air .....	17
2.2 Fatigue Cracking in LWR Environments .....	21
2.2.1 Carbon and Low-Alloy Steels .....	21
2.2.1.1 Effects of Surface Micropits .....	21
2.2.1.2 Mechanisms of Corrosion Fatigue .....	22
2.2.1.3 Effects of Dynamic Strain Aging (DSA) .....	26
2.2.1.4 Crack Growth Rates in Smooth Fatigue Specimens .....	28
2.2.2 Austenitic Stainless Steels .....	29
2.2.2.1 Effects of Surface Micropits .....	31
2.2.2.2 Mechanisms of Corrosion Fatigue .....	31
2.2.2.3 Effects of Dynamic Strain Aging (DSA) .....	34
2.2.2.4 Crack Growth Rates in Smooth Fatigue Specimens .....	34

3.	Fatigue Strain vs. Life ( $\epsilon$ -N) Behavior in Air .....	39
3.1	Carbon and Low-Alloy Steels and Weld Metals .....	39
3.1.1	Experimental Data .....	39
3.1.2	Temperature .....	42
3.1.3	Strain Rate.....	42
3.1.4	Sulfide Morphology .....	43
3.1.5	Cyclic Strain Hardening Behavior .....	43
3.1.6	Fatigue Life Model .....	44
3.1.7	Heat-to-Heat Variability.....	47
3.1.8	Fatigue $\epsilon$ -N Behavior of Weld Metals .....	50
3.1.9	Surface Finish.....	50
3.1.10	Extension of the Best-Fit Mean Curve from $10^6$ to $10^{11}$ Cycles .....	51
3.1.11	Fatigue Design Curves .....	53
3.2	Wrought and Cast Austenitic Stainless Steels and Weld Metals .....	56
3.2.1	Experimental Data .....	56
3.2.2	Specimen Geometry and Type of Loading .....	60
3.2.3	Strain Rate.....	61
3.2.4	Temperature .....	61
3.2.5	Cyclic Strain Hardening Behavior .....	62
3.2.6	Fatigue Life Model .....	63
3.2.7	Heat-to-Heat Variability.....	65
3.2.8	Fatigue $\epsilon$ -N Behavior of Cast Austenitic Stainless Steels.....	66
3.2.9	Fatigue $\epsilon$ -N Behavior of Weld Metals .....	67
3.2.10	Surface Finish.....	68
3.2.11	Fatigue Design Curve .....	69
3.3	Ni-Cr-Fe Alloys and Weld Metals .....	71
3.3.1	Experimental Data .....	72

	3.3.2	Fatigue Life Model .....	74
4.		Fatigue $\epsilon$ -N Behavior in LWR Environments.....	77
	4.1	Carbon and Low-Alloy Steels.....	77
		4.1.1 Experimental Data .....	79
		4.1.2 Strain Rate.....	82
		4.1.3 Strain Amplitude .....	84
		4.1.4 Temperature .....	88
		4.1.5 Dissolved Oxygen.....	91
		4.1.6 Water Conductivity.....	92
		4.1.7 Sulfur Content in Steel .....	92
		4.1.8 Hold Periods .....	93
		4.1.9 Flow Rate .....	96
		4.1.10 Fatigue Life Model .....	97
		4.1.11 Environmental Fatigue Correction Factor.....	98
		4.1.12 Surface Finish.....	104
		4.1.13 Heat-to-Heat Variability.....	106
		4.1.14 Modified Rate Approach .....	107
	4.2	Wrought and Cast Austenitic Stainless Steels .....	110
		4.2.1 Experimental Data .....	111
		4.2.2 Strain Rate.....	115
		4.2.3 Strain Amplitude .....	116
		4.2.4 Temperature .....	118
		4.2.5 Dissolved Oxygen.....	119
		4.2.6 Water Conductivity.....	120
		4.2.7 Material Heat Treatment .....	121
		4.2.8 Cast Austenitic Stainless Steels.....	121
		4.2.9 Stainless Steel Weld Metals.....	124

4.2.10	Hold Periods .....	125
4.2.11	Flow Rate .....	126
4.2.12	Fatigue Life Model .....	127
4.2.13	Environmental Correction Factor .....	128
4.2.14	Surface Finish.....	135
4.2.15	Heat-to-Heat Variability.....	136
4.3	Ni-Cr-Fe Alloys .....	138
4.3.1	Experimental Data .....	138
4.3.2	Effects of Key Parameters .....	140
4.3.3	Environmental Correction Factor .....	141
5	Adjustment Factors in ASME Code Fatigue Design Curves.....	147
5.1	Material Variability and Data Scatter .....	149
5.2	Size and Geometry .....	150
5.3	Surface Finish.....	151
5.4	Loading Sequence.....	151
5.5	Air Fatigue Design Curve Adjustment Factors Summarized.....	152
6.	Validation of $F_{en}$ Expressions.....	157
6.1	Spectrum Straining .....	158
6.2	Complex Loading – Safety Injection Transient.....	162
6.3	U-Bend Tests in Inert and PWR Water Environments.....	166
6.4	Simulation of Actual Plant Conditions .....	170
7.	Summary .....	173
8.	References .....	177
APPENDIX A: Incorporating Environmental Effects into Fatigue Evaluations .....		A-1
A1	Scope .....	A-1
A2	Environmental Correction Factor ( $F_{en}$ ).....	A-1
A3	Fatigue Evaluation Procedure.....	A-3
APPENDIX B: MATERIAL INFORMATION .....		B-1

B1	Carbon and Low-Alloy Steels Included in the Fatigue Database .....	B-1
B2	Wrought and Cast Austenitic Stainless Steels and Welds.....	B-4
B3	Ni-Cr-Fe Alloys and Welds.....	B-7
APPENDIX C: SAMPLE PROBLEM.....		C-1
C1	Background .....	C-1
C2	Problem Description .....	C-1
C3	Evaluation.....	C-8
C4	Results .....	C-11
C5	References .....	C-73



## FIGURES

---

Figure 1.	Fatigue $\epsilon$ -N data for low-alloy steels and austenitic stainless steels in water compared to ASME Air Design Curve; RT = room temperature. ....	6
Figure 2.	The effects of neutron irradiation on fatigue lives of Type 347 SSs at room temperature: (a) the fatigue $\epsilon$ -N behavior, and (b) variations in plastic strain amplitude as a function of fatigue cycles (Ref. 109). ....	10
Figure 3.	Strain amplitude vs. fatigue life data in 325°C air or simulated PWR primary water environments for CW Type 316 SS irradiated to (a) less than $10^{22}$ , (b) $2-6 \times 10^{25}$ , and (c) greater than $3 \times 10^{26}$ n/m <sup>2</sup> ( $E > 1.0$ MeV) (Ref. 110). ....	12
Figure 4.	Strain amplitude vs. fatigue life data in 325°C air and simulated PWR primary water environments for Type 304 SS irradiated to $5 \times 10^{25} - 10^{26}$ n/m <sup>2</sup> ( $E > 0.1$ MeV) (Ref. 110). ....	12
Figure 5.	Two stages of fatigue crack growth in smooth test specimens. ....	17
Figure 6.	Schematic illustration of the plastic blunting process of fatigue crack growth in Stage II: (a) zero load; (b) small tensile load; (c) maximum tensile load, widening of slip bands; (d) crack closure, and formation of "ears" at crack tip; (e) maximum compressive load; (f) small tensile load in the subsequent cycle. ....	18
Figure 7.	Crack depth plotted as a function of fractional life for carbon and low-alloy steels tested in air (Refs. 11, 165-167). ....	19
Figure 8.	Schematic illustration of (a) growth of short cracks in smooth specimens as a function of fatigue life fraction, and (b) crack velocity as a function of crack depth. ....	20
Figure 9.	Fatigue life of carbon and low-alloy steel specimens in high-DO water at 288°C compared with the fatigue life of specimens preoxidized in high-DO water and tested in either air or low-DO water at 288°C (Refs. 40, 41, 176). ....	22
Figure 10.	Schematic illustration of slip oxidation/dissolution process. ....	23
Figure 11.	Schematic illustration of hydrogen-induced cracking of low-alloy steel. ....	25
Figure 12.	Fatigue cracks on gauge surfaces of A106-Gr. B carbon steel tested in (a) air and (b) high-DO water at 288°C (Ref. 10). ....	26
Figure 13.	Fatigue cracks along longitudinal sections of A106-Gr. B carbon steel tested in (a) air and (b) high-DO water at 288°C (Ref. 10). ....	26
Figure 14.	(a) Fatigue crack initiation and (b) crack growth in DSA susceptible low-alloy steel exposed to high-temperature water environment (Ref. 147). ....	27
Figure 15.	Depth of largest crack plotted as a function of (a) fatigue cycles and (b) fraction of fatigue life for A533-Gr B low-alloy steel in air and water environments (Ref. 11). ....	28
Figure 16.	(a) Morphology and length of surface crack after various numbers of cycles for A533-Gr. B steel in air at room temperature, and (b) fracture surface and probable crack front for surface cracks shown in (a) (Ref. 11). ....	28
Figure 17.	Crack growth rates plotted as a function of crack depth for A533-Gr B low-alloy steel tested in air and water environments (Ref. 11). ....	29

Figure 18.	Photomicrographs of oxide films that formed on Type 316NG stainless steel in (a) simulated PWR water and (b) high-DO water (Ref. 13).....	30
Figure 19.	Schematic of the corrosion oxide film formed on austenitic stainless steels in LWR environments. ....	30
Figure 20.	Effects of environment on formation of fatigue cracks in Type 316NG SS in air and low-DO water at 288°C. Preoxidized specimens were exposed for 10 days at 288°C in water that contained either less than 5 ppb DO and approximately 23 cm <sup>3</sup> /kg dissolved H <sub>2</sub> or approximately 500 ppb DO and no dissolved H <sub>2</sub> (Ref. 13). ....	31
Figure 21.	Photomicrographs of the fatigue crack morphology of Type 304 SS in (a) air, (b) high-DO BWR water, and (c) low-DO PWR water at 289°C (Ref. 47).....	32
Figure 22.	Photomicrographs showing sites of fatigue crack initiation on fracture surfaces of Type 304 SS tested at 289°C in (a) air, (b) high-DO BWR water, and (c) low-DO PWR water (Ref. 47).....	33
Figure 23.	Photomicrographs showing fatigue striations on fracture surfaces of Type 304 SS tested at 289°C in (a) air, (b) high-DO BWR water, and (c) low-DO PWR water (Ref. 47).....	33
Figure 24.	Depth of largest crack plotted as a function of fatigue cycles for austenitic stainless steels in air and water (Refs. 13,207).....	35
Figure 25.	Crack growth rates plotted as a function of crack length for austenitic stainless steels in (a) water and (b) air environments (Refs. 13,44,207). ....	35
Figure 26.	Crack growth rate data for Type 304 SS in high temperature water determined from (a) fracture mechanics CT specimens and (b) smooth cylindrical fatigue specimens (Ref. 208).....	36
Figure 27.	Fatigue strain vs. life data for carbon and low-alloy steels in air at room temperature (JNUFAD database and Refs. 10,18,19,48).....	41
Figure 28.	The change in fatigue lives of carbon and low-alloy steels in air as a function of temperature. ....	42
Figure 29.	Effect of strain rate and temperature on cyclic stress of carbon and low-alloy steels. ....	44
Figure 30.	Schematic diagram of the best-fit of the experimental data by minimizing the distance between the data point and the S-N curve. ....	45
Figure 31.	Experimental and predicted fatigue lives of (a, b) carbon steels and (c, d) low-alloy steels in air.....	46
Figure 32.	Estimated cumulative distribution of constant A in the ANL models for fatigue life data in the original revision of NUREG/CR-6909 (a, c) and this report (b, d); (a, b) for heats of carbon steels and (c, d) low-alloy steels in air. ....	48
Figure 33.	Fatigue $\epsilon$ -N behavior for carbon and low-alloy steel weld metals in air at room temperature and 289°C (Ref. 136).....	50
Figure 34.	Effect of surface finish on the fatigue life of A106-Gr B carbon steel in air at 289°C (Ref. 46).....	51
Figure 35.	Fatigue design curves based on the ANL model for (a) carbon steels and (b) low-alloy steels in air. ....	54

Figure 36.	Fatigue design curve for carbon steels in air. The curve developed from the ANL model is based on factors of 12 on life and 2 on stress.....	55
Figure 37.	Fatigue design curve for low-alloy steels in air. The curve developed from the ANL model is based on factors of 12 on life and 2 on stress. ....	55
Figure 38.	Fatigue $\epsilon$ -N behavior for Types 304, 304L, 316, and 316NG SS austenitic stainless steels in air at various temperatures up to 400°C (Refs. 13,42-47, 61,136). ....	58
Figure 39.	Influence of specimen geometry on fatigue lives of Types 304 and 316 stainless steels (JNUFAD data). ....	60
Figure 40.	Influence of bending loading on fatigue lives of Types 304 and 316 stainless steels (JNUFAD data).....	60
Figure 41.	Influence of temperature on fatigue lives of austenitic stainless steels in air (Ref. 61-63). ....	61
Figure 42.	Effects of strain amplitude, temperature, and strain rate on cyclic strain-hardening behavior of Types 304 and 316NG SSs in air at 288°C and room temperature. ....	62
Figure 43.	Cyclic stress-strain curves for Types 316, 304 and 316NG SSs in air at room temperature and 288°C. ....	63
Figure 44.	Experimental and predicted fatigue lives (using the ANL model) for austenitic SSs in air. ....	64
Figure 45.	Estimated cumulative distribution of constant A in the ANL model for fatigue lives for heats of austenitic SSs in air included in (a) the initial revision of NUREG/CR-6909 and (b) those included in this report. ....	65
Figure 46.	Fatigue $\epsilon$ -N behavior for several heats of CF-8M cast austenitic SSs in air at various temperatures. ....	67
Figure 47.	Fatigue $\epsilon$ -N behavior for austenitic SS weld metals in air at room temperature. ....	68
Figure 48.	Effects of surface roughness on fatigue lives of (a) Type 316NG and (b) Type 304 SSs in air (Ref. 46). ....	68
Figure 49.	Fatigue design curves for austenitic SSs in air.....	70
Figure 50.	Fatigue $\epsilon$ -N behavior for Alloys 600, 690 and 800 in air at temperatures between room temperature and 315°C (Refs. JNUFAD data, 61,66-75). ....	73
Figure 51.	Fatigue $\epsilon$ -N behavior for Alloys 62, 82, 132, 152, and 182 welds in air at various temperatures (Refs. JNUFAD data,61,66-75). ....	73
Figure 52.	Fatigue $\epsilon$ -N behavior for Inconel 718 in air at room temperature and 427°C (Refs. 61,72,73,136,210). ....	73
Figure 53.	Fatigue $\epsilon$ -N behavior for carbon and low-alloy steels in air at room temperature and high-purity water at temperatures below 150°C (Ref. 137). ....	79
Figure 54.	Strain amplitude vs. fatigue life data for (a) A533-Gr B and (b) A106-Gr B steels in air and high-dissolved-oxygen water at 288°C (Ref. 10). ....	81
Figure 55.	Dependence of fatigue lives of carbon and low-alloy steels on strain rate (Refs. 10,23). ....	83

Figure 56.	Fatigue life of A533–Gr. B low-alloy steel as a function of strain rate in high purity water with 0.1 or 2.0 ppm dissolved oxygen (Refs. 141,143).....	84
Figure 57.	Fatigue strain-life behavior of A533–Gr. B and A508–Gr. 3 low-alloy steels at 288°C in air and high-purity water with 0.1 ppm dissolved oxygen (Ref. 151). ....	84
Figure 58.	Fatigue life of A106–Gr B carbon steel at 288°C and 0.75% strain range in air and water environments under different loading waveforms (Ref. 10).....	85
Figure 59.	Fatigue lives of carbon and low–alloy steels tested with loading waveforms where slow strain rate was applied during a fraction of the tensile loading cycle (Refs. 10,24).....	86
Figure 60.	Experimental values of fatigue life and those predicted from the modified rate approach (a) without and (b) with consideration of a threshold strain (Ref. 136). ....	87
Figure 61.	Change in fatigue life of A333–Gr. 6 carbon steel and A508–Gr. 3 low-alloy steel with temperature and DO (Ref. 136).....	89
Figure 62.	Waveforms for changes in temperatures and strains during exploratory fatigue tests (Ref. 21). ....	90
Figure 63.	Fatigue lives of A333–Gr. 6 carbon steel tube specimens under varying temperature conditions, as indicated by horizontal bars (Ref. 21). ....	90
Figure 64.	Dependence on DO of the fatigue lives of carbon and low alloy steels in high-purity water (Ref. 18, 19, 22).....	91
Figure 65.	Effect of strain rate on fatigue life of low–alloy steels with different sulfur contents (Refs. 10, 136).....	92
Figure 66.	Effect of strain rate on the fatigue lives of A333–Gr. 6 carbon steels with different sulfur contents (Ref. 10).....	93
Figure 67.	Fatigue lives of A106–Gr B steel in air and water environments at 288°C, 0.78% strain range, and hold periods at peak tensile strain (Ref. 10). Hysteresis loops are for tests in air. ....	94
Figure 68.	Effect of hold periods on the fatigue lives of A333–Gr. 6 carbon steel at 289°C in water with 1 ppm DO (Ref. 24). ....	95
Figure 69.	Effects of water flow rate on fatigue lives of A333–Gr. 6 and A508–Gr. 1 carbon steels and A533–Gr. B low-alloy steel at 289°C and 0.3 or 0.6% strain amplitudes and various strain rates (Ref. 25,26). ....	96
Figure 70.	Effect of flow rate on low–cycle fatigue of carbon steel tube bends in high–purity water at 240°C (Ref. 55). RT = room temperature.....	97
Figure 71.	Experimental fatigue lives of carbon steels in LWR environments vs. fatigue lives predicted from the (a) new expression, (b) JNES expression, and (c) the previous NUREG/CR-6909 expression. ....	99
Figure 72.	Experimental fatigue lives of low-alloy steels in LWR environments vs. fatigue lives predicted from the (a) new expression, (b) JNES expression, and (c) the previous NUREG/CR-6909 expression. ....	100
Figure 73.	Comparison of the fatigue lives of carbon and low-alloy steels predicted from the new $F_{en}$ expression and the JNES $F_{en}$ expression. ....	101

Figure 74.	Residuals for predicted fatigue lives of carbon steels as a function of (a) Material ID, (b) water dissolved oxygen content, (c) strain rate, (d) temperature, (e) steel sulfur content, and (f) strain amplitude. ....	102
Figure 75.	Residuals for predicted fatigue lives of low-alloy steels as a function of (a) Material ID, (b) water dissolved oxygen content, (c) strain rate, (d) temperature, (e) steel sulfur content, and (f) strain amplitude. ....	103
Figure 76.	Residuals for predicted fatigue lives in air of carbon and low-alloy steels as a function of Material ID. ....	104
Figure 77.	Effect of surface finish on the fatigue lives of (a) A106–Gr B carbon steel and (b) A533 low–alloy steel in air and high–purity water at 289°C (Ref. 46). ...	105
Figure 78.	Relationship between surface finish and fatigue life reduction fraction for A533–Gr. B low-alloy steel in water at 288°C (Ref. 144). ....	105
Figure 79.	Estimated cumulative distribution of parameter A in the ANL model for fatigue lives for heats of carbon and low–alloy steels in LWR environments. ....	107
Figure 80.	Application of the modified rate approach to determine the environmental fatigue correction factor $F_{en}$ during the increasing strain portion of a transient. ....	108
Figure 81.	Example showing $F_{en}$ values computed using average temperatures compared to the $F_{en}$ computed using an integrated (modified rate) approach. ...	109
Figure 82.	Strain amplitude vs. fatigue life data for (a) Type 304 and (b) Type 316NG SSs in water at 288°C (JNUFAD and Refs. 13,45). ....	113
Figure 83.	Fatigue stress - life data from load-controlled tests on Type 304L SSs, with and without mean stress, in air and PWR water (Ref. 60). ....	114
Figure 84.	Fatigue strain - life data from load-controlled tests on Type 304L SSs, with and without mean stress, in air (a, c) and PWR water (b, d) (Refs. 58,60). ....	115
Figure 85.	Dependence of fatigue lives of austenitic stainless steels on strain rate in low–DO water (Refs. 13,45,47,60). ....	116
Figure 86.	Dependence of fatigue lives of Types (a) 304 and (b) 316NG SSs on strain rate in high– and low–DO water at 288°C (Ref. 13,45,47). ....	116
Figure 87.	Results of strain rate change tests on Type 316 SSs in low–DO water at 325°C. Low strain rate was applied during only a fraction of the tensile loading cycle. Fatigue life is plotted as a function of fraction of strain at high strain rate (Refs. 30,35). ....	117
Figure 88.	Change in fatigue lives of austenitic stainless steels in low–DO water with temperature (Refs. 13,29–31,34,45–47). ....	118
Figure 89.	Fatigue lives of Type 316 SSs under constant and varying test temperatures (Ref. 29,30). ....	119
Figure 90.	Effects of water conductivity and soaking period on fatigue lives of Type 304 SSs in high–DO water (Ref. 13,45). ....	120
Figure 91.	The effects of material heat treatment on fatigue lives of Type 304 SSs in air, BWR and PWR environments at 289°C, approximately 0.38% strain amplitude, sawtooth waveform loading, and 0.004%/s tensile strain rate (Ref. 47). ....	121

Figure 92.	Fatigue lives of cast austenitic SSs in high-purity water at 289°C and 0.3% and 0.6% strain amplitude plotted as a function of DO content (Ref. 136). .....	122
Figure 93.	Strain amplitude vs. fatigue life data for cast austenitic SSs at 325°C and various strain rates in water with 0.005 ppm DO content (Ref. 29,34).....	122
Figure 94.	Dependence of fatigue lives of CF-8M cast SSs on strain rate in low-DO water at various strain amplitudes (Refs. 136,43,45). .....	123
Figure 95.	Change in fatigue lives of cast austenitic SSs in low-DO water with temperature (Ref. 136). .....	124
Figure 96.	Strain amplitude vs. fatigue lives for Types 308 and 316TP SS weld metals at 325°C and various strain rates in water with 0.005 ppm DO content (Ref. 136). .....	124
Figure 97.	Change in fatigue lives of SS weld metals in LWR environments with strain rate and temperature (Ref. 136).....	125
Figure 98.	Fatigue lives of Type 304 SSs tested in high-DO water at 260–288°C with trapezoidal or triangular waveform loadings (Refs. 14,31). .....	125
Figure 99.	Effect of hold periods on the fatigue lives of Types 316NG and 316 SSs in LWR environments at various strain rates (Ref. 136).....	126
Figure 100.	Effects of water flow rate on the fatigue lives of Types 304, 304L, 316NG and CF-8M cast SSs in high-purity water at 289°C (Ref. 136). .....	127
Figure 101.	Effects of water flow rates on the fatigue lives of Type 304 and 316 austenitic SSs in PWR primary water at 325°C (Ref. 136). .....	127
Figure 102.	Experimental fatigue lives of wrought and cast austenitic SSs in LWR environments vs. fatigue lives predicted from (a) the updated ANL expression, (b) the JNES expression, (c) the previous NUREG/CR-6909 expression, and (d) fatigue lives of SS weld metals predicted from the updated ANL expression.....	130
Figure 103.	Fatigue lives of wrought and cast austenitic SSs in LWR environments estimated from the new $F_{en}$ expressions vs. those estimated from the JNES expression. ....	131
Figure 104.	Experimental fatigue lives of Types 304L and 316N austenitic SSs in LWR environments vs. fatigue lives predicted from (a) the updated ANL expression and (b) the JNES expression. ....	132
Figure 105.	Experimental fatigue lives of wrought and cast austenitic SSs in water containing greater than 0.1 ppm DO vs. fatigue lives predicted from (a) the updated ANL expression and (b) the JNES expression.....	132
Figure 106.	Residuals for predicted fatigue lives of wrought and cast austenitic SSs as a function of (a) ANL Material ID, (b) water DO content, (c) strain rate, (d) temperature, and (e) strain amplitude.....	134
Figure 107.	Residuals for predicted fatigue lives of wrought and cast austenitic SSs in air as a function of ANL Material ID. ....	135
Figure 108.	Effect of surface finish on fatigue life of (a) Type 316NG and (b) Type 304 stainless steels in air and high-purity water at 289°C. ....	136

Figure 109.	Effects of surface finish on the fatigue lives of Type 304L SSs in air and PWR primary water environments at 300°C (Refs. 155,157). .....	136
Figure 110.	Estimated cumulative distribution of constant A in the ANL model for fatigue lives of heats of austenitic SSs in LWR environments.....	137
Figure 111.	Fatigue $\epsilon$ -N behavior for Alloy 600 and its weld alloys in simulated BWR water at approximately 289°C (Refs. 136, 39).....	139
Figure 112.	Fatigue $\epsilon$ -N behavior for Alloys 600 and 690 and associated weld metals in simulated PWR water at 325°C (Refs. 136, 75). .....	139
Figure 113.	Dependence of fatigue lives of Alloys 690 and 600 and associated weld metals on strain rate in PWR and BWR environments (Refs. 39, 75, 136).....	140
Figure 114.	Dependence of fatigue lives of Alloy 600 on temperature in a PWR environment (Refs. 39, 75, 136).....	141
Figure 115.	Experimental fatigue lives vs. fatigue lives predicted from the updated $F_{En}$ expression for Ni-Cr-Fe alloys and weld metals in simulated (a) BWR and (b) PWR environments. ....	142
Figure 116.	Experimental fatigue lives vs. fatigue lives predicted from the $F_{En}$ expression in the original revision of NUREG/CR-6909 for Ni-Cr-Fe alloys and weld metals in simulated (a) BWR and (b) PWR environments.....	143
Figure 117.	Experimental fatigue lives vs. fatigue lives predicted from the JNES $F_{En}$ expression for Ni-Cr-Fe alloys and associated weld metals in simulated (a) BWR and (b) PWR environments. ....	143
Figure 118.	Residuals for predicted fatigue lives of Ni-Cr-Fe alloys and associated weld metals as a function of (a) material ID, (b) water DO content, (c) strain rate, (d) temperature, and (e) strain amplitude.....	145
Figure 119.	Residuals for predicted fatigue lives of Ni-Cr-Fe alloys and associated weld metals in air as a function of ANL Material ID. ....	146
Figure 120.	Fatigue data for (a) carbon and low-alloy steel and (b) Type 304 stainless steel components (Refs. 237,238). .....	148
Figure 121.	Estimated cumulative distribution of parameter A in the ANL models that represent the fatigue lives of test specimens and actual components in air. ....	155
Figure 122.	Schematic of the repeated sequence of randomized block of 50 strain cycles (Ref. 158). .....	159
Figure 123.	Fatigue strain-life data for Type 316NG SS in PWR water at 320°C and for Ti-stabilized 316 SS in VVER water at 293°C (Refs. 158,159).....	161
Figure 124.	Experimental and estimated fatigue lives for Type 316NG and Ti-stabilized 316 SS tested with constant and spectrum strain loading (Refs. 158,159).....	162
Figure 125.	Typical strain cycle of cold and hot thermal shocks corresponding to a PWR safety injection transient (Ref. 155).....	163
Figure 126.	Fatigue strain-life data for Type 304L SS in air and PWR environments at 300°C (Refs. 155-157).....	164

Figure 127.	The experimental and estimated fatigue lives for Type 304L SS tested at 300°C in air and a PWR environment using triangular and complex loading that simulated a PWR safety injection transient (Refs. 155-157).....	165
Figure 128.	U-bend test specimen and nomenclature (Ref. 97). .....	166
Figure 129.	Overview of the extent and location of fatigue cracking in U-bend tests at strain amplitude of 0.6% (Ref. 97).....	168
Figure 130.	Overview of the extent and location of fatigue cracking in U-bend tests at strain amplitude of 0.4% (Ref. 97).....	169
Figure 131.	The experimental and predicted fatigue lives for Type 304L SS U-bend specimens at 240°C in inert and PWR environments (Refs. 97-99). .....	170
Figure 132.	Loading waveforms for Fatigue Test Nos. 1 and 7 (Ref. 154). .....	171
Figure 133.	The experimental and predicted fatigue lives of Type 316 SS tested in PWR primary water using two blocks of fatigue cycles of different strain amplitudes and varying temperature and strain rate (Ref. 154).....	172
Figure A.1.	Fatigue design curves for carbon steels in air. The curve developed from the ANL model is based on factors of 12 on life and 2 on stress. ....	A-4
Figure A.2.	Fatigue design curves for low-alloy steels in air. The curve developed from the ANL model is based on factors of 12 on life and 2 on stress. ....	A-4
Figure A.3	Fatigue design curve for austenitic stainless steels in air. The curve developed from the ANL model is based on factors of 12 on life and 2 on stress.....	A-5
Figure C.1.	Sample Problem Geometry.....	C-2
Figure C.2.	Sample Problem Transient Time Histories .....	C-4
Figure C.3.	Sample Problem Transient Membrane Plus Bending Stress Histories for SCL 2 .....	C-5
Figure C.4.	Sample Problem Transient Total Stress Histories for SCL 2 .....	C-6
Figure C.5.	Sample Problem Combined Transient Stress History for SCL 2.....	C-7
Figure C.6.	Principal Stress Intensity Histories and Peaks and Valleys Used in Limiting CUF Calculation for Sample Problem for SCL 2 .....	C-13

## TABLES

---

Table 1.	Sources of the fatigue $\epsilon$ -N data on carbon and low-alloy steels in air environment.....	40
Table 2.	Values of constant A in the ANL fatigue life model for carbon steels in air and the factors on life as a function of confidence level and percentage of population bounded. ....	49
Table 3.	Values of constant A in the ANL fatigue life model for low-alloy steels in air and the factors on life as a function of confidence level and percentage of population bounded. ....	50
Table 4.	Fatigue design curves for carbon and low-alloy steels including proposed updated extension to $10^{11}$ cycles.....	54
Table 5.	Fatigue design curves for carbon and low-alloy steels and the extension to $10^{11}$ cycles proposed in the initial revision to NUREG/CR-6909. ....	55
Table 6.	Sources of the fatigue $\epsilon$ -N data on wrought and cast austenitic stainless steels in an air environment. ....	56
Table 7.	Values of constant A in the ANL fatigue life model for austenitic SSs and the factors on fatigue lives for austenitic SSs in air as a function of confidence level and percentage of population bounded.....	66
Table 8.	The ASME Code fatigue design curves for austenitic SSs in air. ....	69
Table 9.	Sources of the fatigue $\epsilon$ -N data on Ni-Cr-Fe alloys and their weld metals in an air environment. ....	71
Table 10.	Sources of the fatigue $\epsilon$ -N data for carbon and low-alloy steels in LWR environments. ....	80
Table 11.	Sources of the fatigue $\epsilon$ -N data for cast and austenitic stainless steels in LWR environments. ....	112
Table 12.	Sources of the fatigue $\epsilon$ -N data for Ni-Cr-Fe alloys and their weld metals in LWR environments. ....	138
Table 13.	Statistical information for the constant A used to evaluate material variability and data scatter. ....	150
Table 14.	Factors on life applied to the mean fatigue $\epsilon$ -N air curve to account for the effects of various material, loading, and environmental parameters. ....	153
Table 15.	Factor applied to the mean values of fatigue life to bound 95% of the data population. ....	154
Table 16.	Chemical composition and tensile strength of test materials for the constant and spectrum strain amplitude fatigue tests. ....	158
Table 17.	Environmental conditions for the constant and spectrum strain amplitude fatigue tests. ....	159
Table 18.	The conditions and results of fatigue tests on austenitic SSs obtained under constant and spectrum strain amplitude loading. ....	160
Table 19.	Chemical composition and tensile strength of Type 304L SS. ....	163

Table 20.	Environmental conditions for fatigue tests in simulated PWR environment. ....	163
Table 21.	The conditions and results of fatigue tests on Type 304L austenitic SS at 300°C in air and PWR environments using a triangular or complex strain cycle. ....	165
Table 22.	Summary of the key conditions and results of the U-bend tests at 240°C. ....	168
Table 23.	Chemical composition and tensile strength of Type 316 SS material. ....	170
Table 24.	Test matrix for the two blocks fatigue damage tests.....	172
Table 25.	Results of the two blocks fatigue damage tests.....	172
Table A.1.	Fatigue design curves for carbon and low-alloy steels in air.....	A-5
Table A.2.	Fatigue design curves for austenitic stainless steels in air. ....	A-5
Table C.1.	Sample Problem Transient Definitions .....	C-3
Table C.2.	Limiting CUF Results for Sample Problem for SCL 2 .....	C-12
Table C.3.	CUF <sub>en</sub> Results Based for Sample Problem for SCL 2 (Average Strain Rate Approach).....	C-14
Table C.4.	CUF <sub>en</sub> Results Based for Sample Problem for SCL 2 (Modified Strain Rate Approach).....	C-15
Table C.5.	Principal Stress Intensity Histories Used in Limiting CUF Calculation for Sample Problem for SCL 2 .....	C-16

## EXECUTIVE SUMMARY

---

Cyclic loadings on a reactor pressure boundary component occur because of changes in mechanical and thermal loadings as the system goes from one load set (e.g., pressure, temperature, moment, and force loading) to another. The American Society of Mechanical Engineers (ASME) Boiler and Pressure Vessel Code Section III, Subsection NB contains rules for the design of Class 1 components of nuclear power plants and recognizes fatigue as a possible mode of failure in pressure vessel steels and piping materials. ASME Code Section III fatigue analysis procedures consider all fatigue cycles based on the anticipated number of thermal and pressure transients, and for each load-cycle or load set pair, an individual fatigue usage factor is determined by the ratio of the number of cycles anticipated during the design lifetime of the component, as specified by the Owner, to the number of allowable cycles. Figures I-9.1 through I-9.6 of Mandatory Appendix I to Section III of the ASME Code specify fatigue design curves that define the allowable number of cycles as a function of applied stress amplitude. Those fatigue design curves have evolved significantly since the initial publication of Section III in 1963. However, Paragraph NB-3121 of the 2011 Addenda to Section III of the Code continues to state that the effects of coolant environments on the fatigue resistance of materials were not addressed in the fatigue design curves. Therefore, the effects of water environments on the fatigue resistance of materials used in operating pressurized water reactor (PWR) and boiling water reactor (BWR) plants, whose components were designed in accordance with the ASME Code Section III, may not adequately address long-term environmental effects on fatigue based on the data available at the time the fatigue design curves were derived.

The current Section III design fatigue curves in air contained in Section III of the ASME Code were based primarily on strain-controlled fatigue tests of small polished specimens at room temperature in laboratory air environments. Best-fit curves to the experimental test data were first adjusted to account for the effects of mean stress and then lowered by a factor of 2 on stress and 20 on cycles (whichever was more conservative) to obtain the design fatigue air curves. These factors were not intended as “safety margins,” but rather they were intended as “adjustment factors” that were applied to the experimental laboratory data to obtain estimates of the fatigue lives of actual reactor components. Recent fatigue-strain-vs.-life ( $\epsilon$ -N) data obtained primarily in the U.S. and Japan demonstrate that light water reactor (LWR) environments have potentially significant effects on the fatigue resistance of materials. Specimen lives obtained from laboratory tests in simulated LWR environments were much shorter than those obtained from corresponding tests in an air environment.

In the original version of NUREG/CR-6909, the existing fatigue  $\epsilon$ -N data for carbon and low-alloy steels, wrought and cast austenitic stainless steels (SSs), and nickel-chromium-iron (Ni-Cr-Fe) alloys in air and LWR environments were evaluated to identify the various material, environmental, and loading parameters that influence fatigue crack initiation. The results of those evaluations were used to establish the effects of key parameters on the fatigue lives of steels. The fatigue lives of materials were decreased in LWR environments; the magnitude of the reduction depended on the temperature, strain rate, dissolved oxygen (DO) level in the water, and, for carbon and low-alloy steels, the sulfur (S) content of the steels. For all steels, environmental effects on fatigue lives were significant only when critical parameters (temperature, strain rate, DO level, and strain amplitude) met certain threshold values. Environmental effects were moderate, e.g., less than a factor of 2 decrease in fatigue lives, when any one of the threshold conditions was not satisfied. The threshold values of the critical parameters and the effects of other parameters (such as water conductivity, water flow rate, and material heat treatment) on the fatigue lives of the steels were also discussed.

In this report, the comprehensive review of the fatigue  $\epsilon$ -N data for nuclear power plant piping and pressure vessel steels presented in the original version of NUREG/CR-6909 was reevaluated using a much larger database. The results were updated to include this reevaluation, as well as to address concerns from interested stakeholders regarding the  $F_{en}$  methodology for incorporating environmental effects into ASME Code Section III fatigue cumulative usage factor (CUF) evaluations. The resulting effects of various material, loading, and environmental parameters on the fatigue lives of steels are summarized in this report.

The results indicated that the ASME Code Section III mean air curve for low-alloy steels is in good agreement with the available experimental data, and the ASME Code Section III mean air curve for carbon steels is conservative. In addition, the best-fit mean air data used to develop the fatigue design air curve for austenitic SSs in ASME Code Section III editions prior to 2009b Addenda is not consistent with the experimental data at strain amplitudes less than 0.5%; fatigue lives predicted by the ASME Code Section III mean air curve were longer than those obtained from experiments. Therefore, in the initial version of NUREG/CR-6909, new fatigue design air curves were developed for carbon and low-alloy steels and austenitic SSs that were based on the ANL fatigue life models and were consistent with the fatigue  $\epsilon$ -N data available at that time. The air design curves were extended up to  $10^{11}$  cycles using available high-cycle fatigue data. In 2009, the ANL design air curve for austenitic SSs was adopted into Mandatory Appendix I of Section III of the ASME Code. The reevaluation of the fatigue  $\epsilon$ -N behavior of austenitic SS materials using a much larger database indicated that the air fatigue design curves previously developed by ANL are consistent with the available fatigue data, and do not warrant any modifications. However, in the present report, the extension of the air fatigue design curves for carbon and low-alloy steels up to  $10^{11}$  cycles was modified to be consistent with the extension of the current ASME Code Section III fatigue design curve beyond  $10^6$  cycles.

The reevaluation results also indicated that the fatigue data for Ni-Cr-Fe alloys were not consistent with the current ASME Code mean air curve for austenitic SSs. The rather limited fatigue  $\epsilon$ -N data for Ni-Cr-Fe alloys, such as Alloys 600, 690, and 800 and their welds, were consistent with the best-fit mean air curve for austenitic SSs at fatigue lives less than  $10^4$  cycles, and showed longer fatigue lives than the predicted values for fatigue lives greater than  $10^4$  cycles. However, a separate air fatigue design curve was not developed for Ni-Cr-Fe alloys, and the current ASME Code fatigue air design curve for austenitic SSs, which is based on the ANL model, was used to represent the fatigue  $\epsilon$ -N behavior of Ni-Cr-Fe alloys and associated weld metals. The data also indicated that the fatigue resistance of Inconel 718 is superior to that of the other Ni-Cr-Fe alloys. The slope of the Inconel 718 fatigue  $\epsilon$ -N curve is flatter and the fatigue limit is higher than those for austenitic SSs.

The fatigue lives of carbon and low-alloy steels, austenitic SSs, and Ni-Cr-Fe alloys were decreased in LWR environments. The reduction depended on some key material, loading, and environmental parameters. The fatigue  $\epsilon$ -N data were consistent with the much larger database on enhancement of crack growth rates in these materials in LWR environments. The key parameters that influenced fatigue lives in these environments, e.g., temperature, DO level in the water, strain rate, strain (or stress) amplitude, and, for carbon and low-alloy steels, S content of the steel, were identified. In addition, the functional form of the dependence of fatigue lives on these parameters and the range of the values of these parameters within which environmental effects were significant was defined. If these critical loading and environmental conditions exist during reactor operation, then environmental effects may be significant and should be included in any relevant ASME Code Section III fatigue evaluations.

In the initial version of NUREG/CR-6909 (published in 2007), fatigue life models were developed to predict the fatigue lives of small smooth specimens of carbon and low-alloy steels, wrought and cast austenitic SSs, and Ni-Cr-Fe alloys as a function of material, loading, and environmental parameters using the existing fatigue  $\epsilon$ - $N$  database. The functional form and bounding values of these parameters were based on experimental observations and data trends. An approach was presented that incorporated the effects of LWR coolant environments into the ASME Code Section III fatigue evaluations based on the environmental fatigue correction factor,  $F_{en}$ . The fatigue usage for a specific stress cycle or load set pair derived using the ASME Code Section III fatigue design air curves was multiplied by the  $F_{en}$  to account for environmental effects.

In the present report, the  $F_{en}$  expressions were updated using a much larger fatigue  $\epsilon$ - $N$  database, primarily derived from extensive additional data provided from Japan. The updated expressions also address comments provided by interested stakeholders related to: (a) the constants in the  $F_{en}$  expressions that results in a  $F_{en}$  value of approximately 2 even when the strain rate is very high or temperature is very low, (b) the temperature dependence of  $F_{en}$  for carbon and low-alloy steels, and (c) the dependence of  $F_{en}$  on water chemistry for austenitic SSs.

This report also presents a brief description of the mechanisms for fatigue cracking in air and LWR coolant environments. Fatigue life is conventionally divided into two stages: initiation and propagation. In LWR environments, the initiation stage involves the growth of microstructurally small cracks characterized by decelerating crack growth. The propagation stage involves the growth of mechanically small cracks characterized by accelerating crack growth. The available fatigue  $\epsilon$ - $N$  data indicated that LWR environments affect both the initiation and propagation of fatigue cracks. Two mechanisms are described in this report that potentially enhance both fatigue crack initiation and fatigue crack growth rates in LWR environments - slip oxidation/dissolution and hydrogen-induced cracking. The potential effects of dynamic strain aging on cyclic deformation and environmental effects are also discussed.

This report also presents a critical review of the ASME Code Section III fatigue adjustment factors of 2 on stress and 20 on life and assesses the possible conservatism in the choice of adjustment factors. Although these factors were intended to be conservative, they were not considered safety margins in the work presented in this report. Instead, these factors cover the effects of variables that influence fatigue lives but were not investigated in the experiments that were used to obtain the air fatigue design curves. Data available in the literature were reviewed to evaluate the factors on cycles that are needed to account for such differences and uncertainties. Monte Carlo simulations were performed to determine the factor on cycles needed to obtain a fatigue design curve in air that provided a conservative estimate of the number of cycles required to initiate a fatigue crack in reactor components. The results presented in the initial version of NUREG/CR-6909 indicated that, for carbon and low-alloy steels and austenitic SSs, the current ASME Code Section III requirements for a factor of 20 on cycles to account for the effects of material variability and data scatter, as well as size, surface finish, and loading history, may be decreased by at least a factor of 1.7. Thus, to reduce conservatism, fatigue design curves were developed based on the ANL fatigue life models and those curve were then adjusted for mean stress effects and by a factor of 2 on stress and 12 on cycles. These adjustments were made to account for the effects of four parameters - material variability and data scatter, size, surface finish, and loading sequence. In this report, the range of the these four parameters were modified and Monte Carlo simulations were repeated to determine the factor on cycles needed to obtain fatigue design curves in air. The results indicated that for carbon and low-alloy steels and austenitic SSs, a factor of 2 on stress and 10 on cycles are adequate to develop air fatigue design curves from the best-fit mean air curves.

However, until these results are further validated with applicable fatigue data  $\epsilon$ -N data, the air fatigue design curves presented in this report are based on factors of 2 on stress and 12 on life.

The  $F_{en}$  methodology was also validated by comparing the results of several experimental data sets obtained from fatigue tests that simulated actual plant conditions with estimated fatigue usage using the updated  $F_{en}$  expressions. The data sets represented fatigue tests with changing strain rate and/or temperature, complex loading that simulated a PWR safety injection transient, spectrum loading (i.e., random strain amplitudes), and pipe U-bend tests. In all cases, the results indicated that the predicted fatigue lives were in good agreement with the experimental values; the differences between the experimental and predicted fatigue lives were within a factor of two, which is within the experimental data scatter. The predicted fatigue lives for the tests with the complex strain loading cycle were lower than the experimental values by a factor of about 2. The reason for this deviation was not clear but may be unique to the specific test loading cycle. Nonetheless, although the predicted lives were all lower, the estimated values were within the range of data scatter.

Finally, the detailed procedure for incorporating environmental effects into ASME Code Section III fatigue evaluations is presented.

Revision 1 of this report represents a comprehensive and detailed expansion of the Revision 0 manuscript that incorporates significant additional background, test data, and test data descriptions. In addition, the content layout of the report was revised for clarity. As a result, the revisions made to the Revision 0 manuscript are not specifically identified throughout the text of this revision.

## ABBREVIATIONS

---

ANL	Argonne National Laboratory
ANN	Artificial Neural Network
ASME	American Society of Mechanical Engineers
ASTM	American Society for Testing and Materials
ATR	Advanced Test Reactor
BTP	Branch Technical Position
BNCS	Board on Nuclear Codes and Standards
BWR	Boiling Water Reactor
CGR	Crack Growth Rate
CLEE	Cyclic Life Environmental Effects
CT	Compact Tension
CUF	Cumulative Usage Factor
CVCS	Chemical and Volume Control System
CW	Cold Worked
da/dN	Fatigue Crack Growth Rate (expressed as the change in crack depth, da, divided by the number of applied cycles, dN)
DO	Dissolved Oxygen
DSA	Dynamic Strain Aging
E	Energy
EAC	Environmentally Assisted Cracking
EBR II	Experimental Breeder Reactor II
ECP	electrochemical Potential
EFD	Environmental Fatigue Data
EFT	Environmental Fatigue Testing
EPR	Electrochemical Potentiodynamic Reactivation
EPRI	Electric Power Research Institute
ETR	Experimental Test Reactor
FAP	Fatigue Action Plan
GE	General Electric Company
GSI	Generic Safety Issue
H	Hydrogen
HAZ	Heat Affected Zone
He	Helium
HWC	Hydrogen Water Chemistry
ID	Internal Diameter
IG	Intergranular

## ABBREVIATIONS (continued)

---

IHI	Ishikawajima-Harima Heavy Industries
INEL	Idaho National Engineering Laboratory
JAPEIC	Japan Power Engineering and Inspection Corporation
JNES	Japan Nuclear Energy Safety Organization
JNUFAD	Revised and Renamed Fatigue Database "FADAL" from Japan
KWU	Kraftwerk Union Laboratories
LEFM	Linear Elastic Fracture Mechanics
LWR	Light Water Reactor
MA	Mill Annealed
MEA	Materials Engineering Associates
MHI	Mitsubishi Heavy Industries
mm	Millimeters
MnS	Manganese Sulfide
MOU	Memorandum of Understanding
MPa	Megapascals
MPA	Materialprüfungsanstalt
MSC	Microstructurally Small Crack
N	Number of Cycles
$N_{\text{air}}$	Number of Cycles in Air
$N_{\text{water}}$	Number of Cycles in LWR Environment
Ni-Cr-Fe	Nickel-Chrome-Iron
NPS	Nominal Pipe Size
NRC	Nuclear Regulatory Commission
NWC	Normal Water Chemistry
OD	Outer Diameter
ORNL	Oak Ridge National Laboratory
ppb	Parts Per Billion
ppm	Parts Per Million
PSB	Persistent Slip Band
PVRC	Pressure Vessel Research Council
PWR	Pressurized Water Reactor
RCS	Reactor Coolant System
RG	Regulatory Guide
RHR	Residual Heat Removal
RMS	Root Mean Square
RT	Room Temperature
S	Sulfur

## **ABBREVIATIONS (concluded)**

---

SICC	Strain Induced Corrosion Cracking
SS	Stainless Steel
T	Temperature
TENPES	Thermal and Nuclear Power Engineering Society
TG	Transgranular
TMI	Three Mile Island
UTS	Ultimate Tensile Strength
VTT	Valtion Teknillinen Tutkimuskeskus (Finnish: Technical Research Center of Finland)
VVER	Voda-Vodyanoi Energetichesky Reaktor (Russian pressurized water reactor)
WRC	Welding Research Council
YS	Yield Strength



## **ACKNOWLEDGMENTS**

---

The authors are indebted to the Japan Nuclear Energy Safety Organization (JNES) for sharing their enormous fatigue ( $\epsilon$ -N) database for use in the evaluations documented in this report. The authors are also grateful to Bill Shack for his invaluable input and guidance in preparing this report. The authors acknowledge Yogen Garud for his contributions and helpful comments. This work was co-sponsored by the Office of Nuclear Regulatory Research, U.S. Nuclear Regulatory Commission; Project Manager: Gary L. Stevens and the Electric Power Research Institute (EPRI) as Cooperative Nuclear Safety Research under the Environmentally Assisted Fatigue Effects Addendum to the NRC/EPRI Memorandum of Understanding (MOU), under NRC Job Codes V6069 and V6269.



# 1. INTRODUCTION

---

The structural integrity of a metal component may gradually degrade when it is subjected to cyclic loading, even at magnitudes less than the design static loads, due to a well-known degradation mechanism called fatigue. The mechanism of fatigue damage can occur in flaw-free components by developing cracks during service. The American Society of Mechanical Engineers (ASME) Boiler and Pressure Vessel Code Section III, Subsection NB, which contains rules for the design of Class 1 components for nuclear power plants, recognizes fatigue as a possible mode of failure in pressure vessel steels and piping materials. Fatigue is a major consideration in the design of rotating machinery and aircraft, where the components are subjected to a very large number of cycles, i.e., high-cycle fatigue. In these situations, the primary concern is the endurance limit, which is the stress level below which an infinite number of cycles can be applied without fatigue failure. However, cyclic loadings on a reactor pressure boundary component occur because of changes in mechanical and thermal loadings as the system goes from one load state to another. The number of cycles applied during the design life of the component seldom exceeds 100,000 and is typically less than a few thousand (e.g., low-cycle fatigue). The main difference between high-cycle and low-cycle fatigue is that the former involves little or no plastic strain, whereas the latter involves strains in excess of the yield strain. Therefore, design curves for low-cycle fatigue are based on tests in which strain rather than stress is the controlled variable.

The ASME Code fatigue evaluation procedures are described in NB-3200, “Design by Analysis,” and NB-3600, “Piping Design.” The ASME Code fatigue analysis considers all transient loads based on the anticipated number of thermal and pressure transients, and for each load-cycle or load set pair, an individual fatigue usage factor is determined by the ratio of the number of cycles anticipated during the lifetime of the component to the allowable cycles. Figures I-9.1 through I-9.6 of Mandatory Appendix I to Section III of the ASME Boiler and Pressure Vessel Code specify fatigue design curves for various materials that define the allowable number of cycles as a function of applied stress amplitude. The cumulative usage factor (CUF) is the sum of the individual usage factors for all load set pairs, and ASME Code Section III requires that at each location the CUF, calculated based on Miner’s rule, must not exceed unity for acceptable fatigue design.

Although the ASME Code Section III rules apply to Class 1 components, those fatigue design rules are sometimes applied to other classes of components to provide a robust fatigue design in situations where known fatigue issues exist or fatigue duty is high [e.g., Class 2 pressurized water reactor (PWR) feedwater nozzles]. As such, the methods described in this report are intended to apply to all components exposed to an LWR environment that utilize the fatigue calculation procedures from ASME Code Section III.

Revision 1 of this report represents a comprehensive and detailed expansion of the Revision 0 manuscript that incorporates significant additional background, test data, and test data descriptions. In addition, the content layout of the report was revised for clarity. As a result, the revisions made to the Revision 0 manuscript are not specifically identified throughout the text of this revision.

## 1.1 Definition of Fatigue Life

Before discussing the fatigue design curves used in the ASME Code Section III fatigue CUF analysis, it is important to first define “fatigue life” in terms of its use in this report. In the American Society for Testing and Materials (ASTM) Designation E 1823-09a<sup>1</sup> “Standard Terminology Relating to Fatigue and Fracture Testing,” fatigue life is defined as “the number of

cycles of a specified character that a given specimen sustains before failure of a specified nature occurs. Fatigue life, or the logarithm of fatigue life, is a dependent variable.” Accordingly, the ASME Code fatigue design curves [i.e., stress amplitude ( $S_a$ ) vs. number of cycles ( $N$ ) curves] are generally considered to represent allowable number of cycles to failure. However, note that ASTM E1823 states that fatigue life is “failure of a specified nature.” Furthermore, Section 8.9 of ASTM Standard E 606-04<sup>2</sup> “Standard Practice for Strain-Controlled Fatigue Testing,” states that the definition of failure may vary with the ultimate use of the fatigue life information, and provides the following acceptable alternatives for determination of failure:

- (i) *Separation*: Total separation or fracture of the specimen into two parts at (1) some location within the uniform section of the uniform-gage specimen, or (2) the vicinity of the minimum diameter in the hourglass specimen.
- (ii) *Modulus Method*: For any specified number of cycles,  $N$ , during a fatigue test, the modulus for unloading following a peak tensile stress is defined as  $E_{NT}$  and the modulus for loading following a peak compressive stress is  $E_{NC}$ . Failure is defined as the number of cycles where the ratio  $E_{NT}/E_{NC}$  reaches one-half the value for the first cycle (i.e., is reduced by 50%). However, if total separation occurs first, as in item (i) above, fatigue life is defined by the number of cycles to separation.
- (iii) *Microcracking*: The existence of surface microcracks (e.g., as observed optically or by replicas) that are larger than some preselected size consistent with the test objective.
- (iv) *Force (Stress) Drop*: Failure is defined as the ability of a test specimen to sustain a tensile force (or stress). Failure is often defined as the point at which the maximum force (stress) or elastic modulus (as measured when unloading from a peak tensile stress) decreases by approximately 50% because of the presence of cracks. The exact method and the percentage drop should be documented.

In the fatigue  $\epsilon$ - $N$  data used to develop the original ASME Code best-fit or mean-data curves, failure was primarily defined as total separation or fracture of the specimen into two parts. However, in the fatigue tests performed during the last four decades, failure was defined according to the force (stress) drop method. In most of these tests, fatigue life was defined in terms of the number of cycles for the tensile stress to decrease 25% from its peak or steady-state value (i.e., 25% load drop). For the typical cylindrical specimens used in these studies, this corresponded to the number of cycles needed to produce approximately 3-mm-deep cracks in test specimens. Thus, the fatigue life of a material was described in terms of three parameters, viz., strain or stress, cycles, and crack depth. The best-fit curve to the existing fatigue  $\epsilon$ - $N$  data describes, for a given strain or stress amplitude, the number of cycles needed to develop a 3-mm deep crack. Note that, for consistency, all data used in this report were adjusted to be on an equivalent 25% load drop basis as discussed at the beginning of Chapter 3.

Based on the foregoing and the results of the majority of the test data evaluated, fatigue life is described in this report as the number of cycles of a specified strain amplitude that a specimen can sustain before the formation of a 3-mm-deep crack (i.e., an “engineering crack”). This equates to a 25% load drop in test specimens, and is assumed to equate to crack initiation in an actual component. Using this definition, a calculated fatigue CUF less than unity provides reasonable assurance that a fatigue crack has not formed in a component, and indicates that the probability of forming a crack in the component is low.

## 1.2 Air Fatigue Design Curves in Section III of the ASME Code

The ASME Code fatigue design curves, as given in Mandatory Appendix I of Section III, are based on strain-controlled tests of small polished specimens at room temperature in air. The data are typically obtained from fatigue tests conducted in accordance with ASTM Designation E 606-04 “Standard Practice for Strain-Controlled Fatigue Testing.” This practice covers the determination of fatigue properties of nominally homogeneous materials by the use of uniform gage section specimens subjected to axial strain-controlled, fully reversed (strain ratio, R, equal to -1) cycling. The practice is also applicable to hourglass specimens. The practice may be adapted to guide more general testing where strain or temperature may be varied according to application specific histories. The presentation and analysis of data are performed in accordance with ASTM Standard E 468, “Standard Practice for Presentation of Constant Amplitude Fatigue Test Results for Metallic Materials”<sup>3</sup> and ASTM Standard E 739, “Standard Practice for Statistical Analysis of Linear or Linearized Stress-Life (S-N) and Strain-Life ( $\epsilon$ -N) Fatigue Data.”<sup>4</sup> The guidance in Metals Handbook, Volume 8, “Fatigue Data Analysis”<sup>5</sup> can also be used. The definitions of terms related to fatigue testing are described in ASTM Standard E 1823, “Standard Terminology Relating to Fatigue and Fracture Testing.”<sup>6</sup>

The design curves were developed from the best-fit curves to the experimental fatigue-strain-vs.-life ( $\epsilon$ -N) data, which are expressed in terms of the Langer equation<sup>7</sup> of the form

$$\epsilon_a = A1(N)^{-n1} + A2, \quad (1)$$

where  $\epsilon_a$  is the applied strain amplitude, N is the fatigue life, and A1, A2, and n1 are coefficients of the model. Equation 1 may be written in terms of stress amplitude  $S_a$  instead of  $\epsilon_a$ . The stress amplitude is the product of  $\epsilon_a$  and elastic modulus E, i.e.,  $S_a = E \cdot \epsilon_a$  (stress amplitude is one-half the applied stress range). The current ASME Code best-fit or mean curve described in the Section III criteria document<sup>8</sup> for various steels is given by

$$S_a = \frac{E}{4\sqrt{N_f}} \ln\left(\frac{100}{100 - A_f}\right) + B_f, \quad (2)$$

where E is the elastic modulus (MPa),  $N_f$  is the number of cycles to failure, and  $A_f$  and  $B_f$  are constants related to reduction in area in a tensile test (percent) and endurance limit of the material at  $10^7$  cycles (MPa), respectively.<sup>7</sup> The current Code mean curves were obtained from Eq. 2 and  $A_f$  and  $B_f$  values of 68.5% and 149.2 MPa, 61.4% and 265.4 MPa, and 72.6% and 299.9 MPa, respectively, for carbon steels, low-alloy steels, and austenitic stainless steels (SSs).<sup>8</sup> Thus, using an elastic modulus of 206,843 MPa for carbon and low-alloy steels and 179,264 MPa for austenitic SSs, the mean curves are expressed for carbon steels, as

$$S_a = 59,734 (N_f)^{-0.5} + 149.2, \quad (3)$$

for low-alloy steel, as

$$S_a = 49,222 (N_f)^{-0.5} + 265.4, \quad (4)$$

and for austenitic SSs, as

$$S_a = 58,020 (N_f)^{-0.5} + 299.9. \quad (5)$$

The fatigue  $\epsilon$ - $N$  data are typically expressed by rewriting Eq. 1 as

$$\ln(N) = A - B \ln(\epsilon_a - C), \quad (6)$$

where  $A$ ,  $B$ , and  $C$  are constants;  $C$  represents the fatigue limit of the material; and  $B$  is the slope of the log-log plot of fatigue  $\epsilon$ - $N$  data. The ASME Code mean-data curves (i.e., Eqs. 3-5) may be expressed in terms of Eq. 6 as follows. The fatigue life of carbon steels is given by

$$\ln(N) = 6.726 - 2.0 \ln(\epsilon_a - 0.072), \quad (7)$$

for low-alloy steels, by

$$\ln(N) = 6.339 - 2.0 \ln(\epsilon_a - 0.128), \quad (8)$$

and, for austenitic SSs, the fatigue life corresponding to the fatigue design curve originally published in Section III of the ASME Code prior to the 2009b Addenda is given by

$$\ln(N) = 6.954 - 2.0 \ln(\epsilon_a - 0.167), \quad (9)$$

and, as derived in Section 3.2.6, the fatigue life corresponding to the fatigue design curves in 2009b Addenda and later editions of the ASME Code, by

$$\ln(N) = 6.891 - 1.920 \ln(\epsilon_a - 0.112), \quad (10)$$

where strain amplitude  $\epsilon_a$  is in percent. The  $\epsilon$ - $N$  curve for austenitic SSs is also used for nickel-chromium-iron (Ni-Cr-Fe) alloys (e.g., Alloy 600).

The best-fit or mean-data curves (e.g., Eqs. 7-10) provide an estimate of the fatigue life that would lead to failure in 50% of the population under a given loading. However, as discussed later in this report, the ASME Code fatigue design curves are now defined to estimate acceptable fatigue life for at least 95% of the population under a given loading.

Another term that is often used in ASME Section III fatigue evaluations is fatigue limit (or endurance limit), which is defined as<sup>1</sup> “the limiting value of the median fatigue strength as the fatigue life,  $N_f$ , becomes very large.” However, certain materials (e.g., carbon and low-alloy steels and austenitic SSs) and environments preclude the attainment of a fatigue limit. Therefore, in the literature, fatigue limit is typically defined as a value of stress,  $S_N$ , for failure at a specified number of cycles,  $N$  (e.g., at  $10^6$  or  $10^{11}$  cycles).

The above  $\epsilon$ - $N$  curves describe the formation of engineering fatigue cracks in small, smooth test specimens in an air environment. To use the small-specimen data for actual reactor components, the best-fit  $\epsilon$ - $N$  curves for specimen data must be adjusted to account for the effects of variables that are known to affect fatigue life but were not accounted for in the small-specimen data. Such variables include mean stress, surface finish, size, and loading history. Furthermore, the best-fit curve represents the average behavior of the material. To obtain a curve that assures a low probability for formation of fatigue cracks, the small specimen curve must also be adjusted to account for data scatter and material variability.

The procedure used to develop the ASME Code fatigue design curves from the best-fit (or mean-data) curves for small specimens is as follows. First, the best-fit curves are adjusted to account for the effects of mean stress. This is necessary to account for mean stress effects not

considered during specimen testing, such as weld residual stress. Mean stress was accounted for using the modified Goodman relationship given by

$$S'_a = S_a \left( \frac{\sigma_u - \sigma_y}{\sigma_u - S_a} \right) \quad \text{for } S_a < \sigma_y, \quad (11)$$

and

$$S'_a = S_a \quad \text{for } S_a > \sigma_y, \quad (12)$$

where  $S'_a$  is the adjusted value of stress amplitude, and  $\sigma_y$  and  $\sigma_u$  are yield and ultimate strengths of the material, respectively. Equations 11 and 12 assume the maximum possible mean stress and typically give a conservative adjustment for mean stress. The original ASME Code Section III fatigue design curves were obtained by reducing the fatigue life at each point on the adjusted best-fit curve by a factor of 2 on strain (or stress) or 20 on cycles, whichever was more conservative.

As described in the Section III criteria document,<sup>8</sup> the factors of 2 and 20 are not safety margins, but rather adjustment factors that were applied to the small-specimen data to account for the effects of variables that are known to affect fatigue life but were not accounted for in the small-specimen data. These factors include (a) data scatter and material variability, (b) the differences in surface condition and size between the test specimens and actual reactor components, and (c) random load cycles as compared to constant strain cycles used to obtain the fatigue  $\epsilon$ -N data.

### 1.3 Subfactors Included in ASME Section III Air Fatigue Design Curves

In comments about the initial scope and intent of the ASME Code Section III fatigue design procedures, Cooper<sup>9</sup> states that the factor of 20 on life was regarded as the product of three subfactors:

Scatter of data (minimum to mean)	2.0
Size effect	2.5
Surface finish, atmosphere, etc.	4.0

Although the ASME Code Section III criteria document<sup>8</sup> states that these factors were intended to cover such effects as environment, Cooper<sup>9</sup> further states that the term “atmosphere” was intended to reflect the effects of an industrial atmosphere in comparison with an air-conditioned laboratory, which are different than the effects of a specific coolant environment. In addition, surface finish represented surface roughness of industrial-grade component surface compared to that of a polished test specimen. Subsubarticle NB-2160 (or Subsubarticle NG-2160 for core support structures) of Section III of the ASME Code states, “It is the responsibility of the Owner to select material suitable for the conditions stated in the Design Specifications (NCA-3250), with specific attention being given to the effects of service conditions upon the properties of the material.” The minimum contents of the Design Specifications are specified in Paragraph NCA-3252 of Section III of the ASME Code. Paragraph NCA-3252(a)(3) states that the Design Specifications shall include “the environmental conditions, including radiation.” The environmental conditions that are likely to influence the properties of materials used in nuclear

power plant structures and components include temperature, reactor coolant environment, and neutron irradiation.

Furthermore, Paragraph NB-3121 of Section III of the ASME Code (or Paragraph NG-3121 for core support structures) states, “It should be noted that the tests on which the fatigue design curves (Figs. I-9.0) are based did not include tests in the presence of corrosive environments which might accelerate fatigue failure.” Paragraph B-2131 in Nonmandatory Appendix B to Section III, “Owner’s Design Specifications,” states that the Owner’s Design Specification should provide information about, “any reduction to design stress intensity values, allowable stress, or fatigue design curves that is necessitated by environmental conditions.”

### 1.3.1 Effects of Reactor Coolant Environment on Fatigue Lives

Existing fatigue  $\epsilon$ - $N$  data (Fig. 1) illustrate potentially significant effects of light water reactor (LWR) coolant environments on the fatigue resistance of carbon and low-alloy steels, wrought and cast austenitic SSs, and Ni-Cr-Fe alloys.<sup>10-75</sup> Small-scale laboratory fatigue test data indicate that under certain reactor operating conditions, fatigue lives of carbon and low-alloy steels can be a factor of 17 lower in the coolant environment than in air. Therefore, the factors in the ASME Code may be less conservative than originally intended.

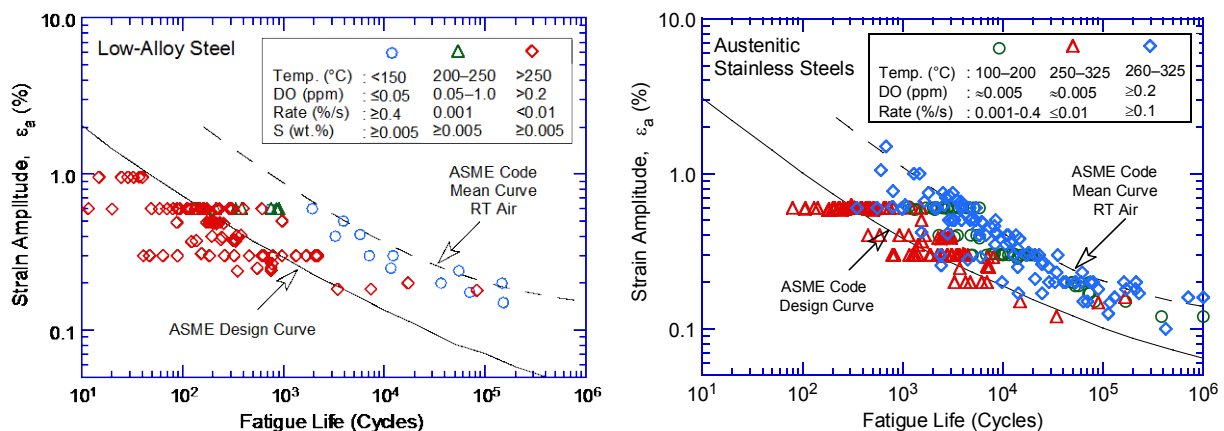


**Figure 1. Fatigue  $\epsilon$ - $N$  data for low-alloy steels and austenitic stainless steels in water compared to ASME Air Design Curve; RT = room temperature.**

The fatigue  $\epsilon$ - $N$  data are consistent with the much larger database on enhancement of crack growth rates (CGRs) in these materials in simulated LWR environments. The key parameters that influence fatigue life in these environments are temperature, the dissolved-oxygen (DO) level in the water, strain rate, strain (or stress) amplitude, and, for carbon and low-alloy steels, the sulfur content of the steel. The range of the values for these parameters within which environmental effects are significant has also been defined. If these critical loading and environmental conditions exist during reactor operation, then environmental effects may be significant and should be included in any associated ASME Code fatigue evaluations. Experience with nuclear power plants worldwide indicates that the critical range of loading and environmental conditions that leads to environmental effects on formation of fatigue cracks can and do occur during plant operation.<sup>56,76-92</sup> It therefore is important that component design include consideration of environmental effects to prevent premature fatigue failures.

Experience with operating nuclear power plants worldwide reveals that many failures of reactor components were attributed to fatigue; examples include piping, nozzles, valves, and pumps.<sup>76-83</sup> In most cases, these failures were associated with thermal loading due to thermal

stratification and striping, or mechanical loading due to vibratory loading. In piping components, several failures were associated with thermal loading due to thermal stratification and striping. Thermal stratification was typically caused by the injection of low-flow, relatively cold feedwater during plant startup, hot standby, and variations below 20% of full power, whereas thermal striping was caused by rapid, localized fluctuations of the interface between hot and cold feedwater.

Thermal loading due to flow stratification or striping was not typically included in the original design basis analyses for most U.S. nuclear power plants. Regulatory evaluation indicated that high-cycle thermal-stratification loading can occur in PWR surge lines as a result of in-surge and out-surge during heatup/cool-down transients.<sup>93</sup> During heatup or cool-down, when the pressurizer water is heated to approximately 227°C (440°F), the hotter water can flow at a very low rate from the pressurizer through the surge line to the hot-leg piping over the cooler water layer in the piping. The thermal gradients between the upper and lower parts of the pipe can be as high as 149°C (300°F). As a result, all U.S. PWRs performed revised fatigue analyses to address thermal stratification effects in surge lines. Furthermore, the effect of these loadings may also be aggravated by corrosion effects due to a high-temperature aqueous environment. The increased fatigue duty caused by such thermal loading increases the importance of evaluating environmental effects.

The mechanism of cracking in feedwater nozzles and piping was attributed to corrosion fatigue or strain-induced corrosion cracking (SICC).<sup>84-86</sup> Case histories and identification of conditions that lead to SICC of low-alloy steels in LWR systems were summarized by Hickling and Blind. A review of significant occurrences of corrosion fatigue damage and failures in various nuclear power plant systems was presented in an Electric Power Research Institute (EPRI) report.<sup>56</sup> An assessment of the U.S. experience related to PWR primary system leaks observed during the period 1985 through 1996 was presented by Shah et al.<sup>88</sup>

Hirschberg et al. summarized the operating experience regarding thermal fatigue of non-isolable piping connected to PWR reactor coolant system (RCS).<sup>87</sup> Significant cracking occurred in non-isolable sections of the safety injection system and residual heat removal (RHR) system piping connected to the PWR coolant system.<sup>89,90</sup> At Farley, cracking occurred in the heat affected zone (HAZ) of the weld between the first elbow and the horizontal pipe, ≈0.9 m (36 in.) from the RCS cold-leg nozzle. At Tihange, the crack was located in the base metal of an elbow, ≈0.6 m (24 in.) from the RCS hot-leg nozzle. At the Genkai plant, cracking occurred in the RHR suction line at the weld between the first elbow downstream of the hot-leg nozzle and the horizontal pipe section. Cracking due to thermal fatigue also occurred in the safety injection system at Dampierre 1 and 2 plants, and in the chemical and volume control system (CVCS) in Obrigheim plant. In all cases, thermal cycling was caused by interaction of hot RCS fluid from turbulent penetration at the top of the pipe, and cold valve leakage fluid that stratified at the bottom of the pipe. At Genkai, the valve internals alternately shrunk and expanded causing periodic leakage of hot fluid through the stem packing and leak-off line into the elbow.

Thermal stratification, however, can occur even in the absence of valve leakage. The results of fatigue monitoring indicate that many PWR plants measured thermal-stratification cycling in the RHR suction line because of turbulence penetration of the hot leg fluid extending into the horizontal pipe section, which then stratified due to normal convection.<sup>87</sup> For thermal stratification, the length of the vertical pipe section of the RHR suction line must be short enough for the hot fluid to reach the horizontal pipe section, and the length of the horizontal pipe section must be long enough to cause sufficient heat losses for stratification to develop. A

typical temperature gradient of 49°C (120°F) was observed for typical cases of stratification, and temperature gradients as high as 177°C (350°F) were measured in some plants.

Non-isolable leaks due to thermal-stratification cycling also occurred in reactor coolant loop drain lines, excess letdown lines, and makeup/high pressure injection lines at the Three Mile Island (TMI), Loviisa 2, Mihama, and Oconee plants.<sup>87,88</sup> A leak in the cold-leg drain line [1.5 in. or 2 in. National Pipe Size (NPS)] occurred in the weld between the first elbow downstream of the loop nozzle and the horizontal pipe section at TMI, and in the elbow extrados at Oconee. In both cases, thermal stratification was caused by turbulence penetration of the RCS fluid periodically extending into the horizontal section and, because the pipe was not insulated, it stratified due to heat loss. The same mechanism caused a leak in the 2 in. NPS excess letdown line at Mihama. Whereas the Mihama line was insulated, stratification still occurred because the length of the horizontal section to the isolation valve was very long, resulting in significant heat loss.

Thermal fatigue caused leaks in a connecting pipe and shell of the regenerative heat exchanger in the CVCS at Tsuruga 2,<sup>91,92</sup> and in a 250-mm pipe section of the heat exchanger bypass on the RHR system at Civaux 1.<sup>76</sup> Thermal-hydraulic mock-up tests indicate that at Tsuruga, superposition of low-frequency temperature gradients due to changes in the flow pattern and high frequency temperature fluctuations due to mixing of the bypass flow and main flow caused thermal fatigue.<sup>91,92</sup>

Cracking also occurred in austenitic SS channel heads in an experimental test loop used for stress corrosion cracking studies in a simulated PWR environment.<sup>94</sup> Cracks were observed in a region that was subjected to temperature fluctuations between 170 and 190°C at a frequency of 0.05 Hz. The cracks initiated on the inner surface; the cracking morphology was essentially transgranular with fatigue-like striations visible in some regions of the fracture surface. Thermal fatigue, with possible effects of the PWR coolant environment, was concluded to be the root cause of these failures.<sup>94</sup>

Such cracking in non-isolable pipe sections due to thermal cycling was generally termed as high-cycle fatigue, i.e., it occurs at stress levels that correspond to allowable fatigue cycles of  $10^5$  or higher. The current understanding of turbulent penetration is not sufficient to accurately predict the frequency of thermal cycling associated with that phenomenon. Environmental effects on fatigue crack initiation may be significant in low-DO water at stress levels above the threshold value and at strain rates less than 0.4 %/s.

Lenz et al.<sup>85</sup> showed that in feedwater lines, the strain rates are  $10^{-3}$ – $10^{-5}$ %/s due to thermal stratification and  $10^{-1}$ %/s due to thermal shock. They also reported that thermal stratification is the primary cause of crack initiation due to SICC. Stephan and Masson<sup>95</sup> subjected a full-scale mock-up of the steam generator feedwater system to various regimes of stratification. After 4000 cycles of applied loading, destructive examination performed between two locations where stable states of stratification occurred revealed small cracks, 1.4–2.0 mm deep, in the weld region. The fatigue usage factors calculated with elastic and cyclic elastic-plastic computations gave values of 1.3–1.9. Because the average DO level in the water was approximately 5 ppb, which corresponds to the maximum admissible value under normal operating conditions (power greater than 25% nominal power) in French PWRs, environmental effects on life were expected to be minimal and environmental correction factors were not applied in the computations of the fatigue usage factor.

Full-scale mock-up tests to generate thermal stratification in a pipe in a laboratory confirmed the applicability of laboratory data to component behavior.<sup>96</sup> The material, loading, and

environmental conditions were simulated on a 1:1 scale using only thermo-hydraulic effects. Under the conditions of strain rate and strain range typical of thermal stratification in these piping systems, the coolant environment has a significant effect on fatigue crack initiation.<sup>12,29,30</sup>

Finally, a study conducted on SS pipe bend specimens in simulated PWR primary water at 240°C concluded that reactor coolant environment has a significant effect on the fatigue life of SSs.<sup>97-99</sup> Relative to fatigue lives in an inert environment, lives in a PWR environment at strain amplitudes of 0.4% and 0.6% were decreased by factors of 2.9 and 1.4 at strain rates of 0.0005 %/s and 0.01 %/s, respectively. These values show very good agreement with the values predicted from the Argonne National Laboratory (ANL) models presented later in this report for incorporating environmental effects into the ASME Code Section III fatigue evaluations.

### 1.3.2 Effects of Neutron Irradiation

The potential effects of neutron irradiation on the fatigue life of reactor structural materials such as low-alloy pressure vessel steel, austenitic stainless steels, and Ni-Cr-Fe alloys and their weld metals are not fully characterized. Irradiation effects were not included in the ASME Code Section III fatigue evaluations performed for reactor core support structures and reactor internal components. The majority of the existing data on the effects of neutron irradiation resulted from fatigue crack growth tests on austenitic SSs that were irradiated in fast reactors [primarily Experimental Breeder Reactor II (EBR-II)] at test temperatures of 427 (800°F) and 593°C (1100°F).<sup>100-104</sup> The CGR test results indicated that for Type 304 and 316 SS irradiated at 405-410°C (760-770°F) to  $1.2 \times 10^{22}$  n/cm<sup>2</sup> ( $E > 0.1$  MeV) fluence, the fatigue CGRs at 427°C (800°F) were up to a factor of 2 higher than those for unirradiated material at low values of stress intensity factor range ( $\Delta K$ ) [less than 40 ksi in.<sup>1/2</sup> (43.9 MPa m<sup>1/2</sup>)], but were lower for higher  $\Delta K$  values. These observations were reversed at 593°C (1100°F). Crack growth rates were comparable or lower at higher values of  $\Delta K$ . A similar behavior was observed for Type 316 weld metal. Tests on Type 304 and 316 SS irradiated in a thermal reactor [Advanced Test Reactor (ATR)] at 288°C (550°F) to  $1.8 \times 10^{21}$  n/cm<sup>2</sup> ( $E > 0.1$  MeV) and tested at 427°C (800°F) showed superior resistance to crack growth; CGRs were 25 to 50% lower than those for unirradiated material.<sup>105</sup> Based on these studies EPRI concluded,<sup>106</sup> “The work of several researchers suggest that neutron irradiation does not result in a further reduction in fatigue properties and in some cases suggest an improvement.”

Other limited fatigue  $\epsilon$ - $N$  data on materials irradiated under LWR conditions and tested at LWR operating temperatures also showed significant differences in the microstructure and microchemistry of LWR irradiated materials, and materials irradiated in fast neutron test reactors. Specifically, cavities and helium (He) bubbles were observed in austenitic SSs irradiated at a temperature of 320°C (608°F) to high neutron fluence levels in PWRs. Such microstructures could lead to embrittlement of the material.<sup>107</sup> Therefore, fatigue data on LWR irradiated materials should be developed to further quantify the effects of neutron irradiation on fatigue lives.

Fatigue  $\epsilon$ - $N$  data on irradiated Type 308 SS weld metals showed moderate decreases in fatigue lives in the low-cycle regime and superior fatigue lives in the high-cycle regime.<sup>108</sup> Similar effects from neutron irradiation were also observed on the room-temperature fatigue  $\epsilon$ - $N$  behavior of Type 347 SSs irradiated in the Engineering Test Reactor (ETR) at 60°C (140°F) to total integrated fast flux ( $> 1$  MeV) exposures of  $5.5 \times 10^{25}$ ,  $1.1 \times 10^{26}$ , and  $1.6 \times 10^{26}$  n/m<sup>2</sup>, as shown in Fig. 2a.<sup>109</sup> Neutron irradiation decreased the room-temperature fatigue lives of Type 347 SSs at high strain amplitudes (above 0.35%) and had beneficial effects on fatigue lives at low strain amplitudes (below 0.25%). The decreases in fatigue lives increased with increased

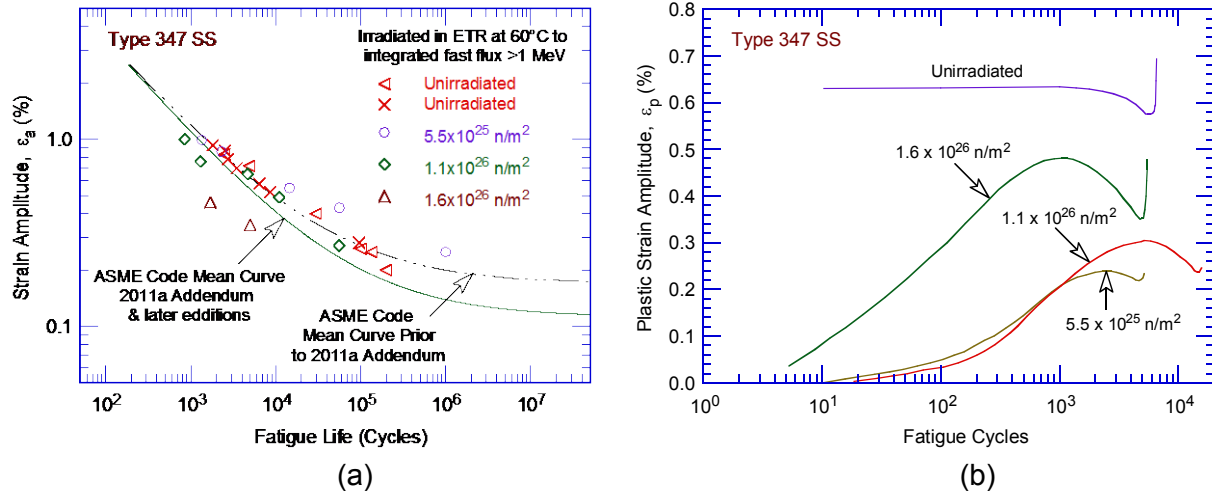


**Figure 2. The effects of neutron irradiation on fatigue lives of Type 347 SSs at room temperature: (a) the fatigue  $\epsilon$ - $N$  behavior, and (b) variations in plastic strain amplitude as a function of fatigue cycles (Ref. 109).**

total neutron doses. The reductions in fatigue lives were likely related to the irradiation-induced decreases in ductility of the materials.

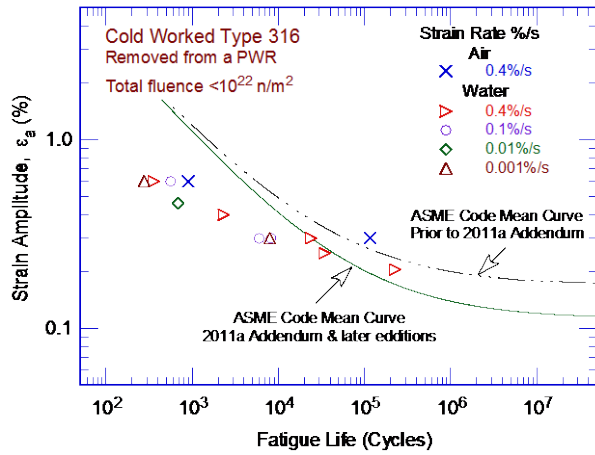
The fatigue test results also indicated significant differences in the cyclic hardening behavior of the irradiated materials relative to unirradiated materials. Typically, at room temperature, austenitic SSs exhibited strain softening after the initial cyclic hardening during the first ten cycles. For the irradiated Type 347 SSs, although total strain was held constant, the plastic strain varied significantly during the fatigue tests, as shown in Fig. 2b. The plastic strains were insignificant initially and increased gradually during the fatigue tests due to strain softening until a later stage where plastic strains started to decrease due to secondary strain hardening and formation of fatigue cracks in the specimens. The extent of strain softening increased with increased neutron doses (Fig. 2b). The rapid increases in plastic strains near the end of the tests were associated with specimen fracture. In contrast, the unirradiated Type 347 SSs exhibited slight strain hardening and plastic strain decreased at a very low rate; later, the materials also showed faster decreases in plastic strains because of secondary strain hardening and formation of fatigue cracks. Thus, the impact of irradiation on fatigue life is not readily apparent from these data because of several competing factors.

The fatigue  $\epsilon$ - $N$  data on cold-worked (CW) Type 316 SS tube materials and solution-annealed Type 304 bar materials removed from an operating PWR are shown in Figs. 3 and 4, respectively.<sup>110</sup> The data were obtained in simulated PWR water at 325°C (617°F) on CW Type 316 SS tube specimens with a 6.48 mm outer diameter and a 0.71 mm wall thickness. The tube specimens were irradiated to fluence values of less than  $10^{22}$ ,  $2 - 6 \times 10^{25}$ , and greater than  $3 \times 10^{26}$  n/m<sup>2</sup> ( $E > 0.1$  MeV), while the 5.08-mm diameter cylindrical specimens of Type 304 SS were irradiated to fluence levels ranging from  $5 \times 10^{25}$  to  $10^{26}$  n/m<sup>2</sup> ( $E > 0.1$  MeV). However, the baseline fatigue data for the unirradiated materials for the same heats of SSs were not available. To determine the possible effects of specimen configuration (i.e., solid cylindrical vs. thin-walled tube specimens), fatigue tests using the two specimen geometries were conducted on another heat of CW Type 316 SS in air at 325°C. The results indicated that the fatigue strengths of the solid specimens were 1.4 times those of the cylindrical tube specimens. The ASME Code Section III best-fit mean air curves for austenitic SSs are shown in the plots in Figs. 3 and 4 for comparison. Based on these test results, the authors concluded, “The fatigue life of irradiated SS was longer than that of unirradiated SS in the range of this research, that is,

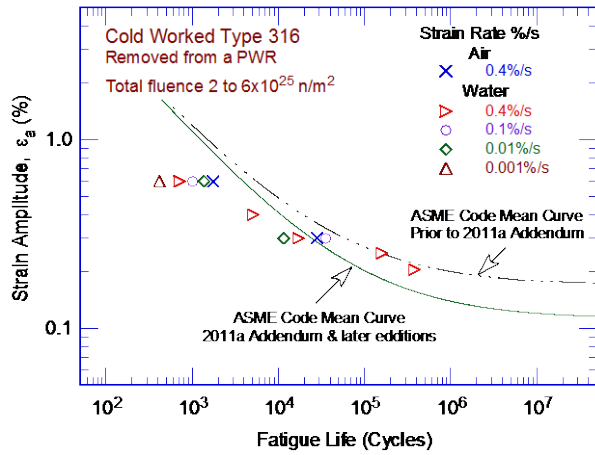
strain amplitude was less than 0.6%. This increase in fatigue strength was considered due to an increase of tensile strength after irradiation.”

In the absence of sufficient baseline fatigue data on unirradiated materials, the above conclusion that the fatigue lives of irradiated materials are longer than those of unirradiated materials is not fully justified. For example, the fatigue lives of irradiated Type 304 SSs in air are close to the ASME Code Section III best-fit mean curves. However, the effects of neutron irradiation are not available because there is insufficient fatigue  $\epsilon$ - $N$  data in air on unirradiated materials for these heats of Type 304 SSs. The fatigue data for irradiated CW Type 316 SSs were obtained on thin-walled tube specimens, and were not consistent with the ASME Code Section III mean air curve for austenitic SSs because the majority of the data were obtained from solid cylindrical specimens. The experimental  $\epsilon$ - $N$  behavior showed a lower  $\epsilon$ - $N$  slope than that for the ASME Code Section III mean curve (Fig. 3). Even after adjusting by a factor of 1.4 on strain to account for the effect of specimen geometry, the fatigue lives in air at 0.3% strain amplitude fall to the right of the ASME Code Section III mean curve, whereas, the fatigue lives at 0.6% strain amplitude are significantly to the left. The primary reason for this inconsistency is likely caused by inadequate specimen size (tube specimens with 0.71-mm thick wall) for fatigue tests performed at high strain amplitudes. However, the fatigue data in Figs. 3 and 4 show that fatigue lives of austenitic SSs were decreased in a PWR primary water environment. Except for the data on CW Type 316 SSs irradiated to a fluence greater than  $3 \times 10^{26}$  n/m<sup>2</sup>, the data for irradiated materials and the data for irradiated Type 304 SSs show lower fatigue lives in PWR primary water environment compared to those in air. The effects of the environment increase with decreasing strain rates.

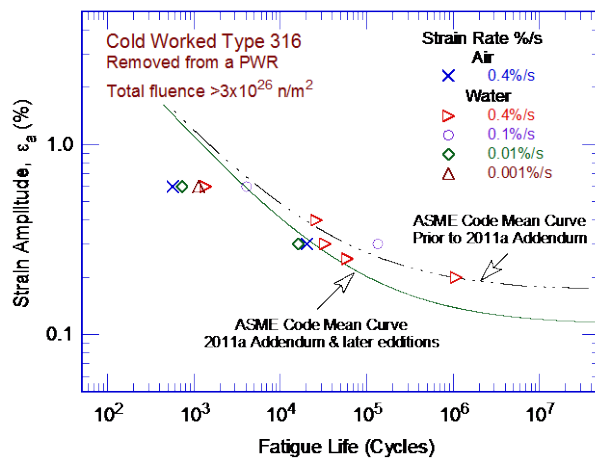
The limited available data are inconclusive with regard to the impact of irradiation on the fatigue lives of materials exposed to LWR environments. Although some small-scale laboratory fatigue  $\epsilon$ - $N$  test data indicate that neutron irradiation decreases the fatigue lives of austenitic SSs, particularly at high strain amplitudes, it is not possible to quantify the impact of irradiation on the prediction of fatigue lives based on the limited data currently available. Additional fatigue data on reactor structural materials irradiated under LWR operating conditions are needed to determine whether there are measurable effects of neutron irradiation on the fatigue lives of these materials and, if so, to better define how those impacts may be quantified. In the absence of such data, the methods described in this report are considered appropriate for application to materials exposed to significant levels of irradiation, such as SS reactor internals components, when mandated by regulation or required by the current licensing basis.



(a)



(b)



(c)

**Figure 3.** Strain amplitude vs. fatigue life data in 325°C air or simulated PWR primary water environments for CW Type 316 SS irradiated to (a) less than  $10^{22}$ , (b)  $2\text{--}6 \times 10^{25}$ , and (c) greater than  $3 \times 10^{26}$  n/m<sup>2</sup> ( $E > 1.0$  MeV) (Ref. 110).

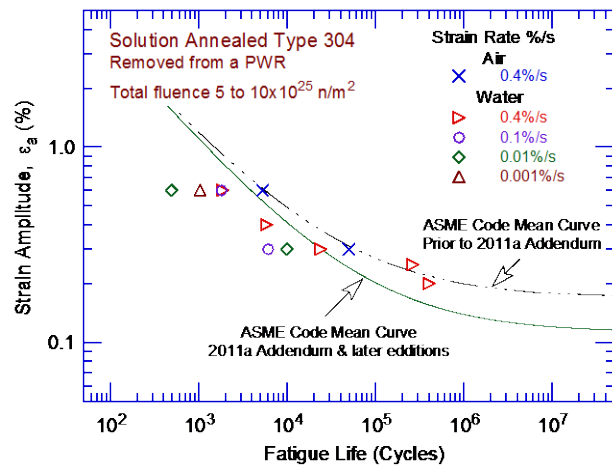


**Figure 4.** Strain amplitude vs. fatigue life data in 325°C air and simulated PWR primary water environments for Type 304 SS irradiated to  $5 \times 10^{25}$ – $10 \times 10^{25}$  n/m<sup>2</sup> ( $E > 0.1$  MeV) (Ref. 110).

## 1.4 Modeling of Environmental Effects

In 1991, the U.S. Nuclear Regulatory Commission (NRC) issued a draft Branch Technical Position (BTP) for fatigue evaluation of nuclear plant components for license renewal. The BTP raised a concern about the adequacy of the ASME Code in addressing environmental effects on fatigue resistance of materials for operating PWRs and boiling water reactors (BWRs), whose primary-coolant pressure boundary components were constructed as specified in Section III of the ASME Code. In 1993, the Commission directed the NRC staff to treat fatigue as a potential safety issue within the existing regulatory process for operating reactors. The staff developed a Fatigue Action Plan (FAP) to resolve three principal issues: (a) adequacy of fatigue resistance of older vintage plants designed to the United States of America Standard B31.1 Code that did not require an explicit fatigue analysis of components, (b) effect of LWR environments on the fatigue resistance of primary pressure boundary materials, and (c) appropriate corrective action required when ASME Code fatigue allowable limits are exceeded, i.e., when the CUF is greater than unity.

The Idaho National Engineering Laboratory (INEL) assessed the significance of ANL-developed interim fatigue design curves, by performing fatigue evaluations of a sample of components in the reactor coolant pressure boundary.<sup>111</sup> In all, six locations were evaluated from facilities designed by each of the four U.S. nuclear steam supply system vendors. Selected components from older vintage plants designed according to the B31.1 Code were also included in the evaluation. Conservatism in the original fatigue evaluations, e.g., actual loading cycles instead of assumed cycles, was removed, and fatigue usage was evaluated with a fatigue design curve that considered the effects of the coolant environment. The results indicated that most of the locations had a CUF of less than the ASME Code limit of 1.0 for 40 years. The risk to reactor-coolant pressure boundary components from failure due to fatigue was assessed under Generic Safety Issue (GSI) 78, "Monitoring of Fatigue Transient Limits for the Reactor Coolant System," and GSI-166, "Adequacy of Fatigue Life of Metal Components."<sup>112</sup> Based on these studies, it was concluded<sup>113</sup> that no immediate action was necessary to address the three fatigue issues identified in the FAP. A risk study indicated that fatigue failure of piping was not a significant contributor to core damage frequency. Based on the risk assessment, a backfit to incorporate environmental effects into the fatigue analyses of operating plants was not justified.<sup>114</sup>

However, because the NRC studies were less certain that the conservatism in the original fatigue calculations could be used to account for an additional 20-years of operation, the NRC staff recommended that environmental effects be considered by evaluating the sample locations in the INEL study (NUREG/CR-6260)<sup>111</sup> for plants pursuing license renewal. These recommendations were documented in GSI-190, "Fatigue Evaluation of Metal Components for 60-year Plant Life."<sup>112</sup> Based on probabilistic analyses and sensitivity studies, interactions with the industry, and various programs available to licensees to manage the effects of aging, it was concluded that no generic regulatory action was required. For some components, although cumulative probabilities of crack initiation and through-wall cracks approached 1.0 for the renewal period, the maximum failure rate was generally low, in the range of  $10^{-2}$  through-wall cracks per year.

In addition, the predicted failure rates were generally associated with high CUF locations and components with thin walls; in most cases, any leakage that might result from these through-wall cracks was estimated to be small and not likely to lead to core damage. However, the calculations that supported the resolution of this issue indicated the potential for an increase in the frequency of pipe leaks as plants continue to operate. Thus, the NRC staff recommended that aging-management programs for license renewal should address component fatigue, including the effects of the reactor coolant environment. It should, however, be noted that when

the INEL study was performed, it was not known that the effects of high-temperature reactor coolant environment on fatigue cracking of austenitic SSs are greater in low-DO environments than in high-DO environments. Thus, the six sample locations evaluated in the INEL study may not necessarily be the bounding locations for some plants, and additional plant-specific component locations than those considered in NUREG/CR-6260 should be included in the fatigue CUF evaluations, including the effects of environment.

In 1991, the ASME Board on Nuclear Codes and Standards (BNCS) requested the Pressure Vessel Research Council (PVRC) to examine the existing worldwide  $\epsilon$ -N data and develop recommendations for the ASME. The PVRC compiled and evaluated fatigue  $\epsilon$ -N data related to the effects of LWR coolant environments on the fatigue life of pressure boundary materials; the results were summarized by Van Der Sluys and Yukawa.<sup>115,116</sup> The staff agreed with the concept of using an environmental correction factor ( $F_{en}$ ) approach to obtain fatigue usage reflecting environmental effects for ASME Code Section III fatigue evaluations. This information was forwarded to the appropriate ASME Code committee.<sup>117</sup>

An analysis of the existing fatigue  $\epsilon$ -N data and the procedures for incorporating environmental effects into ASME Code Section III fatigue evaluations was presented in several review articles<sup>115,116,118-126</sup> and ANL reports.<sup>10,12,13,45-47</sup> The fatigue  $\epsilon$ -N data in air and LWR environments were also examined from the standpoint of fracture mechanics and CGR data.<sup>127,128</sup> Further details are presented in the next section of this report. The key material, loading, and environmental parameters that influence the fatigue lives of carbon, low-alloy, and austenitic stainless steels were identified, and the range of these key parameters where environmental effects are significant, was defined. Two approaches were proposed for incorporating the environmental effects into ASME Section III fatigue evaluations for primary pressure boundary components in operating nuclear power plants: (a) develop new fatigue design curves for LWR applications, or (b) use an environmental fatigue correction factor to account for the effects of the coolant environment.

In the first approach, following the same procedures used to develop the fatigue design curves in ASME Code Section III, environmentally adjusted fatigue design curves were developed from fits to experimental data obtained in LWR environments. Interim fatigue design curves that address environmental effects on the fatigue life of carbon, low-alloy, and austenitic stainless steels were first proposed by Majumdar et al.<sup>129</sup> However, as mentioned above, the "interim" fatigue design curve for austenitic SSs was based on little or no data in low-DO environments. As a result, at the time of the development of the interim design curves, it was not known that the effects of high-temperature reactor coolant environment on fatigue lives are greater in low-DO environments than in high-DO environments. Fatigue design curves based on a more rigorous statistical analysis of experimental data were developed by Keisler et al.<sup>130</sup> These design curves were subsequently revised based on updated ANL models.<sup>10,12,45,46</sup> However, in LWR environments, the fatigue life of carbon and low-alloy steels, Ni-Cr-Fe alloys, and austenitic SSs depends on several loading and environmental parameters. Therefore, such an approach requires development of several design curves to cover all possible environmental conditions encountered during plant operation. Depending on the number of such design curves for the desired loading and environmental conditions, development of additional curves may be a significant undertaking.

The second approach, proposed by Higuchi and Iida in 1991,<sup>19</sup> considers the effects of reactor coolant environments on fatigue life in terms of an environmental fatigue correction factor,  $F_{en}$ , that is defined as the ratio of fatigue life in air at room temperature to that in water under reactor operating conditions. To incorporate environmental effects into fatigue evaluations, this approach required that the fatigue usage factor for a specific stress cycle or load set pair, based

on the ASME Code Section III design fatigue curves, be multiplied by the environmental fatigue correction factor. Specific expressions for  $F_{en}$ , based on the ANL fatigue life models, were developed.<sup>10,45</sup> Such an approach is relatively simple for application to previously-developed fatigue analyses and is recommended in this report. A similar methodology was also developed in Japan by the Environmental Fatigue Data (EFD) Committee of the Thermal and Nuclear Power Engineering Society (TENPES) under the Project on Environmental Fatigue Testing (EFT). The EFT was also supported by the Japan Power Engineering and Inspection Corporation (JAPEIC) and the Japan Nuclear Energy Safety (JNES) Organization, and some utilities.<sup>131-135</sup> Updated technical results were published in a JNES report,<sup>136</sup> JNES-SS-1005 “Environmental Fatigue Evaluation Method for Nuclear Power Plants.” All of that data were considered in the results documented in this report.

In 2007, the original version of NUREG/CR-6909,<sup>137</sup> which is the technical basis document for NRC Regulatory Guide (RG) 1.207, Revision 0, “Guidelines for Evaluating Fatigue Analyses Incorporating the Life Reduction of Metal Components Due to the Effects of the Light Water Reactor Environment for New Reactors,” presented an overview of the existing fatigue  $\epsilon$ - $N$  data for carbon and low-alloy steels, Ni-Cr-Fe alloys, and wrought and cast austenitic SSs in air and LWR environments. The existing fatigue  $\epsilon$ - $N$  data were evaluated to (a) identify the various material, environmental, and loading parameters that influence fatigue cracking, and (b) establish the effects of key parameters on the fatigue lives of these steels. Fatigue life models, presented in earlier reports for estimating fatigue life as a function of material, loading, and environmental conditions were updated using the fatigue  $\epsilon$ - $N$  database available at that time. The report also described the  $F_{en}$  approach for incorporating effects of LWR environments into ASME Section III fatigue evaluations, and presented a critical review of the ASME Code fatigue adjustment factors of 2 on stress (or strain) and 20 on life to assess the possible conservatism in the choice of adjustment factors. The  $F_{en}$  methodology was identified as applicable to all reactor coolant pressure boundary components exposed to reactor water that require an ASME Section III fatigue CUF calculation.

This report presents a revision to the original version of NUREG/CR-6909 in its entirety. The  $F_{en}$  expressions were updated using a much larger fatigue  $\epsilon$ - $N$  database. The additional data include the JNES data summarized in JNES-SS-1005 on carbon and low-alloy steels, wrought and cast austenitic SSs, and Ni-Cr-Fe alloys, and their associated weld metals, tested in air and LWR environments,<sup>136</sup> and fatigue  $\epsilon$ - $N$  test results from the open literature on several heats of carbon and low-alloy steels tested in BWR environments.<sup>138-146</sup> we have not used any bending tests in our environmental effects analysis. Most of the data evaluated for this report were obtained from completely reversed, axial, strain-controlled tests on small laboratory specimens. The results from a small number of bending tests were also considered for austenitic stainless steels in air (see Table 6 in Section 3.2.1), Ni-Cr-Fe alloy steels in air (see Table 9 in Section 3.3), and carbon and low-alloy steels in water (see Table 10 in Section 4.1.1). These data were included to improve the best fit evaluation of the fatigue life data. Section 3.2.2 includes figures that support the use of these bending test data for austenitic stainless steels, which show that the bending test data points fall evenly on both side of the best fit curve of all the data. Only a small number of high-cycle fatigue tests conducted in load control were considered.

The updated environmental fatigue expressions in this report also address comments from interested stakeholders related to: (a) the constants in the  $F_{en}$  expressions that results in a  $F_{en}$  value of approximately 2 even when the strain rate is very high or temperature is very low, (b) the temperature dependence of  $F_{en}$  for carbon and low-alloy steels, and (c) the dependence of  $F_{en}$  on water chemistry for austenitic SSs. Finally, the updated methodology described in this report applies to any component exposed to the LWR environment that requires an ASME CUF

calculation as part of its design, or if required by the safety basis for the component, or if required by the plant current licensing basis, unless otherwise justified.

In addition, the appropriateness of a strain threshold and the possible effects of hold periods were also evaluated. The potential effects of dynamic strain aging (DSA) on cyclic deformation and environmental effects are discussed.<sup>147-153</sup> The  $F_{en}$  methodology proposed in this report was validated by comparing the results of five different experimental data sets obtained from fatigue tests that simulate actual plant conditions with estimates of fatigue usage adjusted for environmental effects using the updated  $F_{en}$  expressions. The five data sets represent fatigue tests with (a) changing strain rate and/or temperature,<sup>154</sup> (b) complex loading (actual PWR transient),<sup>155-157</sup> (c) spectrum loading (random strain amplitudes),<sup>158,159</sup> (d) thermal fatigue of a stepped pipe,<sup>160</sup> and (e) pipe U-bend tests.<sup>98,99</sup> Appendix C of this report presents a sample application of the  $F_{en}$  methodology that is intended to address by example some of the practical issues identified by interested stakeholders associated with the  $F_{en}$  calculations.<sup>161</sup>

## 2. MECHANISM OF FATIGUE

### 2.1 Formation of an Engineering Crack in Air

Deformation and microstructural changes in the surface grains of metals are responsible for fatigue cracking. During cyclic straining, the irreversibility of dislocation glide leads to the development of surface roughness. Strain localization in persistent slip bands (PSBs) results in the formation of extrusions and intrusions. With continued cycling, microcracks ultimately form in PSBs or at the edges of slip–band extrusions. At high strain amplitudes, microcracks form in notches that develop at grain, twin, or phase boundaries (e.g., ferrite/pearlite) or by cracking of second–phase particles (e.g., sulfide or oxide inclusions).

Once a microcrack forms, it continues to grow along its primary slip plane or a PSB as a Mode II (shear) crack in Stage I growth (where the orientation of the crack is usually at  $45^\circ$  to the stress axis). At low strain amplitudes, a Stage I crack may extend across several grain diameters before the increasing stress intensity of the crack promotes slip on planes other than the primary slip plane. A dislocation cell structure normally forms at the crack tip. Because slip is no longer confined to planes at  $45^\circ$  to the stress axis, the crack begins to propagate as a Mode I (tensile) crack, normal to the stress axis in Stage II growth. At high strain amplitudes, the stress intensity is quite large and the crack propagates entirely by the Stage II process. Stage II crack propagation continues until the crack reaches an engineering size. The two stages of fatigue crack growth in smooth specimens are shown in Fig. 5.

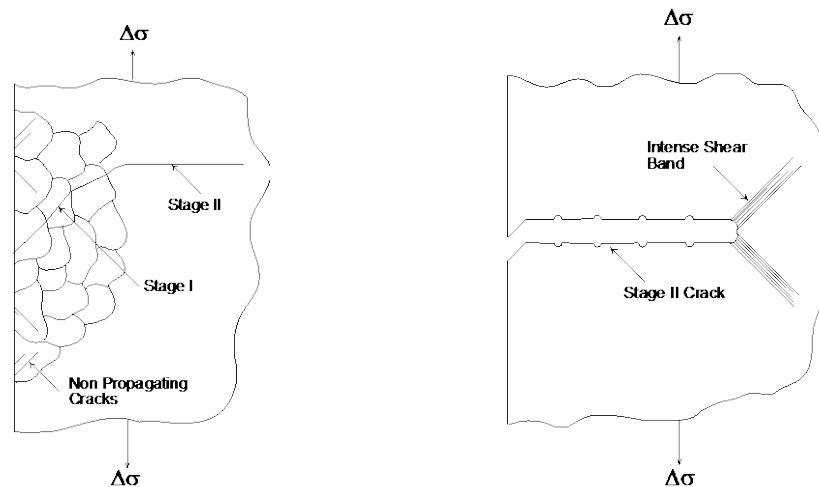
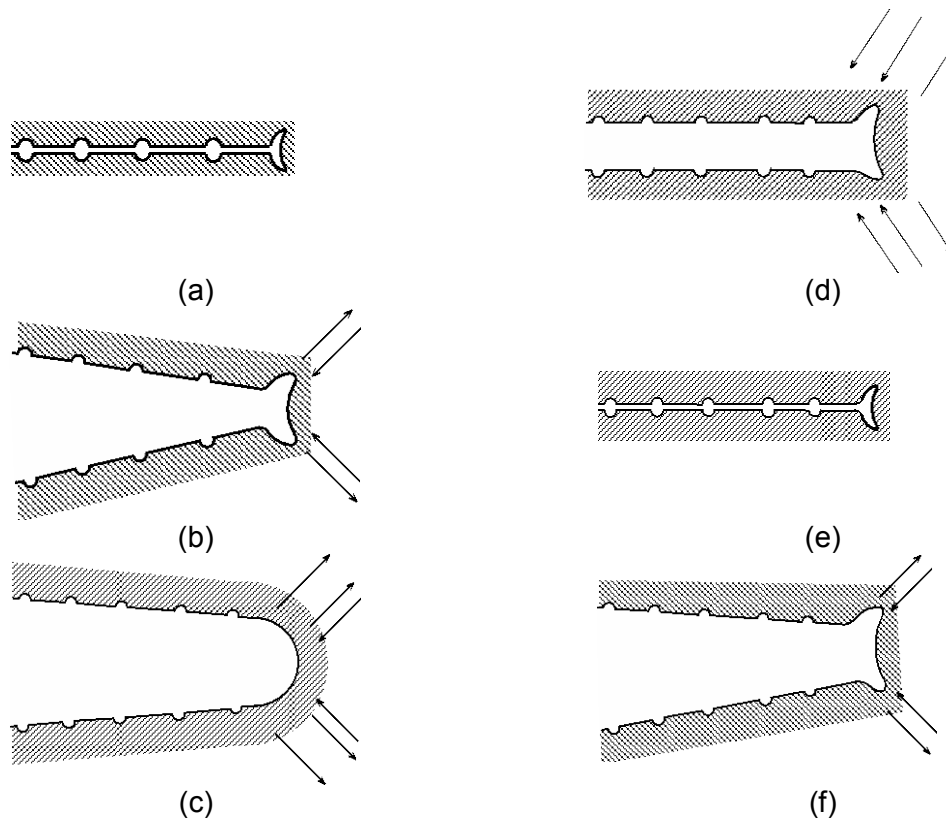


Figure 5. Two stages of fatigue crack growth in smooth test specimens.

In air or mildly corrosive environments, Stage II cracking is characterized by fatigue striations. The process of Stage II fatigue crack growth and formation of fatigue striations<sup>162</sup> is illustrated in Fig. 6. As tensile load is applied, slip bands form at the double notch or “ears” of the crack tip (Fig. 6b). The slip bands widen with further straining, causing blunting of the crack tip (Fig. 6c). Crack surfaces close during compressive loading and slip is reversed, producing ears at the edges of the blunt crack tip (Figs. 6d and 6e). The ears are observed as fatigue striations on the fracture surface. However, there is not necessarily a 1:1 correlation between striation spacing and fatigue cycles. At high strain amplitudes, several striations may be created during one cycle, whereas at low strain amplitudes, one striation may represent several cycles.



**Figure 6. Schematic illustration of the plastic blunting process of fatigue crack growth in Stage II: (a) zero load; (b) small tensile load; (c) maximum tensile load, widening of slip bands; (d) crack closure, and formation of “ears” at crack tip; (e) maximum compressive load; (f) small tensile load in the subsequent cycle.**

Thus, the formation of surface cracks and their growth as shear and tensile cracks (Stages I and II growth) to an “engineering” size (e.g., a 3-mm-deep) crack constitute the fatigue life of a material, which is represented by the fatigue  $\epsilon$ - $N$  curves. Fatigue life is conventionally divided into two stages: initiation, expressed as the number of cycles required to form microcracks on the surface; and propagation, expressed as the number of cycles required to propagate the surface cracks to an engineering size. Thus, the definition of a CUF value of unity, as described in Section 1.1, conventionally includes both initiation and some amount of propagation.

An alternative approach considers fatigue life of engineering structures and components to be entirely composed of the growth of short fatigue cracks, i.e., cracks less than “engineering” size.<sup>163,164</sup> For polycrystalline materials, the time for the formation of surface cracks is negligible. During cyclic loading, surface cracks, 5  $\mu\text{m}$  or longer, form early in life at surface irregularities either already in existence or produced by slip bands, grain boundaries, second-phase particles, etc. (Fig. 7).<sup>11,165-167</sup> Thus, fatigue life may be considered to constitute propagation of cracks from 10 to 3000  $\mu\text{m}$  long, and fatigue damage in a material may be considered as the current size of the fatigue crack.<sup>164</sup> However, the growth rates of short cracks cannot be predicted accurately from fracture mechanics methodology based on the range of stress intensity factor ( $\Delta K$ ) alone. Under the same  $\Delta K$  loading, short fatigue cracks (i.e., cracks having lengths comparable to the unit size of the microstructure) grow at a faster rate than longer fatigue cracks.<sup>168</sup> In addition, shorter cracks can grow at  $\Delta K$  values below those predicted from linear elastic fracture mechanics (LEFM). The differences between the

growth rates of short and long cracks are attributed to interactions with microstructural features, contributions of crack closure with increasing crack length, effects of mixed mode crack propagation, and an inadequate characterization of the crack tip stress/strain fields associated with short cracks.

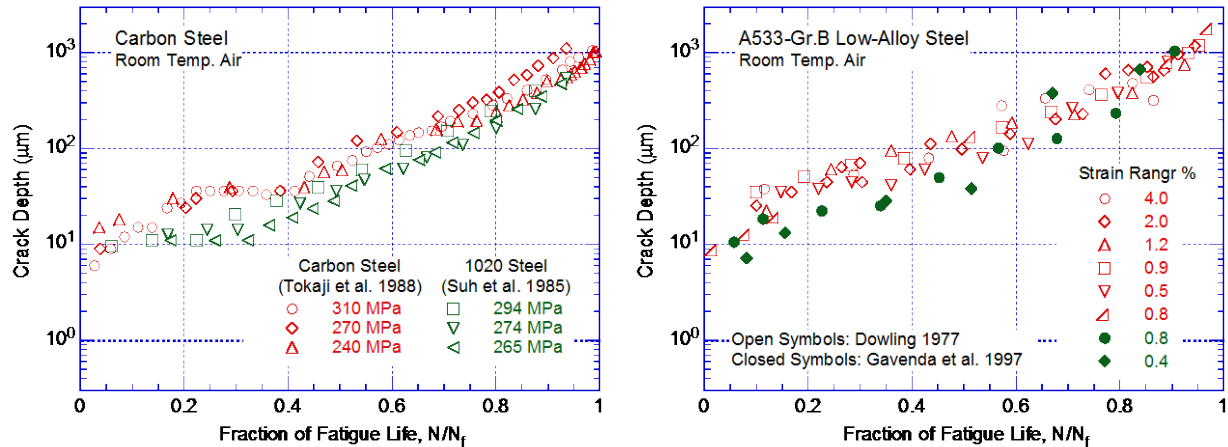


**Figure 7. Crack depth plotted as a function of fractional life for carbon and low-alloy steels tested in air (Refs. 11,165-167).**

A schematic illustration of the two stages of fatigue crack growth including (a) initiation, and (b) propagation, is shown in Fig. 8. The initiation stage involves growth of “microstructurally small cracks” (MSCs), characterized by decelerating crack growth (Region AB in Fig. 8a). The propagation stage involves growth of “mechanically small cracks,” characterized by accelerating crack growth (Region BC in Fig. 8a). The MSCs correspond to Stage-I cracks and grow along slip planes as shear cracks in the early stage of growth. The growth of the MSCs is very sensitive to microstructure.<sup>11,166-171</sup> For MSCs, microstructural effects are strong because of Stage I growth, i.e., crystallographic growth. The growth rates are markedly decreased by grain boundaries, triple points, and phase boundaries. In ferritic-pearlitic steels, fatigue cracks initiate and propagate preferentially in the ferrite phase that forms as long allotriomorphs at prior austenite phase boundaries.<sup>166,170,171</sup> The ferrite/pearlite phase boundaries act as strong barriers to crack propagation, and growth rates decrease significantly when small cracks grow into the pearlite from the ferrite.<sup>166</sup> Limited data suggest that microstructural effects are more pronounced at negative stress ratios; the compressive component of the applied load plays an important role in the formation of Stage I facets and formation of cracks.<sup>169</sup>

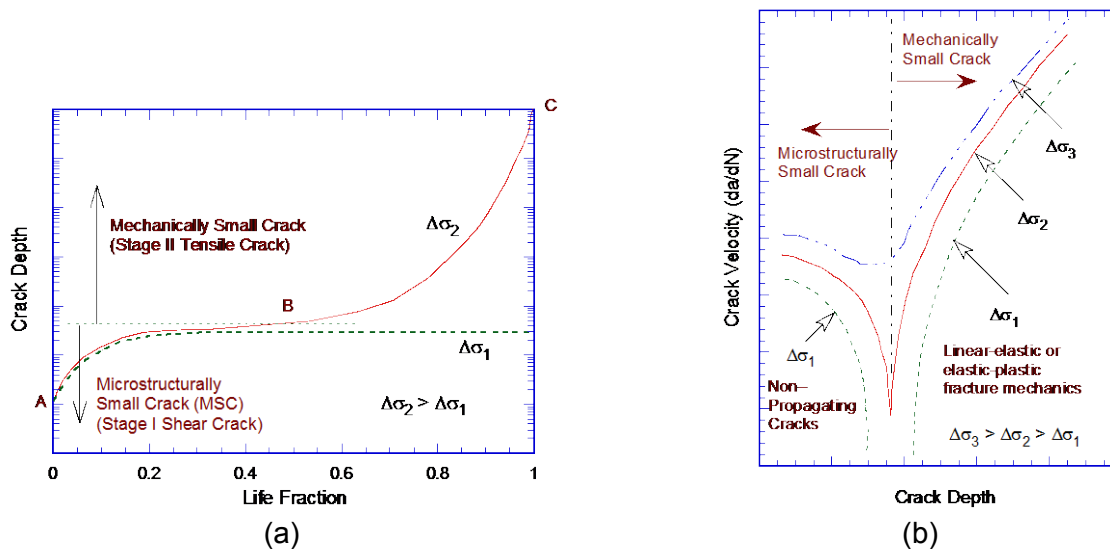


**Figure 8. Schematic illustration of (a) growth of short cracks in smooth specimens as a function of fatigue life fraction, and (b) crack velocity as a function of crack depth.**

Fatigue cracks greater than a critical size, show little or no influence of microstructure and are considered mechanically small cracks.<sup>169</sup> Mechanically small cracks correspond to Stage II (tensile) cracks, which are characterized by striated crack growth, with the fracture surface normal to the direction of maximum principal stress. The growth of mechanically small cracks is characterized in terms of the J-integral range,  $\Delta J$ , and CGR data in air and LWR environments. The CGRs estimated from smooth specimen  $\varepsilon$ -N data show good agreement with CGRs obtained on fracture mechanics compact tension (CT) specimens in air and water environments.<sup>13</sup>

Various criteria, summarized in Section 5.4.1 of Ref. 12, are used to define the crack depth for transition from microstructurally to mechanically small cracks. The transition crack depth is a function of applied stress ( $\sigma$ ) and the microstructure of the material. For completely reversed fatigue straining, the transition from a MSC to a mechanically small crack for several materials is estimated to be approximately 8 times the unit size of the microstructure;<sup>169</sup> actual values may range from 150 to 250  $\mu\text{m}$ .

At low stress levels ( $\Delta\sigma_1$ ) (Fig. 8a), the transition from MSC growth to accelerating crack growth does not occur. This circumstance represents the fatigue limit for a smooth specimen. Although cracks can form below the fatigue limit, they grow to engineering size only at stresses greater than the fatigue limit. The fatigue limit for a material is applicable only for constant loading conditions. Under variable loading conditions, MSCs can grow at high stresses ( $\Delta\sigma_3$ ) (Fig. 8b) to depths larger than the transition crack depth, and then continue to grow at stress levels below the fatigue limit ( $\Delta\sigma_1$ ).

As discussed in Section 1.1, fatigue life is described in this report as the number of cycles of a specified strain amplitude that a specimen can sustain before the formation of a 3-mm-deep crack (i.e., an “engineering crack”). This is assumed throughout this report to equate to crack initiation in an actual component. Using this definition, a calculated fatigue CUF less than unity provides reasonable assurance that a fatigue crack has not formed in a component, and indicates that the probability of forming a crack in the component is low.

## 2.2 Fatigue Cracking in LWR Environments

The available small-scale laboratory fatigue test data indicate a significant decrease in fatigue life of reactor structural materials in LWR environments. The extent of environmental effects depends on the applied strain, temperature, strain rate, DO in the water, and for carbon and low-alloy steels, the sulfur content in the steel. Although the structure and cyclic hardening behavior of carbon and low-alloy steels are distinctly different, there is little or no difference in susceptibility to environmental degradation of fatigue life of these steels. Reduction in fatigue life in LWR coolant environments may arise from easy formation of surface microcracks consisting of the growth of MSCs (i.e., the initiation stage) and/or an increase in growth of mechanically small cracks (i.e., propagation stage). The formation and growth characteristics of fatigue cracks are discussed in detail for carbon and low-alloy steels and wrought and cast austenitic SSs in the following sections. Similar information for Ni-Cr-Fe alloys is very limited.

### 2.2.1 Carbon and Low-Alloy Steels

Carbon and low-alloy steels tested in air show slight discoloration, while those tested in water develop a gray/black corrosion scale and are covered with magnetite ( $\text{Fe}_3\text{O}_4$ ) at all DO levels. Hematite ( $\alpha\text{-Fe}_2\text{O}_3$ ) forms on these materials at DO levels above 200 parts per billion (ppb).<sup>20,22,172</sup> The amount of hematite increases with increasing DO levels in the water.<sup>20</sup> Studies on the pitting behavior of carbon and low-alloy steels<sup>173,174</sup> in high-purity water indicate that pitting corrosion does not occur in these steels at reactor operating temperatures in low-DO PWR environments [typically less than 0.01 parts per million (ppm) DO], and at temperatures above 200°C in water that contains 0.1–0.2 ppm DO, which represents normal BWR water chemistry. However, even under these conditions, micropits form in both types of steels due to dissolution of manganese sulfide (MnS) inclusions<sup>18</sup> or by anodic reaction in the S contaminated matrix<sup>175</sup> close to sulfide inclusions. These micropits and cavities can act as stress raisers and provide preferred sites for the formation of fatigue cracks.

#### 2.2.1.1 Effects of Surface Micropits

The strain rate effects in water are such that fatigue life decreases with decreasing strain rate. These effects are often explained by a higher density of micropits at lower strain rates. Some investigators argue that the longer test durations for slow strain rate tests result in a higher density of micropits and, therefore, shorter periods for the formation of surface microcracks.<sup>18</sup> However, if the presence of micropits was responsible for the reduction in fatigue lives of carbon and low-alloy steels in LWR environments, then specimens pre-exposed to high-DO water followed by testing in air should also show a decrease in fatigue life.

Figure 9 shows a comparison of the fatigue lives of carbon and low-alloy steels tested in high-DO water at 288°C with the fatigue lives of carbon and low-alloy steels preoxidized at 288°C for 30–100 hours in water with 0.6–0.8 ppm DO and then tested in either air or low-DO water with less than 0.01 ppm DO.<sup>40,41,176</sup> The fatigue lives of the preoxidized specimens were identical to those of the unoxidized specimens; life was expected to decrease if surface micropits facilitate the formation of fatigue cracks. Only a moderate decrease in life was observed for both preoxidized and unoxidized specimens tested in low-DO water. Furthermore, if micropits were responsible for the decrease in fatigue lives in LWR environments, then the fatigue limit of these steels should be lower in water than in air.

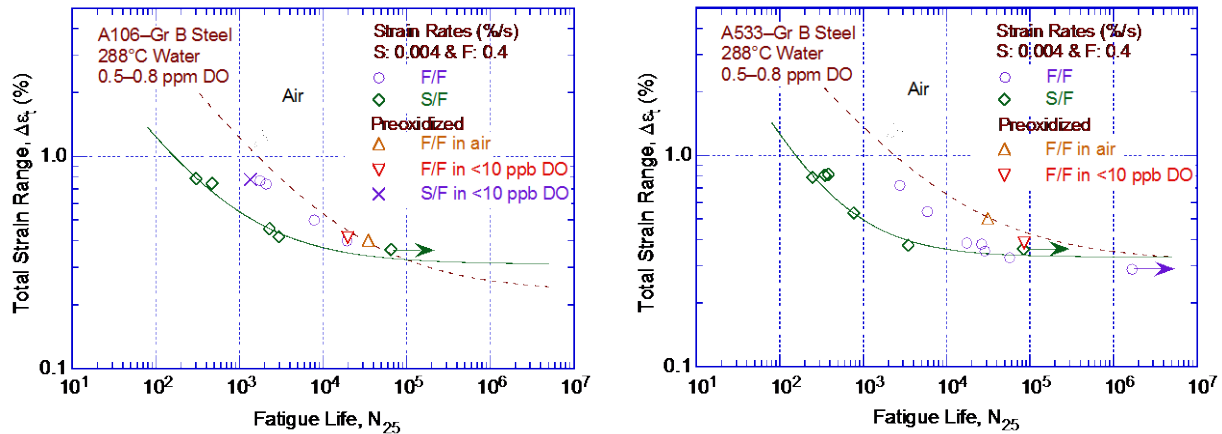


**Figure 9. Fatigue life of carbon and low-alloy steel specimens in high-DO water at 288°C compared with the fatigue life of specimens preoxidized in high-DO water and tested in either air or low-DO water at 288°C (Refs. 40,41,176).**

The extent of fatigue cracking, as measured by the number of cracks with depths greater than 10  $\mu\text{m}$ , along longitudinal sections of carbon and low-alloy steel specimens as a function of strain range in air, simulated PWR, and high-DO water was also investigated.<sup>176</sup> The results indicated that, with the exception of low-alloy steel tested in simulated PWR water, the water environment had no effect on the frequency (number per unit gauge length) of cracks. For similar loading conditions, the number of cracks in the specimens tested in air and high-DO water was identical, although fatigue lives were lower by a factor of approximately 8 in water. If the reduction in life was caused by enhanced crack nucleation, the specimens tested in high-DO water should have shown a higher number of cracks. Detailed metallographic evaluations of the fatigue test specimens<sup>176</sup> also indicated that, irrespective of environment, cracks in carbon and low-alloy steels nucleated along slip bands, carbide particles, or at the ferrite/pearlite phase boundaries.<sup>11,176</sup>

### 2.2.1.2 Mechanisms of Corrosion Fatigue

The environmental enhancement of fatigue crack growth in pressure vessel steels in high-temperature oxygenated water and the effects of sulfur content, loading rate, and flow velocities are well documented.<sup>177-189</sup> Dissolution of MnS inclusions changes the water chemistry near the crack tip, making it more aggressive. This results in enhanced crack growth rates because either (a) the dissolved sulfides decrease the repassivation rate, which increases the amount of metal dissolution for a given oxide rupture rate;<sup>189</sup> or (b) the dissolved sulfide poisons the recombination of hydrogen (H) atoms liberated by corrosion, which enhances H uptake by the steel at the crack tip.

The enhanced CGRs in LWR environments are attributed to either slip oxidation/dissolution<sup>189-193</sup> or hydrogen-induced cracking mechanisms.<sup>194-196</sup> For the slip oxidation/dissolution mechanism, a critical concentration of sulfide ( $\text{S}^{2-}$ ) or hydrosulfide ( $\text{HS}^-$ ) ions, which are produced by the dissolution of sulfide inclusions in the steel, is required at the crack tip for environmental effects to occur. The crack tip is supplied with  $\text{S}^{2-}$  and  $\text{HS}^-$  ions as the advancing crack intersects the sulfide inclusions, and the inclusions dissolve in the high-temperature water environment. Sulfide ions are removed from the crack tip by one or more of the following processes: (a) diffusion due to a concentration gradient, (b) ion transport due to an electrochemical potential (ECP) gradient, (c) pumping action due to cyclic loading on the crack, and/or (d) fluid flow induced within the crack due to the flow of coolant outside the crack. The

morphology, size, and distribution of sulfide inclusions and the probability of advancing the crack to intercept the sulfide inclusions are important parameters affecting growth rates of carbon and low-alloy steels in LWR environments.<sup>183,185-188</sup>

The requirements for a slip dissolution model are that a protective oxide film is thermodynamically stable to ensure that a crack will propagate with a high aspect ratio without degrading into a blunt pit, and that a strain increment occurs to rupture that film and thereby expose the underlying matrix to the environment, Fig. 10. Once the passive oxide film is ruptured, crack extension is controlled by dissolution of freshly exposed surfaces and by the oxidation characteristics. The effect of the environment increases with decreasing strain rate. The mechanism assumes that environmental effects do not occur during the compressive load cycle because during that period water does not have access to the crack tip. Ford, Andresen, et al.<sup>191,192</sup> proposed that the average environmentally assisted crack growth rate,  $\bar{V}_t$  (centimeters/second), is related to the crack tip strain rate,  $\dot{\epsilon}_{ct}$ , by the relationship

$$\bar{V}_t = A(\dot{\epsilon}_{ct})^n, \quad (13)$$

where the constants A and n depend on the material and environmental conditions at the crack tip. There is a lower limit of crack propagation rate associated either with blunting when the crack tip cannot keep up with the general corrosion rate of the crack sides, or with the fact that a critical level of sulfide ions cannot be maintained at the crack tip. For example, the latter condition may occur when the crack growth rate falls below a critical value such that a high concentration of sulfide ions cannot be maintained at the crack tip. The critical crack growth rate at which this transition occurs depends on the DO level, flow rate, and S content of the steel.

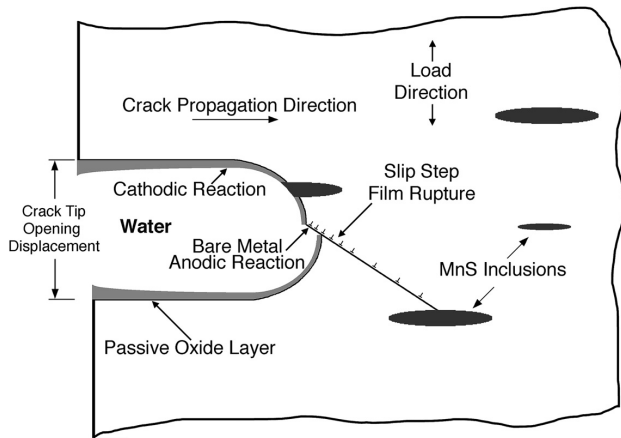


**Figure 10.** Schematic illustration of slip oxidation/dissolution process.

The average critical velocity,  $\bar{V}_{in}$  (millimeters/second), for initiation or cessation of environmentally assisted cracking (EAC), was shown to depend on the balance between sulfide supply rate and mass transport away from the crack tip.<sup>178,182</sup> Initiation of EAC requires a critical concentration of sulfide ions at the crack tip, which is supplied with sulfide ions as the advancing crack intersects the sulfide inclusions, and the inclusions dissolve in the high-temperature water. Crack growth studies in high-temperature, low-DO environment (i.e., less than 0.05 ppm DO) indicate that  $\bar{V}_{in}$  is given by

$$\bar{V}_{in} = \frac{1.27 \times 10^{-6}}{a}, \quad (14)$$

where  $a$  is the crack depth (mm). Thus, for a 2.54 mm crack depth, a minimum average crack velocity of  $5 \times 10^{-7}$  millimeters/second is required to produce the sulfide ion concentration for environmental effects on crack growth to be pronounced.<sup>182</sup> In addition, the critical velocity must be maintained for a minimum crack extension of 0.33 mm to achieve the concentration of sulfide ions needed for initiating environmental enhancement of growth rates.<sup>178</sup> Equation 14 indicates that the minimum crack velocity to initiate environmental effects increases with decreasing crack depth. For crack depths between 0.01 and 3 mm, crack velocities in the range of  $1.27 \times 10^{-4}$  to  $4.23 \times 10^{-7}$  millimeters/second are required to cause a measurable reduction in fatigue lives of carbon and low-alloy steels in low-DO water. For smooth cylindrical fatigue specimens, these growth rates are not achieved under the loading conditions typically used for fatigue  $\epsilon$ - $N$  data, which suggests that environmental effects on fatigue lives in low-DO environments are not significant. This behavior is consistent with the existing fatigue  $\epsilon$ - $N$  data; for most compositions of carbon and low-alloy steels, only moderate reductions in fatigue life (less than a factor of 2) are observed in 288°C water containing less than 0.01 ppm DO, which is within the data scatter.

In addition, consistent with the slip dissolution mechanism assumption mentioned previously, it is assumed that environmental enhancement of crack propagation does not occur during the compressive load cycle because, during that period, the water does not have access to the crack tip due to crack closure. The total crack advance during a fatigue cycle is given by the summation of crack advance in air due to mechanical factors, and crack advance during the tensile load cycle (i.e., increasing strain) from a slip-dissolution mechanism, once the tensile strain increment exceeds the fracture strain of the oxide.

Hydrogen-induced cracking (Fig. 11) of carbon and low-alloy steels is caused by hydrogen produced by the oxidation reaction at the crack tip that is partly absorbed into the metal; it interacts with MnS inclusions and leads to the formation of cleavage cracks at the inclusion matrix interface. Crack extension occurs by linkage of the cleavage cracks. Other hydrogen-induced fracture processes may also enhance growth rates in LWR environments. According to the decohesion mechanism, significant accumulation of hydrogen at or near the crack tip decreases the cohesive interatomic strength of the lattice.<sup>197</sup> Hydrogen-induced bond rupture ahead of the crack tip links up with the main crack resulting in discontinuous, but enhanced crack growth. Furthermore, adsorbed hydrogen lowers the surface energy of the metal, thus facilitating crack growth at a lower fracture stress level. In addition, hydrogen can cause localized crack tip plasticity by reducing the stress required for dislocation motion.<sup>198</sup> Note that the hydrogen produced at the crack tip by this mechanism is not related to the hydrogen content of the bulk fluid; as a result, hydrogen content of the bulk fluid is not a parameter in the  $F_{en}$  expressions.

Both the slip-oxidation/dissolution and hydrogen-induced cracking mechanisms are dependent on oxide rupture rates, passivation rates, and liquid diffusion rates. Therefore, it is difficult to differentiate between the two mechanisms or to establish their relative contribution to crack growth rates in LWR environments. However, fatigue crack morphologies in test specimens indicate that both the slip-oxidation/dissolution and hydrogen-induced cracking mechanisms are important for environmental effects of the fatigue lives of carbon and low-alloy steels in LWR environments. A change in fracture appearance from ductile striations in air to brittle facets or cleavage-like fracture in LWR environments lends the greatest support for hydrogen-induced cracking.<sup>142,143,187,195,196</sup>

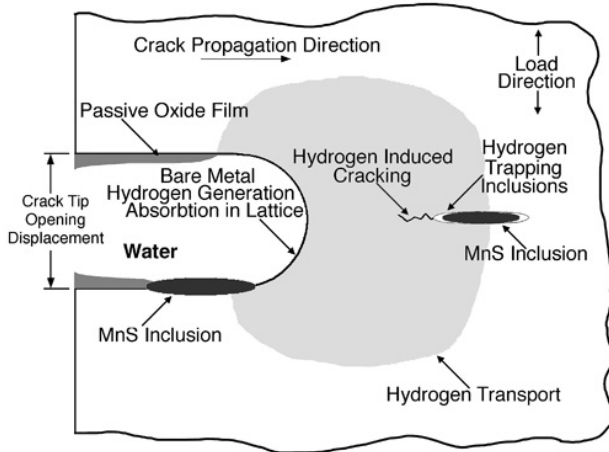


**Figure 11.**  
**Schematic illustration of**  
**hydrogen-induced cracking**  
**of low-alloy steel.**

The fatigue crack morphologies of carbon and low-alloy steels in a BWR environment also show a strong dependence and change with strain rate. At high strain rates, surface crack morphology is predominantly a zigzag pattern and inclined to the loading axis, whereas entirely straight crack morphology normal to the loading axis is observed at slow strain rates.<sup>10,139,143</sup> The surface crack morphology in A106-Gr. B carbon steel tested in air and high-DO water at 288°C is shown in Fig. 12. In addition, high strain rates lead to a rough fracture surface with the typical fan-like or quasi-cleavage cracking pattern, and slow strain rates result in a flat, nondescript fracture surface.<sup>139,142</sup> The propagation of fatigue cracks in A106-Gr. B carbon steel is shown in Fig. 13. In air, fatigue cracks grow along relatively soft ferrite regions and avoid the hard pearlite regions. In contrast, in a high-DO BWR environment, fatigue cracks appear to grow straight, normal to the stress axis, and through both the soft ferrite and the hard pearlite regions. Such crack growth characteristics are consistent with the slip-oxidation/dissolution mechanism and crack extension by anodic dissolution of the matrix in a corrosive environment.

Wu and Katada<sup>142</sup> attributed the change in crack morphology to a change in the corrosion fatigue mechanism from hydrogen-induced cracking to a slip-oxidation/dissolution mechanism with decreasing strain rate. The authors reasoned that, during cyclic loading in high temperature water, plastic deformation induces slip bands at the crack tip along the maximum shear or preferred slip directions. The extrusion of slip bands may rupture the protective oxide film at the crack tip. The slip bands are the favored path for hydrogen transportation and the interfaces between the matrix and inclusions or precipitations in the region of maximum hydrostatic tension are the preferred traps for hydrogen. Thus, hydrogen tends to accumulate at these sites and embrittle them. As a result, at high strain rates, fatigue cracking preferentially occurs along the slip bands or preferred slip directions as well as the matrix/inclusions interfaces, which results in macroscopically tortuous fatigue cracks and a rough fracture surface. However, at low strain rates, fatigue crack growth in high-temperature water is controlled by the film-rupture/oxidation-dissolution mechanism, which results in macroscopically straight fatigue cracks and a relatively flat, featureless fracture surface.

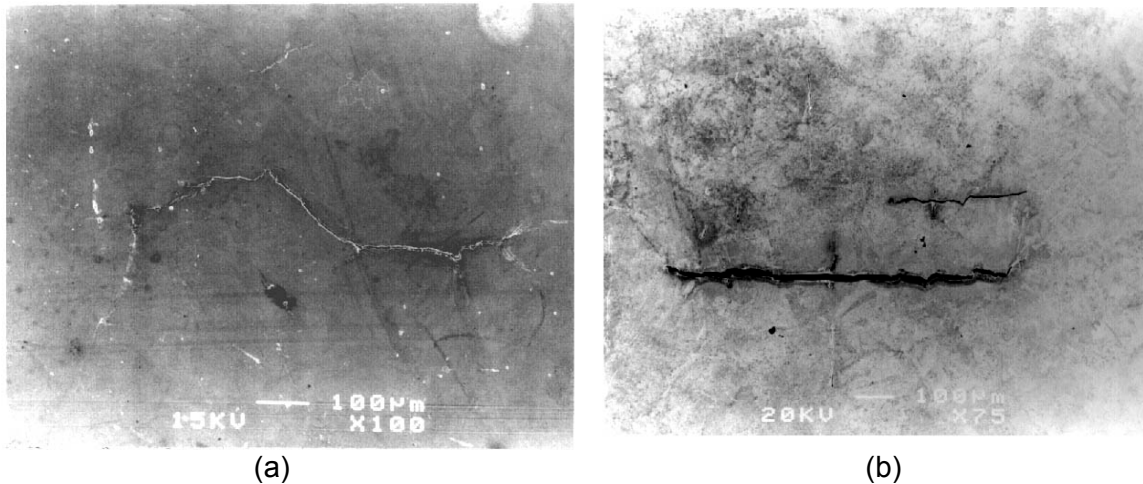


**Figure 12. Fatigue cracks on gauge surfaces of A106-Gr. B carbon steel tested in (a) air and (b) high-DO water at 288°C (Ref. 10).**

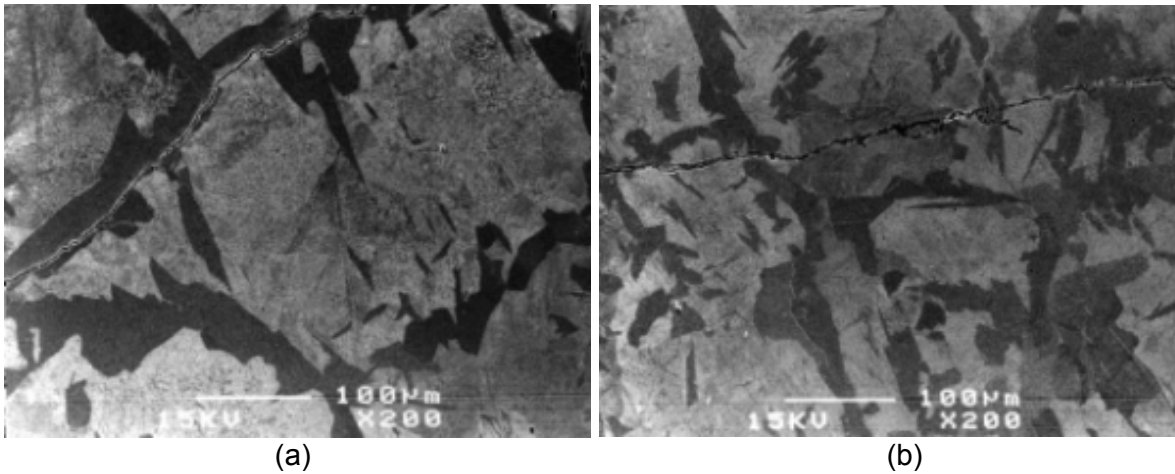


**Figure 13. Fatigue cracks along longitudinal sections of A106-Gr. B carbon steel tested in (a) air and (b) high-DO water at 288°C (Ref. 10).**

### 2.2.1.3 Effects of Dynamic Strain Aging (DSA)

Several studies showed that DSA may play a significant role in the cyclic deformation process of carbon and low-alloy steels in LWR environments.<sup>147-151</sup> DSA occurs in alloys containing solutes that segregate strongly to dislocations resulting in strong interactions between the solute and the stress-strain field of the dislocations, which leads to dislocation pinning, Fig. 14. In carbon and low-alloy steels, DSA occurs due to interstitial elements such as nitrogen and carbon. DSA is sufficiently rapid to occur during fatigue straining and produces a variety of inhomogeneous deformations such as serrated yielding, jerky or serrated flow, etc. These effects depend on temperature and strain rate.

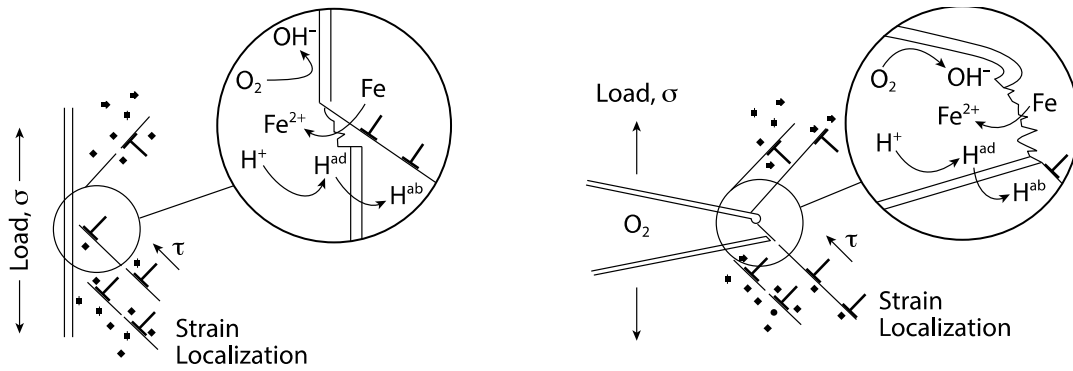


**Figure 14. (a) Fatigue crack initiation and (b) crack growth in DSA susceptible low-alloy steel exposed to high-temperature water environment (Ref. 147).**

Under certain combinations of temperature and strain rate conditions, DSA may significantly affect the EAC behavior of carbon and low-alloy steels by increasing the yield and tensile strength, the strain hardening exponent, the creep rate, and the crack-tip strain and strain rate.<sup>149</sup> DSA also results in planar deformation, an increase in dislocation density and inhomogeneous localization of deformation. These factors favor brittle crack extension and rupture of the protective oxide film, thereby enhancing crack advance by either anodic dissolution or hydrogen embrittlement processes. In high-temperature water, the synergistic interactions between EAC and DSA during fatigue straining may be rationalized as follows:<sup>149</sup>

- Hydrogen vacancies produced by the corrosion reaction at the crack tip enter the steel and hydrogen diffuses to strong trapping sites inside the crack-tip maximum hydrostatic stress region (e.g., MnS inclusions) ahead of the crack tip.
- These sites act as initiation sites for local quasi-cleavage cracking, as well as void formation, and these microcracks link with the main crack.
- In addition, at a given macroscopic strain due to external loads, the microscopic strain in steels that are susceptible to DSA is higher because of strain localization to small areas, which leads to higher rates and larger steps of oxide film rupture. As a result, the slip oxidation/dissolution process enhances fatigue crack initiation or fatigue crack growth rates.
- Such interactions, however, occur only under certain conditions of temperature, strain rate, and DO level in the environment.

In carbon and low-alloys steels, the interaction of nitrogen and dislocations during plastic deformation reduces plasticity, which causes strain localization in the material.<sup>147</sup> Small areas can deform plastically adjacent to areas that might be blocked by nitrogen/dislocation interactions. For a given macroscopic strain, the microscopic strain is higher due to strain localization in steels that are susceptible to DSA. Thus, because of strain localization, stress concentrations at active slip planes lead to higher rates and larger steps of oxide rupture and, simultaneously, to a decreased repassivation rate.<sup>147,148</sup> Consequently, both crack initiation and growth rates may be enhanced in carbon and low-alloy steels.

### 2.2.1.4 Crack Growth Rates in Smooth Fatigue Specimens

Studies on the formation and growth characteristics of short cracks in smooth fatigue specimens in LWR environments indicated that the decrease in fatigue life in LWR environments is caused primarily by the effects of the environment on the growth of MSCs (i.e., cracks less than 200  $\mu\text{m}$  deep) and, to a lesser extent, on the growth of mechanically small cracks.<sup>10,11</sup> Measured crack lengths as a function of fatigue cycles and fraction of fatigue life for smooth cylindrical specimens of A533-Gr B low-alloy steel in air, simulated PWR environment, and high-DO water are shown in Fig. 15. An example of the growth of a surface crack in A533-Gr. B steel tested in air at room temperature, and the fracture surface and probable crack front for the crack, are shown in Fig. 16. The results indicate that, for this example, three cracks merged to form the final fracture surface. The primary crack initiated near an inclusion and reached a surface length of approximately 100  $\mu\text{m}$  after 3,062 cycles (i.e., approximately 50% of the fatigue life). Two secondary cracks merged with the primary crack after approximately 5,700 and 6,000 cycles. Crack depth was determined by dividing the surface crack length by pi ( $\pi$ ).

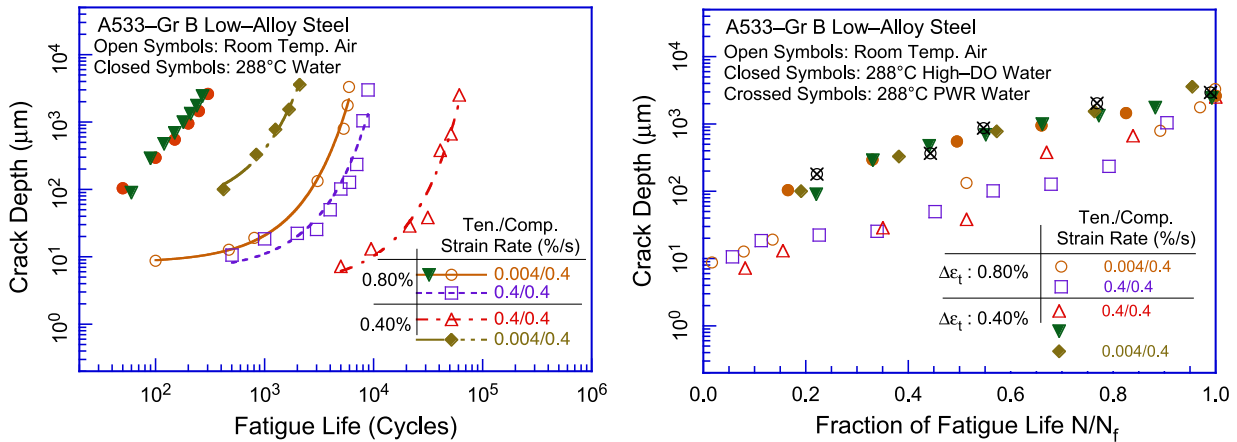


**Figure 15.** Depth of largest crack plotted as a function of (a) fatigue cycles and (b) fraction of fatigue life for A533-Gr B low-alloy steel in air and water environments (Ref. 11).

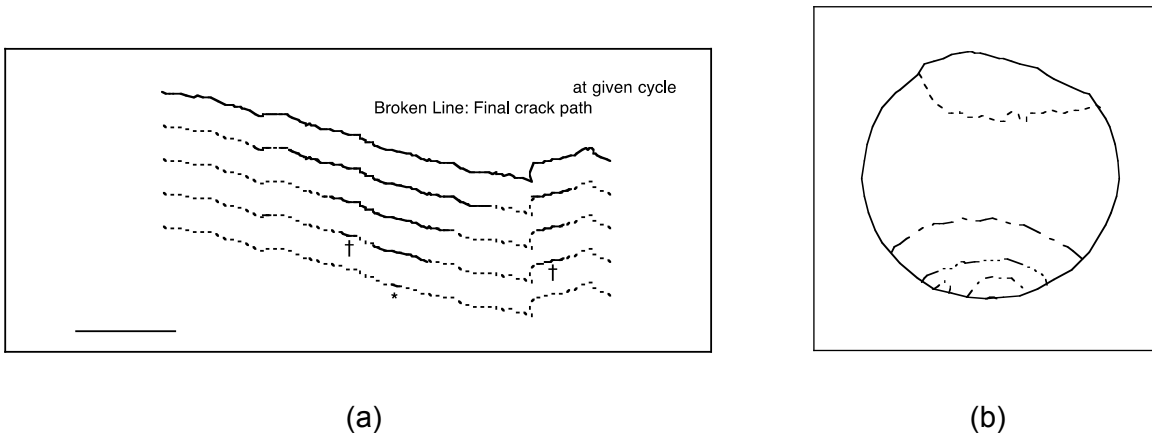


**Figure 16.** (a) Morphology and length of surface crack after various numbers of cycles for A533-Gr. B steel in air at room temperature, and (b) fracture surface and probable crack front for surface cracks shown in (a) (Ref. 11).

The crack growth rates corresponding to the data shown in Fig. 15 are plotted as a function of crack depth in Fig. 17. The results indicate that, in LWR environments, the period spent in the growth of MSCs is decreased. At approximately 0.8% strain range, only 30-50 cycles are needed to form a 100- $\mu\text{m}$  crack in high-DO water, whereas approximately 450 cycles are required to form a 100- $\mu\text{m}$  crack in a low-DO PWR environment and more than 3,000 cycles in air. These values correspond to average growth rates of approximately 2.5, 0.22, and 0.033  $\mu\text{m}/\text{cycle}$  in high-DO water, low-DO PWR environment, and air, respectively. The results also indicate that, relative to air, CGRs in high-DO water are nearly two orders of magnitude higher during the initial stages of fatigue life (i.e., for crack sizes less than 100  $\mu\text{m}$ ), and are one order of magnitude higher for crack sizes greater than 100  $\mu\text{m}$ .

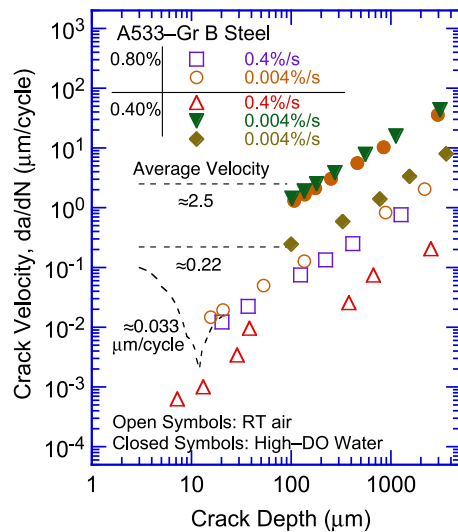
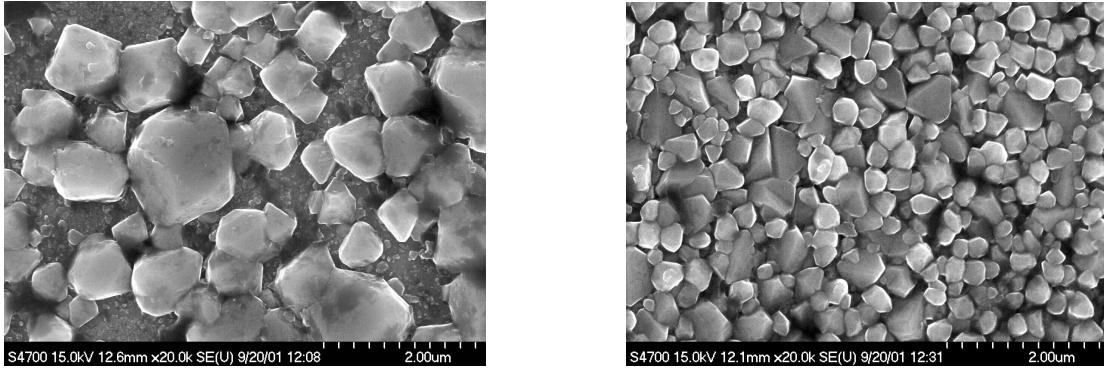


**Figure 17.**  
Crack growth rates plotted as a function of crack depth for A533-Gr B low-alloy steel tested in air and water environments (Ref. 11).

The surface crack and fracture surface morphologies of the test specimens indicate that, in high-temperature, high-DO water with slow strain rates, the surface cracks appear to grow entirely in Stage II growth as Mode I tensile cracks normal to the stress axis (Figs. 12 and 13). In air and low-DO PWR environments, both Stage I and Stage II growths are observed. Surface cracks grow initially as Mode II (shear) cracks along planes 45° to the stress axis and, when the stress intensities are large enough to promote slip on axes other than the primary slip axis, they grow as Mode I (tensile) cracks normal to the stress axis. Also, for A106-Gr. B carbon steel, Stage I crack growth in air and low-DO water occurs entirely along the soft ferrite grains, whereas in high-DO water, cracks propagate across both ferrite and pearlite regions. These results are consistent with the slip-oxidation/dissolution mechanism in high-DO water.

## 2.2.2 Austenitic Stainless Steels

Austenitic SSs exposed to LWR environments develop an oxide film that consists of two layers: a fine-grained, tightly-adherent, chromium-rich inner layer, and a crystalline, nickel-rich outer layer composed of large and intermediate-sized particles. Photomicrographs of the gauge surface of Type 316NG specimens tested in simulated PWR water and high-DO water are shown in Fig. 18. The inner layer forms by solid-state growth, whereas the crystalline outer layer forms by precipitation or deposition from the solution. A schematic representation of the surface oxide film is shown in Fig. 19.



(a) (b)  
**Figure 18. Photomicrographs of oxide films that formed on Type 316NG stainless steel in (a) simulated PWR water and (b) high-DO water (Ref. 13).**

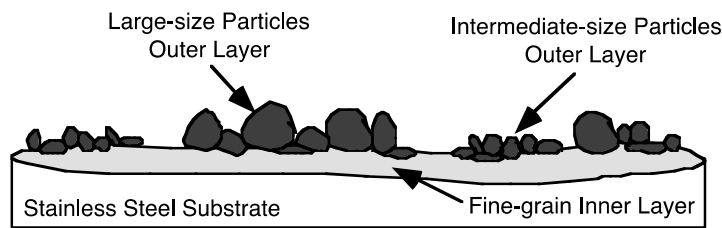


**Figure 19. Schematic of the corrosion oxide film formed on austenitic stainless steels in LWR environments.**

Several studies characterized the oxide films that form on austenitic SSs in LWR environments.<sup>199-205</sup> The inner layer consists of chromium-rich spinel ( $\text{Ni}_x\text{Cr}_y\text{Fe}_{3-x-y}\text{O}_4$ ) with a nonstoichiometric composition; the actual composition of spinels varies with environmental conditions. Da Cunha Belo, et al.<sup>203</sup> determined that the inner layer that formed on Type 316L SS in a PWR environment at 350°C consisted of mixed chromium oxides ( $\text{Cr}_2\text{O}_3 + \text{FeCr}_2\text{O}_4$ ) and  $\text{Fe}_3\text{O}_4$ . Nakayama and Oshida<sup>205</sup> characterized the oxide film on SSs exposed to high-DO (8 ppm) water at 300°C as chiefly composed of  $\text{NiO} \cdot (\text{Cr,Fe})_2\text{O}_3$  and/or  $\text{NiFe}_2\text{O}_4$ , which may be formed by a solid reaction between  $\text{NiO}$  and  $(\text{Cr,Fe})_2\text{O}_3$  or  $\alpha\text{-Fe}_2\text{O}_3$ . Kim<sup>199,200</sup> identified the  $\text{FeCr}_2\text{O}_4$  spinel chromite (or  $\text{Fe}_x\text{Cr}_{3-x}\text{O}_4$ ), along with  $\text{NiFe}_2\text{O}_4$ , in the inner layer formed on Types 304 and 316 SSs exposed at 288°C under BWR normal water chemistry (NWC) or BWR hydrogen water chemistry (HWC) conditions. Kim also noted that the inner oxide layer formed in a NWC BWR environment contained a lower concentration of chromium than that formed in a HWC low-DO environment. Such differences were attributed to chromium oxidation in high-DO water.

The structure and composition of the crystalline outer layer vary with the water chemistry. In BWR environments, the large particles in the outer layer are primarily composed of  $\gamma\text{-Fe}_2\text{O}_3$  hematite in NWC, and  $\text{Fe}_3\text{O}_4$  magnetite in HWC.<sup>199,200</sup> The intermediate particles in the outer layer are composed of  $\alpha\text{-Fe}_2\text{O}_3$  in NWC and  $\text{Fe}_3\text{O}_4$  in HWC. The structure of the outer layer varies when the water chemistry is cycled between NWC and HWC. In PWR environments, the large particles were identified as  $\text{Ni}_{0.75}\text{Fe}_{2.25}\text{O}_4$  spinel and the intermediate particles as  $\text{Ni}_{0.75}\text{Fe}_{2.25}\text{O}_4 + \text{Fe}_3\text{O}_4$ .<sup>203</sup> The possible effects of minor differences in the surface oxide film on fatigue crack initiation are discussed in the next section.

### 2.2.2.1 Effects of Surface Micropits

The characteristics of the surface oxide films that form on austenitic SSs in LWR coolant environments influence the mechanism and kinetics of corrosion processes and thereby influence the initiation stage, i.e., the growth of MSCs. As discussed earlier, the reduction of fatigue lives in high-temperature water may be due to the presence of surface micropits. To investigate the effect of surface micropits, fatigue tests were conducted on Type 316NG (Heat P91576) specimens that were pre-exposed to either low-DO or high-DO water and then tested in air or water environments.<sup>13</sup> The results of these tests, as well as data obtained earlier on this heat and Heat D432804 of Type 316NG SS in air and low-DO water at 288°C, are plotted in Fig. 20. The fatigue lives of specimens preoxidized in high-DO water and then tested in low-DO water were identical to those of specimens tested without preoxidation. Also, fatigue lives of specimens preoxidized at 288°C in low-DO water and then tested in air were identical to those of unoxidized specimens (Fig. 20). If micropits were responsible for the reduction in life, the pre-exposed specimens should have shown a decrease in life. Furthermore, the fatigue limit of these steels should have also been lower in water than in air, but the data indicated this limit was the same in both water and air environments. These results indicate that surface micropits or minor differences in the composition or structure of the surface oxide film had little or no effect on the formation of fatigue cracks.

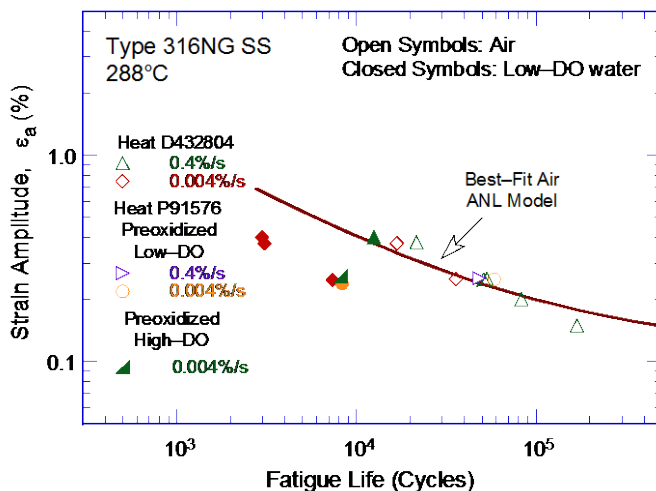


**Figure 20.** Effects of environment on formation of fatigue cracks in Type 316NG SS in air and low-DO water at 288°C. Preoxidized specimens were exposed for 10 days at 288°C in water that contained either less than 5 ppb DO and approximately 23 cm<sup>3</sup>/kg dissolved H<sub>2</sub> or approximately 500 ppb DO and no dissolved H<sub>2</sub> (Ref. 13).

### 2.2.2.2 Mechanisms of Corrosion Fatigue

Both the slip oxidation/dissolution and the hydrogen-induced cracking mechanisms depend on the rates of oxide rupture, passivation, and liquid diffusion. Therefore, it is difficult to differentiate between the two processes or to establish their relative contribution to fatigue cracking in LWR environments. However, for austenitic SSs, lower fatigue lives in low-DO water versus high-DO water are difficult to reconcile in terms of the slip oxidation/dissolution mechanism, which assumes that crack growth rates increase with increasing DO in the water. Metallographic examination of fatigue test specimens suggested that hydrogen-induced cracking may have played an important role in environmentally assisted reduction in fatigue lives of austenitic SSs.<sup>47</sup> For example, hydrogen can cause localized crack tip plasticity by reducing the stress required for dislocation motion, which leads to higher rates and larger steps of oxide film rupture. Thus, fatigue lives may be decreased, not because of increased growth rates, but because of increased film rupture frequency.

A detailed metallographic evaluation of austenitic SS fatigue test specimens was performed to characterize the crack and fracture morphology of the various heats under various heat treatment conditions.<sup>47</sup> Photomicrographs of the crack morphology of Type 304 SS specimens under all test and environmental conditions are presented in Fig. 21. In all cases, the tensile axis was vertical (parallel to the plane of each photomicrograph). For austenitic SSs, the fatigue crack surface morphology was similar to that observed for carbon and low-alloy steels. In an air environment, fatigue cracks were more likely to be oblique, approaching 45° with respect to the tensile axis. By contrast, the cracks that formed in either BWR or PWR environments tended to be perpendicular to the tensile axis.

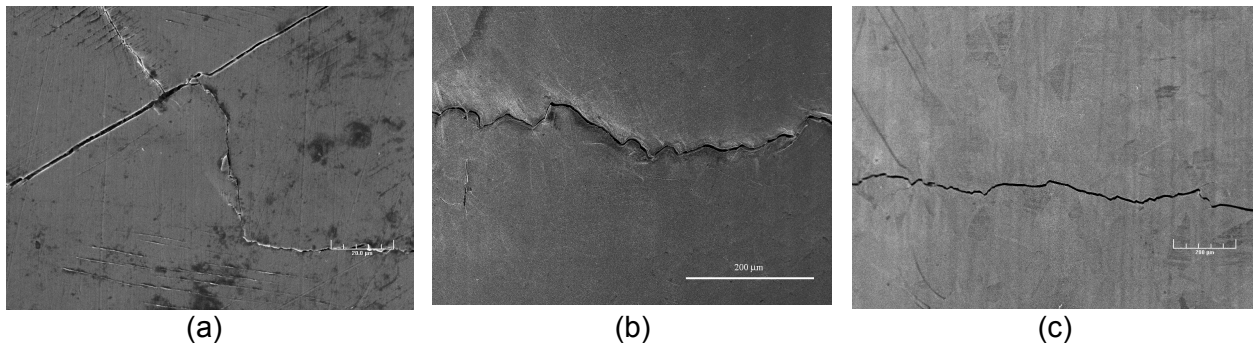
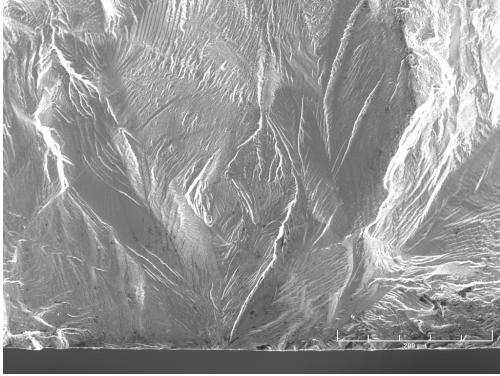


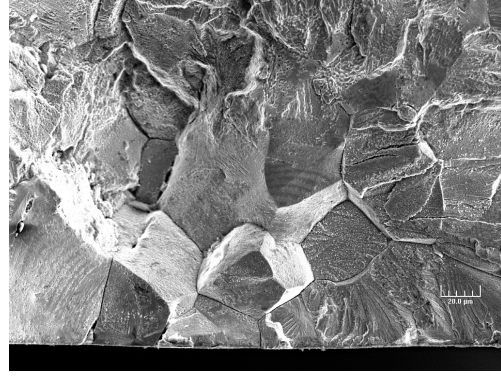
**Figure 21. Photomicrographs of the fatigue crack morphology of Type 304 SS in (a) air, (b) high-DO BWR water, and (c) low-DO PWR water at 289°C (Ref. 47).**

Photomicrographs of the crack morphology of Type 304 SS under all test and environmental conditions are presented in Fig. 22. In air, the fracture mode for crack initiation (i.e., crack depths up to 200  $\mu\text{m}$ ) and crack propagation (i.e., crack depths greater than 200  $\mu\text{m}$ ) was transgranular (TG), most likely along crystallographic planes, leaving behind relatively smooth surfaces. With an increasing degree of sensitization, cleavage-like, or stepped, TG fracture and ridge structures were observed on the smooth surfaces. In simulated NWC BWR environments, the initial crack appeared intergranular (IG) under all heat treatment conditions, implying a weakening of the grain boundaries. The extent of IG fracture increased with the degree of sensitization. Nevertheless, for crack depths beyond 200  $\mu\text{m}$ , the initial IG mode transformed into a TG mode with cleavage-like features. In simulated PWR environments, however, fatigue cracks initiated and propagated in a TG mode irrespective of the degree of sensitization. Prominent features of the fracture surfaces included highly angular, cleavage-like fracture facets that exhibited well-defined “river” patterns.<sup>47</sup> Intergranular facets were rarely observed, but when they were found, it was mostly in the more heavily sensitized alloys.

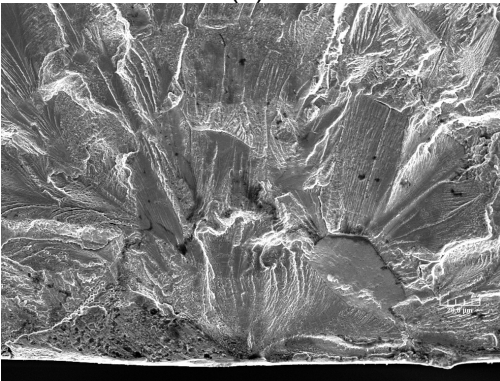
In addition, fatigue striations normal to the crack advance direction were clearly visible beyond approximately 200- $\mu\text{m}$ -crack depths on the fracture surfaces of all materials under all environmental conditions. An example of the fatigue striations observed in Type 304 SS in different environments is shown in Fig. 23. Striations were found on both the TG and IG facets of the samples tested under BWR NWC conditions, or co-existing with the “river” patterns specific to the samples tested in the PWR environments. However, the striations on specimens tested in PWR water were quite faint compared to those tested in NWC BWR water. Furthermore, examination of the specimens after chemical cleaning suggested that some striations were produced by rupture of the surface oxide film rather than the formation of double notches or “ears” at the crack tip.



(a)

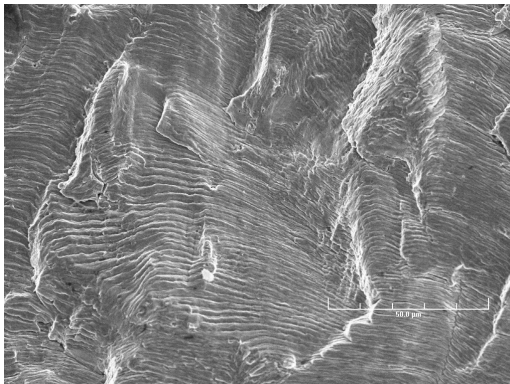


(b)

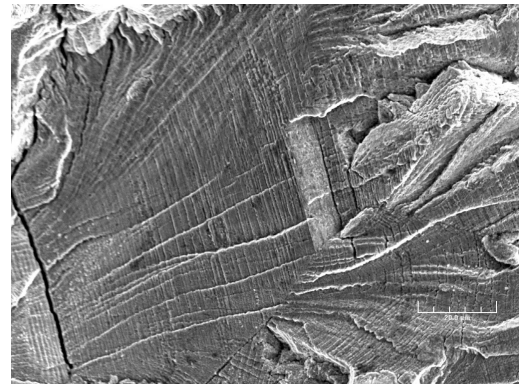


(c)

**Figure 22.** Photomicrographs showing sites of fatigue crack initiation on fracture surfaces of Type 304 SS tested at 289°C in (a) air, (b) high-DO BWR water, and (c) low-DO PWR water (Ref. 47).

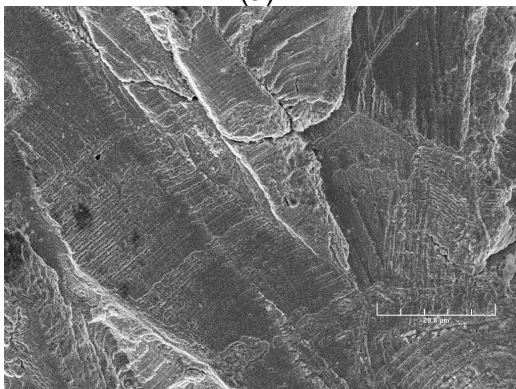


(a)



(b)

**Figure 23.** Photomicrographs showing fatigue striations on fracture surfaces of Type 304 SS tested at 289°C in (a) air, (b) high-DO BWR water, and (c) low-DO PWR water (Ref. 47).



(c)

The characterization of surface cracks and fracture morphology in austenitic SSs suggests that, in LWR environments, although film rupture was apparent, the formation and growth of fatigue cracks were primarily caused by hydrogen-induced cracking.

#### 2.2.2.3 Effects of Dynamic Strain Aging (DSA)

DSA was observed in austenitic SSs in air at strain rates below 0.3 %/s and temperatures in the range of 300-600°C; the peak effects occurred at 500-600°C.<sup>206</sup> The fatigue life of a heat of Type 316LN SS at low strain rates was greater at 600°C than at 500°C. Typically at temperatures above 400°C, the fatigue life of austenitic SSs decreased with an increase in temperature or a decrease in strain rate.<sup>57</sup> DSA increased the dislocation density at slow strain rates, which enhanced the degree of inhomogeneity of deformation during fatigue loading.

DSA was also observed in Type 304L SS under LWR operating conditions. At 0.4 %/s strain rate, the fatigue life and fatigue limit in air were higher at 300°C than at 150°C (due to secondary strain hardening at 300°C).<sup>58</sup> A similar behavior was observed for this heat of SS in PWR water. At 0.4 %/s, fatigue life decreased in PWR water relative to that in air at 150°C, but not at 300°C. This difference was identified as secondary hardening at 300°C, which was not observed at 150°C. The secondary hardening at 300°C may be due to DSA, although the temperature was relatively low.

#### 2.2.2.4 Crack Growth Rates in Smooth Fatigue Specimens

Studies on the formation and growth characteristics of short cracks in smooth fatigue specimens of austenitic SSs in LWR environments indicated that, although the growth rates of mechanically small cracks were greater in water than in air, the decrease in fatigue lives was caused predominantly by the effects of the environment on the growth of MSCs.<sup>44</sup> The growth of the largest crack in austenitic SSs with respect to fatigue cycles, in air and water environments, is shown in Fig. 24. In the figure, the crack length for the test in air at 288°C and 0.75% strain range was measured only near the end of the test. The data obtained by Orbtlik, et al.<sup>207</sup> for Type 316L SS in air at 25°C and approximately 0.2% strain range were used to estimate the crack growth in air at 0.75% strain range. Similar studies on carbon and low-alloy steels indicate<sup>11,165-167</sup> that the fatigue crack size at various life fractions was independent of strain range, strain rate, and temperature; consequently, the depth of the largest crack at various life fractions was approximately the same at strain ranges of 0.75% and 0.2%. The curve for the test in air at 0.75% (shown as a dashed line in Fig. 24) was calculated from the best-fit equation of the experimental data for Type 316L SS at 0.2% strain range; the estimated crack lengths at 0.75% strain range show very good agreement with the measured values. The results showed that, at the same number of cycles, the crack length was longer in low-DO (PWR) water than in air, e.g., after 1,500 cycles, the crack length in air, high-DO (BWR) water, and PWR water was approximately 40, 300, and 1,100  $\mu\text{m}$ , respectively. The growth of cracks during the initiation stage, i.e., growth of MSCs, was enhanced in water; the fatigue cycles needed to form a 500- $\mu\text{m}$  crack were a factor of approximately 12 lower in low-DO water than in air. Figure 24 shows that the number of cycles required to produce a 500- $\mu\text{m}$  crack is 800, 3,000, and 9,000 in low-DO (PWR) water, high-DO (BWR) water, and air environments, respectively; thus, the number of cycles was more than a factor of 10 lower in low-DO water than in air.

The CGRs during the propagation stage, i.e., growth of mechanically small cracks, in air and water environments are plotted as a function of crack length in Fig. 25; they were calculated from the best fit of the data in Fig. 24. The CGRs in high-DO water for the specimen with a 24-hour soak period (closed diamonds in Fig. 25) were determined from measurements of fatigue striations. The CGRs were a factor of 2-6 higher in water than in air. Growth rates in

PWR water or high-DO water with a 24-hour soak period were higher than those in high-DO water with a 120-hour soak period. At a crack length of approximately 1,000  $\mu\text{m}$ , the CGRs in air, high-DO water, and low-DO water were 0.30, 0.64, and 1.05  $\mu\text{m}/\text{cycle}$ , respectively. For the 0.75% strain range and 0.004%/s strain rate, these values corresponded to growth rates of approximately  $1.6 \times 10^{-9}$ ,  $3.4 \times 10^{-9}$ , and  $5.6 \times 10^{-9}$  meters/second in air, high-DO water, and low-DO water, respectively. Thus, growth rates were a factor of 3.5 greater in low-DO water than in air.

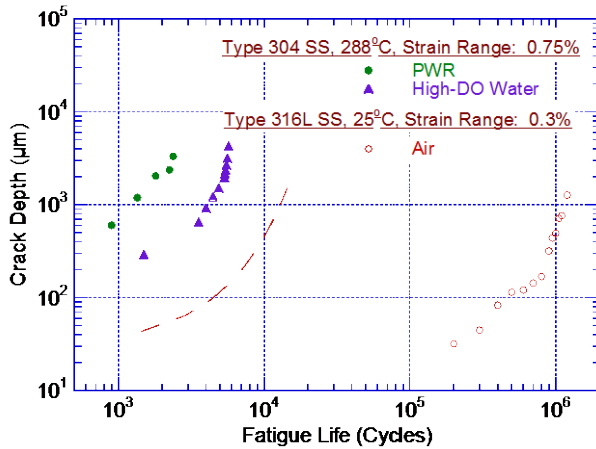


**Figure 24.** Depth of largest crack plotted as a function of fatigue cycles for austenitic stainless steels in air and water (Refs. 13,207).

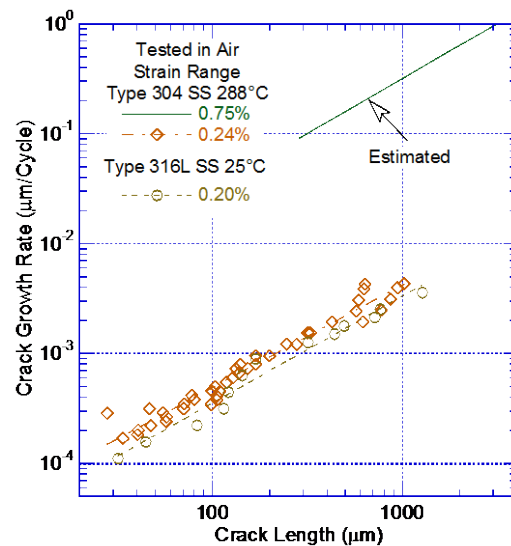
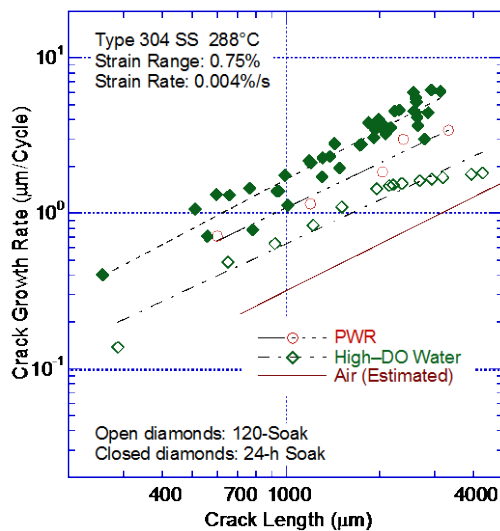


**Figure 25.** Crack growth rates plotted as a function of crack length for austenitic stainless steels in (a) water and (b) air environments (Refs. 13,44,207).

The existing fatigue crack growth ( $da/dN$ ) data obtained from fracture-mechanics tests on CT specimens of wrought and cast SSs in LWR environments were compiled by Shack and Kassner.<sup>208</sup> The results indicated significant enhancement of CGRs in high-DO water; at CGRs of less than  $10^{-10}$  meters/second in air, the rates in BWR NWC conditions exceeded the air curve in Section III of the ASME Code by a factor of approximately 20–30. The experimental CGRs for sensitized Type 304 SS in high-DO water and those predicted in air for the same mechanical loading conditions are plotted in Fig. 26a. The fatigue CGRs in air,  $\dot{a}_{\text{air}}$  (meters/second), were determined from a correlation at 288°C given by

$$\dot{a}_{\text{air}} = 3.43 \times 10^{-12} S(R) \Delta K^{3.3}/T_R, \quad (15)$$

where the function  $S(R)$  is expressed as

$$\begin{aligned} S(R) &= 1.0 & R &\leq 0 \\ S(R) &= 1.0 + 1.8R & 0 < R &\leq 0.79 \\ S(R) &= -43.35 + 57.97R, & 0.79 < R &< 1.0, \end{aligned} \quad (16)$$

and  $T_R$  is the rise time (seconds) of the loading waveform,  $R$  is the load ratio ( $K_{\min}/K_{\max}$ ), and  $\Delta K$  is  $K_{\max} - K_{\min}$ . The fatigue CGR in water [ $\dot{a}_{\text{env}}$  (meters/second)] with 0.2 ppm DO (i.e., BWR NWC) is expressed in terms of the fatigue CGR in air ( $\dot{a}_{\text{air}}$ ) by the relationship

$$\dot{a}_{\text{env}} = \dot{a}_{\text{air}} + 4.5 \times 10^{-5} (\dot{a}_{\text{air}})^{0.5}. \quad (17)$$

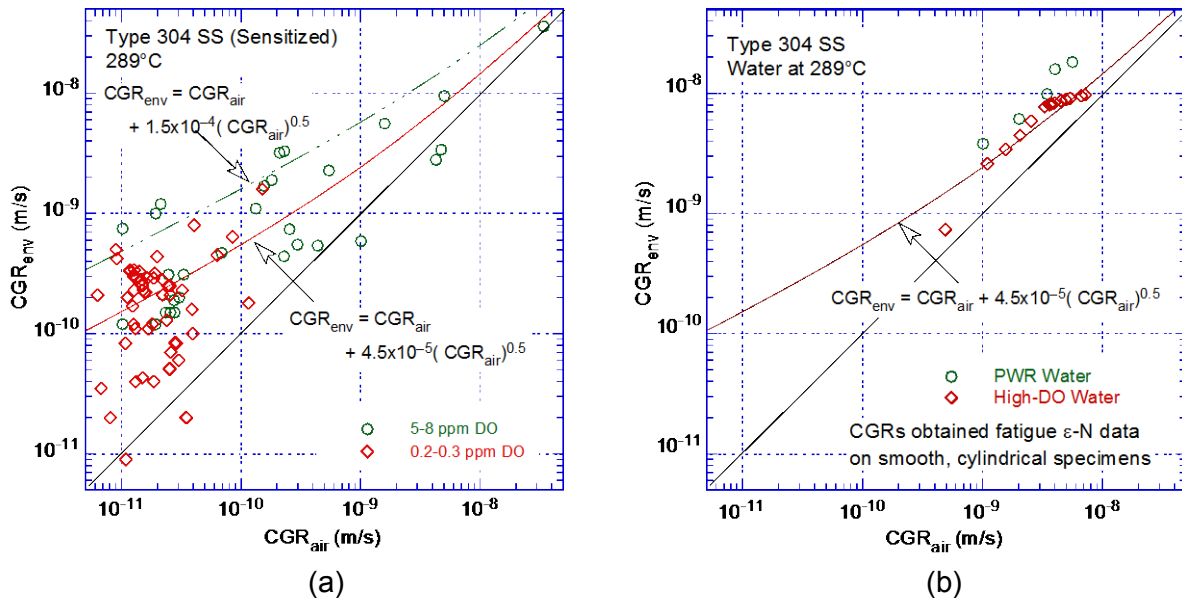


**Figure 26. Crack growth rate data for Type 304 SS in high temperature water determined from (a) fracture mechanics CT specimens and (b) smooth cylindrical fatigue specimens (Ref. 208).**

The CGR data from fracture–mechanics tests in low–DO PWR environments are sparse, particularly at rates that are less than  $10^{-9}$  meters/second. At high CGRs, the observed enhancement in both low– and high–DO environments was relatively small, and the magnitude of the enhancement under the same loading conditions was comparable in the two environments. Until further data become available at low CGRs in simulated PWR water, Shack and Kassner<sup>208</sup> recommended that the environmental enhancement represented by Eq. 17 for 0.2 ppm DO water should also be considered for PWR environments.

The CGRs determined from fatigue  $\epsilon$ – $N$  tests on smooth, cylindrical specimens in high–DO and low–DO (PWR) water environments at 289°C, are plotted in Fig. 26b. The rates in high–DO and low–DO (PWR) water represent the measured values shown as open diamonds and circles, respectively, from Fig. 25a. The CGRs in air for the same loading conditions (i.e., the same crack length) were determined from the estimated rates in air, shown by the solid line in Fig. 25 a. The results from fatigue  $\epsilon$ – $N$  tests showed good agreement with the data obtained from the

fracture–mechanics tests. The CGRs in high–DO water were consistent with the trend predicted from Eq. 17. The rates in low–DO water were slightly higher.

The large reductions in fatigue life of austenitic SSs in PWR environments cannot be explained entirely on the basis of enhanced CGRs during the propagation stage, i.e., growth of mechanically small cracks. For example, the CGRs in low–DO water are a factor of 1.6 greater than those in high–DO water, but fatigue lives are approximately a factor of 4 lower in low–DO water than in high–DO water. As indicated by the results shown in Fig. 25a, the decrease in fatigue lives of austenitic SSs in PWR environments was caused predominantly by the effects of environment on the growth of MSCs.

It should also be noted that, if enhanced CGRs alone were responsible for the environmentally assisted decrease in fatigue lives of materials in LWR environments, environmental effects on the fatigue lives of Alloy 600 and austenitic SSs in LWR environments should be comparable. In air, the fatigue  $\epsilon$ – $N$  behavior of Alloy 600 is comparable to that of austenitic SSs.<sup>61</sup> Fatigue CGR data indicate that the enhancement of CGRs of Alloy 600 and austenitic SSs in LWR environments is also comparable.<sup>209</sup> However, the fatigue  $\epsilon$ – $N$  behaviors of Alloy 600 and austenitic SSs in water differ significantly; only moderate effects of environment are observed for Alloy 600 base material and welds both in low–DO and high–DO water. For example, the fatigue life of Alloy 600 weld metal in water with less than 0.005 ppm DO at 325°C and 0.6% strain amplitude decreased by a factor of approximately 2.5 when the strain rate was decreased from 0.4 to 0.001 %/s. Under similar environmental and loading conditions, the fatigue lives of austenitic SSs were decreased by a factor of approximately ten.



### 3. FATIGUE STRAIN VS. LIFE ( $\epsilon$ -N) BEHAVIOR IN AIR

---

During 1990s, the existing fatigue  $\epsilon$ -N data developed at various establishments and research laboratories worldwide were compiled by the PVRC Working Group on  $\epsilon$ -N Curve and Data Analysis. The database used in the ANL studies, and presented in the initial revision to NUREG/CR-6909, was an extended version of the PVRC database. The reanalysis of the fatigue  $\epsilon$ -N data presented in this report is based on a much larger fatigue  $\epsilon$ -N database. The additional data include the JNES data summarized in JNES-SS-1005 on carbon and low-alloy steels, wrought and cast austenitic SSs, Ni-Cr-Fe alloys, and their associated weld metals tested in air and LWR environments,<sup>136</sup> and fatigue  $\epsilon$ -N test results from the open literature on several heats of carbon and low-alloy steels tested in BWR environments.<sup>138-146</sup> Nearly 60% of the data in the more recent JNES database were included the old JNUFAD<sup>210</sup> database. The JNUFAD database formed a portion of the PVRC database, which was used in the original revision to NUREG/CR-6909 report.

Unless otherwise mentioned, the fatigue database was obtained from smooth cylindrical gauge specimens that were tested under strain control with fully reversed loading, i.e., strain ratio, R, of  $-1$ . Tests on notched specimens or at R values other than  $-1$  were excluded from the fatigue  $\epsilon$ -N data analysis performed for this report. For the previous fatigue testing performed at ANL, the estimated uncertainty in the strain measurements was about 4% of the reported values. For the data obtained in other laboratories, the uncertainty in the reported values of strain is unknown, but was assumed to be small enough such that the results were not significantly impacted.

In nearly all tests, fatigue life was defined as the number of cycles necessary for the tensile stress to drop 25% from its peak or steady-state value,  $N_{25}$ . As discussed in Section 1.1, for the specimen sizes used in these studies, e.g., 5.1–9.5 mm (0.2–0.375 in.) diameter cylindrical specimens, failure corresponds to an approximately 3-mm-deep crack. Some of the earlier tests in air were carried out to complete failure of the specimens, and in some other tests, fatigue lives were defined as the number of cycles for peak tensile stresses to decrease by 10 or 50%. Fatigue lives defined by a criterion other than a 25% load drop were therefore converted to consistent  $N_{25}$  values according to the following formula:

$$N_{25} = N_X / (0.947 + 0.00212X), \quad (18)$$

where X is the failure criterion (e.g., 10, 50 or 100% decrease in peak tensile stress).<sup>10</sup> The estimated uncertainty in fatigue life determined by this procedure is about 2%, which is within the strain measurement uncertainty.

The 25% load drop criterion was not used for the tests that were performed using tube specimens. For tube specimens, fatigue lives were represented by the number of cycles to develop a leak because, with the exception of a few specimens, all tube specimens had 3-mm wall thicknesses.

#### 3.1 Carbon and Low-Alloy Steels and Weld Metals

##### 3.1.1 Experimental Data

The primary sources of fatigue  $\epsilon$ -N data for carbon and low-alloy steels are the tests performed by General Electric Co. (GE) in a test loop at the Dresden 1 reactor;<sup>14,15</sup> work sponsored by EPRI at GE;<sup>16,17</sup> the work of Terrell at Materials Engineering Associates (MEA);<sup>48-50</sup> the work at

ANL on fatigue of pressure vessel and piping steels;<sup>10–13,40–47</sup> the large JNES database<sup>136</sup> “Environmental Fatigue Evaluation Method for Nuclear Power Plants,” studies at Ishikawajima-Harima Heavy Industries (IHI), Hitachi, and Mitsubishi Heavy Industries (MHI) in Japan;<sup>18–36</sup> and the studies at Kraftwerk Union Laboratories (KWU) and Materialprüfungsanstalt (MPA) in Germany.<sup>55,56</sup> From these sources, the total database for fatigue tests in air is composed of 684 tests; 254 tests on carbon steels and 430 tests on low-alloy steels. Carbon steels include 19 heats of A106–Grades B and C, A333–Grade 6, A508–Grade 1, and A333–Grade 6 weld metals. Low-alloy steels include 22 heats of A302–Grade B, A508–Grade 2 and 3, and A533–Grade B steel. A summary of the sources included in the updated database used for the present analyses, as categorized by material type and test environment, is presented in Table 1. Other material information such as chemical composition, heat treatment, and room temperature tensile properties of the various types and heats of materials is given in Appendix B.

**Table 1. Sources of the fatigue  $\epsilon$ -N data on carbon and low-alloy steels in air environment.**

ANL Mat. ID	Material Specification	Sulfur Content (wt.%)	Test Temperature (°C)	Number of Data Points	Source	Applicable Reference
<u>Carbon Steels</u>						
1	A106-Gr.B	0.015	25, 288	3, 17	ANL	10
3	A106-Gr.B	0.020	25, 288	13, 12	MEA	48-50
4	A106-Gr.C (STS480)	0.006	25	5	JNES (Kanasaki)	136
-	A106-Gr.C (STS480)	0.003	25	2	JNES (Kanasaki)	136
6	A106-Gr.B (STS49)	0.007	25	9	JNES (Higuchi)	136
9	A333-Gr.6 (STS42)	0.015	25, 250, 290	13, 7, 3	JNES (Higuchi)	136
10	A333-Gr.6 (STS42)	0.014	25	7 <sup>a</sup>	JNES (Higuchi)	136
11	A333-Gr.6	0.006	288	1	JNES (Higuchi)	136
12	A333-Gr.6 (STS410)	0.012	25, 100, 200, 288	5, 4, 4, 2	JNES (Nakao), ANL	136, 10
13	A333-Gr.6	0.030	25, 288	7, 6	GE	14-17
14	A333-Gr.6 (STS410)	0.008	25, 289	24, 10	JNES (Hirano)	136
15	A333-Gr.6 (STS410)	0.016	25, 289	12, 5	JNES (Hirano)	136
18	A508-Gr.1 (SFVC2B)	0.004	25, 289	6, 5	JNES (Hirano)	136
19	A508-Gr.1 <sup>b</sup>	0.008	25	14	JNES (PLEX)	136
24	CS	-	25, 170	10, 28	MPA	55,56
<u>Carbon Steel Weld Metals</u>						
-	A336-Gr.6 (STS410)	0.001	25, 288	6, 4	JNES (Hirano)	136
-	A336-Gr.6 (STS410)	0.010	25, 289	5, 5	JNES (Hirano)	136
<u>Low-alloy Steels</u>						
1	A302-Gr.B	0.027	288	7	ANL	10
2	A508-Gr.2	0.003	25	9	JNES (Nakao/Higuchi)	136
6	A508-Gr. 3 (SFVV3)	0.003	25, 288	6, 14	JNES (Nagata)	136
7	A508-Gr. 3 (SFVV3)	0.002	25, 288	7, 8	JNES (Narumoto)	136
8	A508-Gr. 3 (SFVV3)	0.003	25	8	JNES (Narumoto)	136
9	A508-Gr. 3 (SFVV3)	0.005	25, 200	31, 2	JNES (Ikemoto, Iwadate, Kou, Nihei, Fukakura)	136
10	A508-Gr. 3 (SFVV3)	0.003	150, 200, 290	18, 15, 13	JNES (Kou, Fukakura, Iida)	136
11	A508-Gr. 3 (SFVV3)	0.003	25, 200, 290	11, 17,	JNES (Nihei, Kou,	136

ANL Mat. ID	Material Specification	Sulfur Content (wt.%)	Test Temperature (°C)	Number of Data Points	Source	Applicable Reference
				24	Fukakura, Iwadate,)	
12	A508-Gr. 3 (SFVV3)	0.003	25	10	JNES (Higuchi, Endou)	136
13	A508-Gr. 3 (SFVV3)	0.008	25	8 <sup>b</sup>	JNES (Kanasaki)	136
14	A508-Gr. 3	0.002	288	14	Wu & Katada	141
16	A533-Gr. B	0.012	25, 288	6, 16	ANL	10,11,12
17	A533-Gr. B (SQV2A)	0.007	25, 288	14, 14	JNES (Nagata), Wu & Katada	136,141
18	A533-Gr. B (SQV2A)	0.001	25, 350	34, 10	JNES (Kazuo Toyam)	136
19	A533-Gr. B (SQV2A)	0.003	25, 300	6, 6	JNES (Narumoto)	136
20	A533-Gr. B (SQV2A)	0.002	25, 286	9, 8	JNES (Narumoto)	136
21	A533-Gr. B (SQV2A)	0.010	25	18 <sup>c</sup>	JNES (Iida)	136
22	A533-Gr. B (SQV2A)	0.008	25, 150, 200, 250, 289	19, <sup>b</sup> 1, 1, 1, 4	JNES (Hirano)	136
23	A533-Gr. B	0.013	288	7	Wu & Katada	143
28	A533-Gr. B	0.014	270	2	MPA	55,56
29	LAS	-	25, 170	16, 16	MPA	55,56
31	17MnMoV64	0.018	200	3	S/KWU	55,56

<sup>a</sup> Six tests performed under load control were excluded.

<sup>b</sup> Includes test results for thermally aged materials.

<sup>c</sup> Tests performed using a sine waveform, and data include results for thermally aged materials.

In air, the fatigue lives of both carbon and low-alloy steels depend on steel type, temperature, and for some compositions, applied strain rate and sulfide morphology. Fatigue  $\epsilon$ - $N$  data from various investigations on carbon and low-alloy steels are shown in Fig. 27. The best-fit air curves based on the ANL models (Eqs. 24 and 25 from Section 3.1.6) and the ASME Section III mean-data air curves at room temperature (Eqs. 7 and 8 from Section 1.2) are also included in the plots in this figure. The results indicate that, although significant scatter is apparent due to material variability, the fatigue lives of these steels are comparable at less than  $5 \times 10^5$  cycles, and those of low-alloy steels are greater than carbon steels for greater than  $5 \times 10^5$  cycles. In addition, the fatigue life at  $10^6$  cycles of low-alloy steels is higher than that of carbon steels.

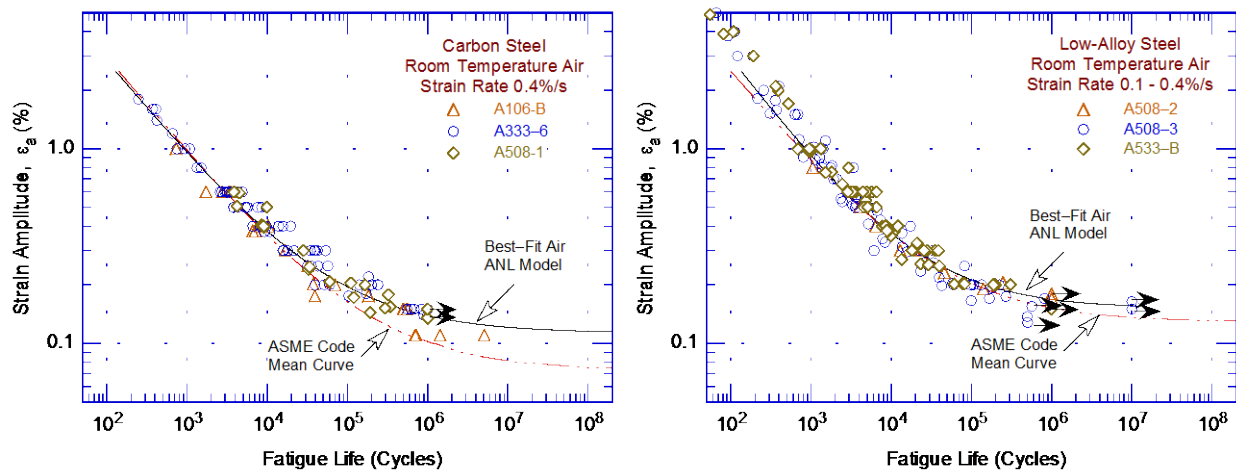


**Figure 27. Fatigue strain vs. life data for carbon and low-alloy steels in air at room temperature (JNUFAD database and Refs. 10,18,19,48).**

The results also indicate that the existing fatigue  $\epsilon$ - $N$  data for low-alloy steels are in good agreement with the ASME mean data curve. The existing data for carbon steels are consistent with the ASME mean data curve for fatigue lives below  $5 \times 10^5$  cycles, and are above the ASME mean data curve at longer lives. Thus, for carbon steels above  $5 \times 10^5$  cycles, the ASME mean data curve is conservative with respect to the existing fatigue  $\epsilon$ - $N$  data.

- The ASME Code mean data air curves for carbon and low-alloy steels (Eqs. 7 and 8) are either consistent with the existing fatigue  $\epsilon$ - $N$  data or are somewhat conservative under some conditions.

### 3.1.2 Temperature

In air, the fatigue lives of both carbon and low-alloy steels decrease with increasing temperature; however, the effect is relatively small (less than a factor of 1.5). The existing fatigue  $\epsilon$ - $N$  data in air at 25–290°C are shown in Fig. 28. As discussed in Section 3.1.1 for each grade of steel, the data represent several heats of material. The solid lines in the plots represent the temperature dependence defined by Eq. 22 in Section 3.1.6. The results indicate a factor of approximately 1.5 decrease in fatigue lives of both carbon and low-alloy steels as the temperature is increased from room temperature to 300°C.

- Variations in the fatigue lives in air due to the effects of temperature for carbon and low-alloy steels were accounted for in the subfactor for “data scatter and material variability.”

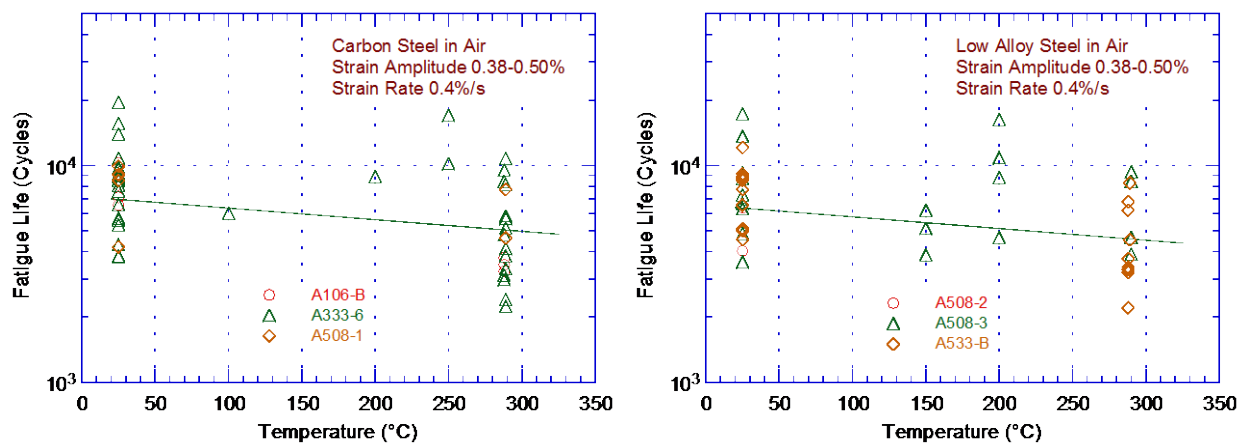


Figure 28. The change in fatigue lives of carbon and low-alloy steels in air as a function of temperature.

### 3.1.3 Strain Rate

The effect of strain rate on the fatigue lives of carbon and low-alloy steels in air appears to depend on the material composition. The existing data indicate that in the temperature range of dynamic strain aging (200–370°C), some heats of carbon and low-alloy steels were sensitive to strain rate; with decreasing strain rate, the fatigue lives in air were either unaffected,<sup>10</sup> decreased for some heats,<sup>211</sup> or increased for others.<sup>212</sup> The carbon and nitrogen contents in the steel are considered to have an important influence on strain rate effects. Inhomogeneous plastic deformation can result in localized plastic strains. This localization retards blunting of propagating cracks that is usually expected when plastic deformation occurs and can result in higher crack growth rates.<sup>211</sup> The increases in fatigue lives were attributed to retardation of

CGRs due to crack branching and suppression of the plastic zone.<sup>212</sup> Furthermore, as discussed earlier, the formation of cracks may be enhanced in the presence of DSA.

- *Variations in fatigue lives in air due to the effects of strain rate for carbon and low-alloy steels were accounted for in the subfactor for “data scatter and material variability.”*

### 3.1.4 Sulfide Morphology

Some high-sulfur steels exhibit very poor fatigue properties in certain orientations because of structural factors such as the distribution and morphology of sulfides in the steel. For example, fatigue tests on a high-sulfur heat of A302-Gr. B steel in three orientations\* in air at 288°C indicated that the fatigue life and fatigue limit in the radial (T2) orientation are lower than those in the rolling (R) and transverse (T1) orientations.<sup>10</sup> At low strain rates, fatigue lives in the T2 orientation were nearly one order of magnitude lower than in the R orientation. In the orientation with poor fatigue resistance, crack propagation occurred preferentially along the sulfide stringers and is facilitated by sulfide cracking.

- *Variations in fatigue lives in air due to differences in sulfide morphology for carbon and low-alloy steels were accounted for in the subfactor for “data scatter and material variability.”*

### 3.1.5 Cyclic Strain Hardening Behavior

The cyclic stress-strain response of carbon and low-alloy steels varies with steel type, temperature, and strain rate. In general, these steels show initial cyclic hardening, followed by cyclic softening or a saturation stage at all strain rates. Carbon steels, with a pearlite and ferrite structure and low yield stress, exhibit significant initial hardening. Low-alloy steels, with a tempered bainite and ferrite structure and a relatively high yield stress, show little or no initial hardening and may exhibit cyclic softening with continued cycling. For both steels, the maximum stress increases as applied strain increases and generally decreases as temperature increases. However, at 200–370°C, these steels exhibited DSA, which resulted in enhanced cyclic hardening, a secondary hardening stage, and negative strain rate sensitivity.<sup>211,212</sup> The temperature range and extent of DSA varied with composition and structure.

The effects of strain rate and temperature on the cyclic stress response of A106-Gr B carbon steel and A533-Gr B low-alloy steel are shown in Fig. 29. For both steels, cyclic stresses were higher at 288°C than at room temperature. At 288°C, all steels exhibited greater cyclic and secondary hardening because of DSA. The extent of hardening increased as the applied strain rate decreased.

- *Cyclic strain hardening behavior influenced the fatigue limits of materials; variations in fatigue lives in air due to the effects of strain hardening for carbon and low-alloy steels were accounted for in the subfactor for “data scatter and material variability.”*

---

\*The three orientations were represented by the direction that was perpendicular to the fracture plane. Both transverse (T1) and radial (T2) directions were perpendicular to the rolling direction, but the fracture plane was across the thickness of the plate in the transverse orientation and parallel to the plate surface in the radial orientation.

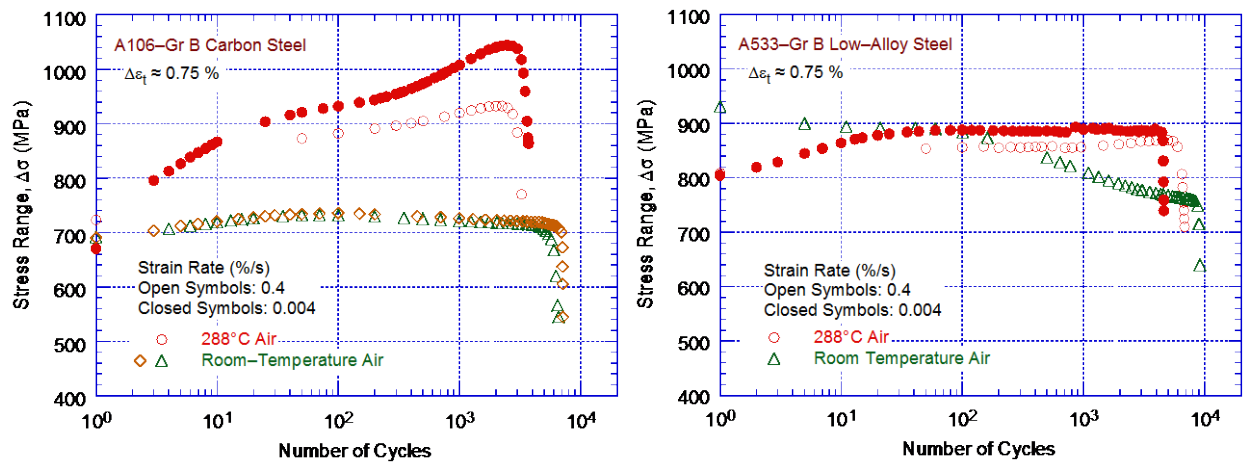


**Figure 29. Effect of strain rate and temperature on cyclic stress of carbon and low-alloy steels.**

### 3.1.6 Fatigue Life Model

ASTM Standard E 739, “Standard Practice for Statistical Analysis of Linear or Linearized Stress–Life ( $S-N$ ) and Strain–Life ( $\epsilon-N$ ) Fatigue Data,”<sup>4</sup> treats fatigue life,  $N$  (or the logarithm of the fatigue life), as the dependent variable, and the controlled variables, e.g., stress or strain, as the independent variable. The coefficients of a “linear” model are commonly established through least-squares curve-fitting of the data using fatigue life as the dependent variable. An optimization program sets the coefficients to minimize the sum of the square of the residual errors, which are the differences between the predicted and actual values of  $N$  or  $\ln(N)$ . However, such an approach may not adequately determine the optimum coefficients for a nonlinear expression such as the Langer curve (Eq. 6), which includes a constant term,  $C$ , related to the fatigue limit. The model does not address the fact that at low strain amplitudes, most of the error in life is due to uncertainty associated with either measurement of stress or strain or variation in threshold strain caused by material variability. A predictive model based on a least-squares fit on  $N$  or  $\ln(N)$  is biased for low strain amplitude ( $\epsilon_a$ ); also, data obtained at strain amplitudes less than the constant  $C$  in Eq. 6 cannot be included in the analysis. On the other hand, a least-squares fit on  $\epsilon_a$  does not work well for higher strain amplitudes. The two kinds of models are transformations of each other, although the precise values of the coefficients differ.

In the statistical model presented in Refs. 130 and 10, the two approaches were combined by minimizing the sum of the squared Cartesian distances from the data points to the predicted curve (Fig. 30). For low  $\epsilon_a$ , this is very close to optimizing the sum of squared errors in predicted  $\epsilon_a$ ; at high  $\epsilon_a$ , this is very close to optimizing the sum of squared errors in predicted life; and at medium  $\epsilon_a$ , this model combines both factors. Therefore, the use of this model addresses the weaknesses identified previously for the model based on residual errors alone. To perform this alternate optimization, it was necessary to normalize the  $x$  and  $y$  axes by assigning relative weights that are used in combining the error in life and strain amplitude because the  $x$  and  $y$ -axes are not in comparable units. In this analysis, errors in strain amplitude (%) were weighted 20 times as heavily as errors in  $\ln(N)$ . A value of 20 was selected for two related reasons. First, this factor led to approximately equal weighting of low and high strain amplitude data in the least-squared error computation of model coefficients. Second, when the factor was applied to the model to generate probability curves, it yielded a standard deviation on strain amplitude comparable to that obtained from the best fit of the high cycle fatigue data to Eq. 1.<sup>130</sup> Because there was judgment applied in the selection of this value, a sensitivity analysis was performed that demonstrated that the coefficients of the model do not

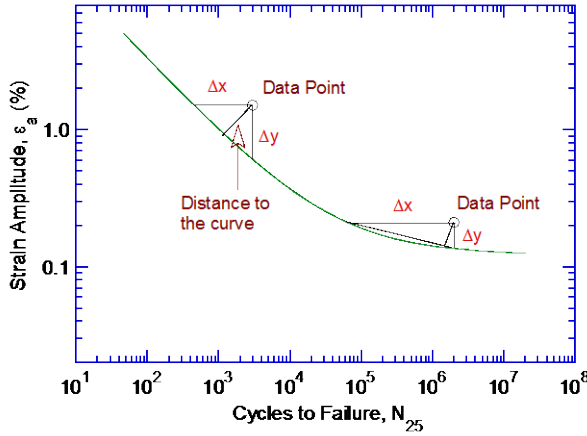


**Figure 30.**  
Schematic diagram of the best-fit of the experimental data by minimizing the distance between the data point and the S-N curve.

change significantly for weight factors between 10 and 25. The normal distance from the best-fit curve was estimated as

$$D = \left\{ (x - \hat{x})^2 + [k(y - \hat{y})]^2 \right\}^{1/2}, \quad (19)$$

where  $\hat{x}$  and  $\hat{y}$  represent predicted values, and  $k = 20$ . Although R-squared is only applicable for linear regression, an approximate value for combined R-squared was derived for illustrative purposes. The combined R-squared was defined as

$$1 - \left( \frac{\sum D^2}{\sum Z^2} \right), \quad (20)$$

$$\text{where } Z = \left\{ (x - x')^2 + [k(y - y')]^2 \right\}^{1/2} \quad (21)$$

and  $x'$  and  $y'$  represent the 25th percentile of  $x$  and  $y$ , respectively. The 25th percentile is selected instead of the mean because the mean values are exaggerated due to the nonlinearity of the equations, and because higher values are less influential to the model. The value from Eq. 20 is not a true R-squared value, but often falls between the  $x$ -based R-squared and the  $y$ -based R-squared values; therefore, it is considered to be a better qualitative measure of the model's predictive accuracy because it is not distorted in the way  $x$ -based R-squared and  $y$ -based R-squared measures would be.

Fatigue life models presented in the original version of NUREG/CR-6909 for estimating the fatigue lives in air of carbon and low-alloy steels in air were developed at ANL as best fits of a Langer curve to an updated version of the PVRC database.<sup>10,46</sup> From those best fits, the fatigue lives,  $N$ , of carbon steels was represented by

$$\ln(N) = 6.614 - 0.00124 T - 1.975 \ln(\varepsilon_a - 0.113), \quad (22)$$

and that of low-alloy steels by

$$\ln(N) = 6.480 - 0.00124 T - 1.808 \ln(\varepsilon_a - 0.151), \quad (23)$$

where  $\varepsilon_a$  is applied strain amplitude (%), and  $T$  is the test temperature ( $^{\circ}\text{C}$ ). Thus, in room-temperature ( $25^{\circ}\text{C}$ ) air, the fatigue lives of carbon steels was expressed as

$$\ln(N) = 6.583 - 1.975 \ln(\varepsilon_a - 0.113), \quad (24)$$

and that of low-alloy steels, by

$$\ln(N) = 6.449 - 1.808 \ln(\varepsilon_a - 0.151). \quad (25)$$

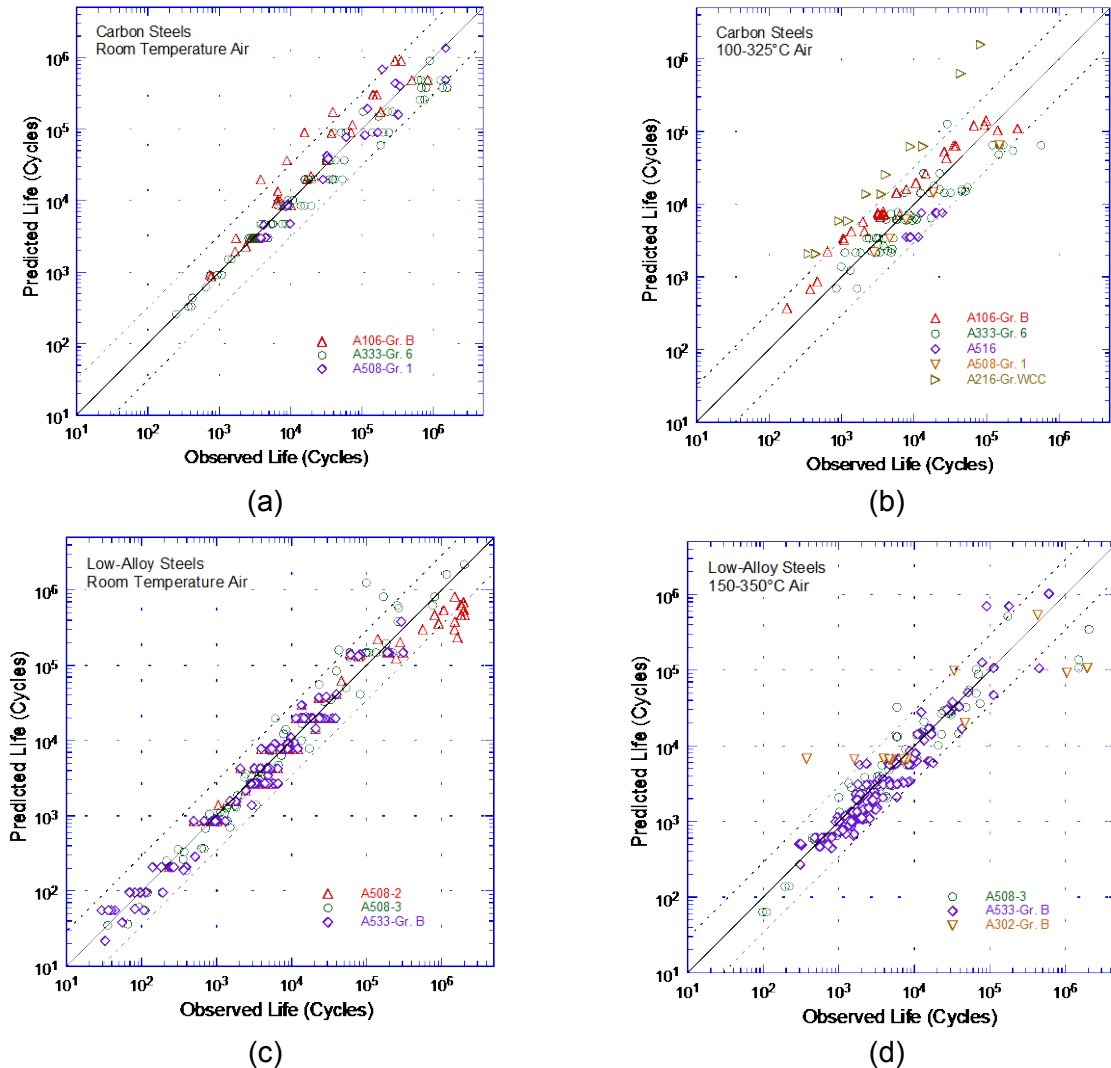


**Figure 31. Experimental and predicted fatigue lives of (a, b) carbon steels and (c, d) low-alloy steels in air.**

Note that Eqs. 24 and 25 were based on incorporation of additional fatigue data and the analysis presented in Section 4.1.7 of Ref. 137; the values of the constant  $A$  in the equations were updated from the values reported in NUREG/CR-6583<sup>10</sup> and NUREG/CR-6815.<sup>46</sup> The heat-to-heat variability of these equations is discussed further in Section 3.1.7 of this report. Relative to the models presented in NUREG/CR-6583, the fatigue lives predicted by the models in the original revision to NUREG/CR-6909 were approximately 2% higher for carbon steel and approximately 16% lower for low-alloy steels. The predicted fatigue lives showed good

agreement with the experimental values; the experimental and predicted values were within a factor of 3. The experimental and predicted fatigue lives of carbon and low-alloy steel data using the expressions defined by Eqs. 24 and 25 are shown in Fig. 31. As discussed in Section 3.1.7, the greater-than-observed fatigue lives for A106-Gr B steel at room temperature and for A216-Gr. WCC at 325°C appear to be due to heat-to-heat variability and not temperature effects.

- *The fatigue life models for carbon and low-alloy steels represent mean values of fatigue lives in air for specimens tested under fully reversed strain-controlled loading. The effects of parameters (such as mean stress, surface finish, size and geometry, and loading history) known to influence fatigue lives were accounted for in the several subfactors that were applied to the mean data air curve to obtain the fatigue design air curve.*

### **3.1.7 Heat-to-Heat Variability**

Several factors, such as small differences in material composition and structure, can change the tensile and fatigue properties of materials. The effect of interstitial element content on DSA and the effect of sulfide morphology on fatigue lives are discussed in Sections 3.1.5 and 3.1.4, respectively. The effect of tensile strength on fatigue lives was included in the expression for the ASME mean data air curve described in the Section III criteria document, i.e., constant  $A_f$  in Eq. 2. In addition, the material fatigue limit was correlated with tensile strength, e.g., the fatigue limit increases with increasing tensile yield stress.<sup>213</sup>

The effects of material variability and data scatter must be included in the data evaluation to ensure that the resulting design curves not only describe the available test data adequately, but also adequately describe the fatigue lives of the much larger number of heats of material that are found in the field compared to the limited number of heats used for testing. The effects of material variability and data scatter are often evaluated by comparing the experimental data to a specific model for fatigue crack initiation, e.g., the best fit (in some sense) to the data. The adequacy of the evaluation depends on the sample of data used in the analysis. For example, if most of the data were obtained from a heat of material that has poor resistance to fatigue damage or under loading conditions that show significant environmental effects, the results may be conservative for most of the materials or service conditions of interest. Conversely, if most data are from a heat of material with a high resistance to fatigue damage, the results may be nonconservative for many heats in service.

Another method to assess the effect of material variability and data scatter is to consider the best-fit curves determined from tests on individual heats of materials or loading conditions as samples of a much larger population of heats of materials and service conditions of interest. To do this, the fatigue behavior of each of the heats or loading conditions was characterized by the value of the constant  $A$  in Eq. 6. The values of  $A$  for the various data sets were rank-ordered, and median ranks were used to estimate the cumulative distribution of  $A$  for the population.<sup>214,215</sup> The distributions were fit to lognormal curves. No rigorous statistical evaluation was performed for these curves, but the fits appeared reasonable and described the observed variability adequately. The data were normalized to room-temperature values using Eqs. 22 and 23 (Section 3.1.6). The median value of the constant  $A$ , reported in the original revision of NUREG/CR-6909, was 6.583 and 6.449, respectively, for the fatigue lives of carbon steels and low-alloy steels in room-temperature air. The estimated cumulative distributions of constant  $A$  in the ANL model for fatigue lives for heats of carbon and low-alloy steels included in the original revision of NUREG/CR-6909 and those included in this report are shown in Fig. 32.

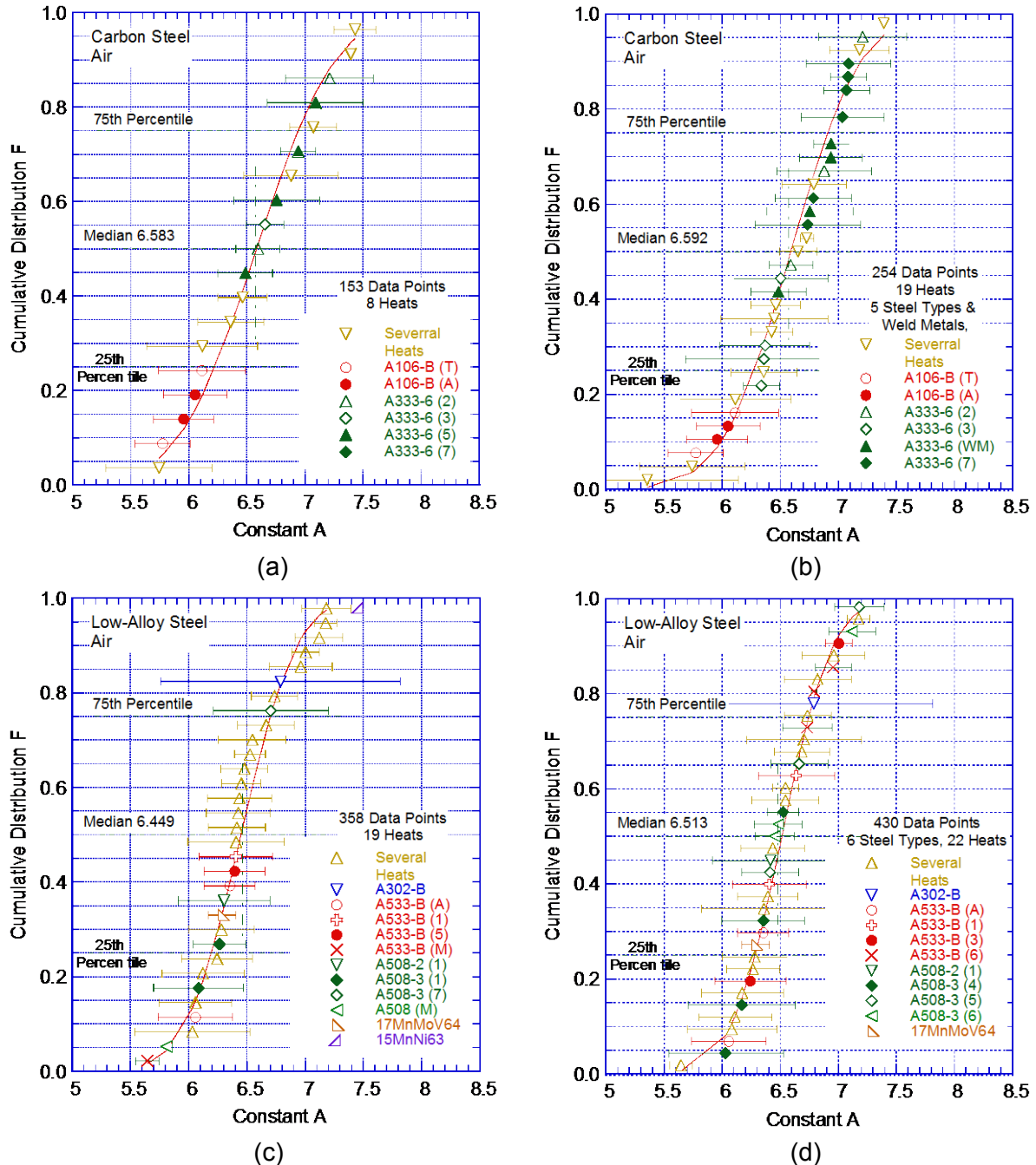


Figure 32. Estimated cumulative distribution of constant A in the ANL models for fatigue life data in the original revision of NUREG/CR-6909 (a, c) and this report (b, d); (a, b) for heats of carbon steels and (c, d) low-alloy steels in air.

The results indicate that the ANL fatigue models presented in the original revision of NUREG/CR-6909 for predicting fatigue lives of carbon and low alloy steels in air remain valid. In spite of a significant increase in the number of data points, the median value of the constant A in Eq. 6 did not change significantly for carbon steels (changed from 6.583 to 6.593) or for low-alloy steels (changed from 6.449 to 6.513). Note that the two heats of A106-Gr B carbon steel were in the 10<sup>th</sup> to 25<sup>th</sup> percentile of the data, i.e., the fatigue lives of these heats were much lower than the average value for carbon steels. Also, the average value of the constant A for the A216-Gr. WCC steel at 325°C (after adjusting for temperature effects) was 4.899, which

is significantly lower than the median value of 6.583 for carbon steels. Therefore, it was not included in the reanalysis of the updated fatigue  $\epsilon$ -N database, and the value of the constant A for A216-Gr. WCC is not shown in Fig. 32.

As discussed in the original revision of NUREG/CR-6909, the A values that describe the 5th percentile of these distributions give fatigue  $\epsilon$ -N curves that are expected to bound the fatigue lives of 95% of the heats of the materials tested. The cumulative distributions of A values in Fig. 32 contain two potential sources of error. The means and standard deviations of the populations must be estimated from the means and standard deviations of the samples,<sup>216</sup> and confidence bounds must be obtained on the population means and standard deviations in terms of the sample means and standard deviations. Secondly, even these conditions did not fully address the uncertainties in the distributions because of the large uncertainties in the sample values themselves, i.e., the “horizontal” uncertainty in the actual value of A for a heat of material, as indicated by the error bars in Fig. 32. Therefore, a Monte Carlo analysis was performed to address both sources of uncertainty. The results for the median values and standard deviations of the constant A from the Monte Carlo analysis did not differ significantly from those determined directly from the experimental values.

The results for carbon and low-alloy steels are summarized in Tables 2 and 3, respectively, in terms of values for the constant A that provide bounds for the portion of the population and the confidence that is desired in the estimates of the bounds. In air, the 5<sup>th</sup> percentile value of constant A at a 95% confidence level was 5.559 for carbon steels and 5.689 for low-alloy steels. From Fig. 32. Since the reanalysis did not change the constants significantly, the median values of the constant A for carbon and low-alloy steels were not changed in this report. Thus, constant A for the sample remains 6.583 for carbon steels and 6.449 for low-alloy steels, and the 95/95 values of the factor to account for material variability and data scatter are 2.8 and 2.1 on life for carbon and low-alloy steels, respectively. These factors provide 95% confidence that the resultant lives are greater than those observed for 95% of the materials of interest.

- *The mean data air curves for carbon and low-alloy steels used to develop the fatigue design air curves represented the average fatigue behavior; heat-to-heat variability was included in the subfactor that was applied to the mean data air curve to obtain the fatigue design air curve to account for “data scatter and material variability.”*

**Table 2. Values of constant A in the ANL fatigue life model for carbon steels in air and the factors on life as a function of confidence level and percentage of population bounded.**

Confidence Level	Percentage of Population Bounded (Percentile Distribution of A)				
	95 (5)	90 (10)	75 (25)	67 (33)	50 (50)
	Values of Constant A				
50	5.798	5.971	6.261	6.373	6.583
75	5.700	5.883	6.183	6.295	6.500
95	5.559	5.756	6.069	6.183	6.381
	Factors on Life				
50	2.2	1.8	1.4	1.2	1.0
75	2.4	2.0	1.5	1.3	1.1
95	2.8	2.3	1.7	1.5	1.2

**Table 3. Values of constant A in the ANL fatigue life model for low-alloy steels in air and the factors on life as a function of confidence level and percentage of population bounded.**

Confidence Level	Percentage of Population Bounded (Percentile Distribution of A)				
	95 (5)	90 (10)	75 (25)	67 (33)	50 (50)
Values of Constant A					
50	5.832	5.968	6.196	6.284	6.449
75	5.774	5.916	6.150	6.239	6.403
95	5.689	5.840	6.085	6.175	6.337
Factors on Life					
50	1.9	1.6	1.3	1.2	1.0
75	2.0	1.7	1.3	1.2	1.0
95	2.1	1.8	1.4	1.3	1.1

### 3.1.8 Fatigue $\epsilon$ -N Behavior of Weld Metals

Available fatigue  $\epsilon$ -N data for carbon and low-alloy steel weld metals in air at room temperature and 289°C are plotted in Fig. 33. The results indicated that, in air, the fatigue lives of carbon and low-alloy steel weld metals were slightly lower than the mean  $\epsilon$ -N behavior of non-welded carbon or low-alloy steel test specimens. Except for one data set for CM US-56B/MF-27 weld metal for which fatigue lives were a factor 2 lower than the mean data curves, the fatigue lives of the other data sets were marginally lower. The results also indicated that the fatigue lives at 289°C were slightly lower than at room temperature. Despite these observations, the available fatigue  $\epsilon$ -N data for carbon and low-alloy steel weld metals were insufficient to accurately establish their fatigue behavior relative to the mean data air curve for carbon steels or low-alloy steels, respectively.

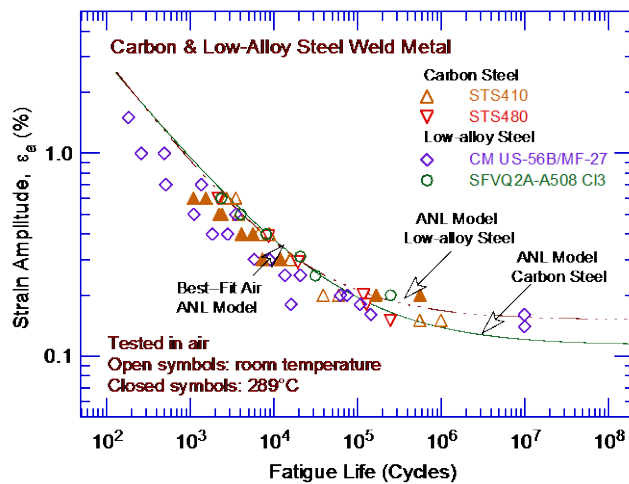


**Figure 33. Fatigue  $\epsilon$ -N behavior for carbon and low-alloy steel weld metals in air at room temperature and 289°C (Ref. 136).**

- *Until additional fatigue  $\epsilon$ -N data for carbon and low-alloy steel weld metals are available, the fatigue mean air curves for carbon steel or low-alloy steels may also be used for weld metals.*

### 3.1.9 Surface Finish

The effect of surface finish was considered to account for the difference in fatigue lives expected in an actual component with an industrial-grade surface finish compared to the smooth polished surface of test specimens. Fatigue lives are sensitive to surface finish; cracks can initiate at surface irregularities that are normal to the axis of applied stress. The height,

spacing, shape, and distribution of surface irregularities are important for crack initiation. The most common measure of roughness is average surface roughness,  $R_a$ , which is a measure of the height of the irregularities. Investigations of the effects of surface roughness on the low-cycle fatigue of Type 304 SS in air at 593°C indicated that fatigue lives decreased as surface roughness increased.<sup>217,218</sup> The effect of roughness on crack initiation,  $N_i(R)$ , is given by

$$N_i(R) = 1012 R_q^{-0.21}, \quad (26)$$

where the root-mean-square (RMS) value of surface roughness,  $R_q$ , is in  $\mu\text{m}$ . Typical values of  $R_a$  for surfaces finished by different metalworking processes in the automotive industry<sup>219</sup> indicated that a value of  $R_a$  of 3  $\mu\text{m}$  (or an  $R_q$  of 4  $\mu\text{m}$ ) represented the maximum surface roughness for drawing/extrusion, grinding, honing, and polishing processes, and a mean value for the roughness range for milling or turning processes. For carbon or low-alloy steels, an  $R_q$  of 4  $\mu\text{m}$  in Eq. 26 would decrease fatigue life by a factor of 3.7 (the  $R_q$  of a smooth polished specimen is approximately 0.0075  $\mu\text{m}$ ).<sup>217</sup>

A fatigue test was conducted on a A106-Gr B carbon steel specimen that was intentionally roughened in a lathe, under controlled conditions, with 50-grit sandpaper to produce circumferential scratches with an average roughness of 1.2  $\mu\text{m}$  and an  $R_q$  of 1.6  $\mu\text{m}$  (approximately 62 micro in.).<sup>46</sup> The results for smooth and roughened specimens are shown in Fig. 34. In air, the fatigue life of a roughened A106-Gr B specimen was a factor of approximately 3 lower than that of smooth specimens. Another study of the effect of surface finish on the fatigue lives of carbon steels in room-temperature air showed a factor of 2 decrease in life when  $R_a$  was increased from 0.3 to 5.3  $\mu\text{m}$ .<sup>220</sup> These results are consistent with Eq. 26. Thus, a factor of 2 to 3 on cycles is necessary to account for surface finish effects on the fatigue lives of carbon and low-alloy steels.

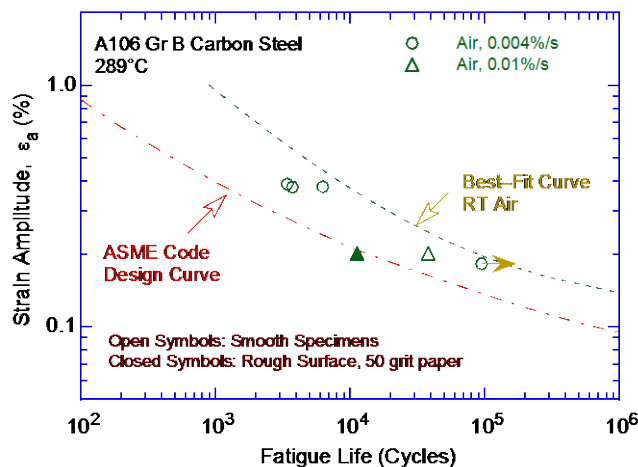


**Figure 34.**  
Effect of surface finish on the fatigue life of A106-Gr B carbon steel in air at 289°C (Ref. 46).

- The effect of surface finish was included as part of the “surface finish and environment” subfactor that was applied to the mean data air curves to obtain the fatigue design air curves for carbon and low-alloy steels.

### 3.1.10 Extension of the Best-Fit Mean Curve from $10^6$ to $10^{11}$ Cycles

The experimental fatigue  $\epsilon$ - $N$  air curves that were used to develop the 2011 ASME Code Section III fatigue design air curve for carbon and low-alloy steels were based on low-cycle fatigue data (less than  $2 \times 10^5$  cycles). The design air curves proposed in this report were

developed from a larger database that included fatigue lives up to  $10^8$  cycles. Both the ASME mean air curves and the ANL models in this report used the modified Langer equation to express the best-fit mean air curves; they are not recommended for estimating fatigue lives beyond the range of the experimental data, i.e., in the high-cycle fatigue regime.

An extension of the current high-cycle fatigue design curves in Section III and Section VIII, Division 2 of the ASME Code for carbon and low-alloy steels from  $10^6$  to  $10^{11}$  cycles was proposed by W. J. O'Donnell to the ASME Section III Subgroup on Fatigue Strength.\* In the high-cycle regime at temperatures not exceeding  $371^\circ\text{C}$  ( $700^\circ\text{F}$ ), the stress amplitude vs. life relationship is expressed as

$$S_a = E\varepsilon_a = C_1N^{-0.05}, \quad (27)$$

where  $\varepsilon_a$  is applied strain amplitude,  $E$  is the elastic modulus,  $N$  is the fatigue life, and  $C_1$  is a constant. A fatigue life exponent of  $-0.05$  was selected based on the fatigue stress range vs. fatigue life data on plain plates, notched plates, and typical welded structures given in Welding Research Council (WRC) Bulletin 398.<sup>221</sup> Because the data were obtained from load-controlled tests with an  $R$  ratio of zero, they take into account the effect of maximum mean stresses and may over-estimate the effect of mean stress under strain-controlled loading conditions. In addition, the fatigue data presented in WRC Bulletin 398 extend only up to  $5 \times 10^6$  cycles; extrapolation of the results to  $10^{11}$  cycles using a fatigue life exponent of  $-0.05$  may yield overly conservative estimates of fatigue life. Finally, ASME received feedback from the evaluation of plant trouble reports, laboratory tests of socket welded joints, and plant operating experience that supported their use of Eq. 27.

Manjoine and Johnson<sup>213</sup> developed fatigue design curves up to  $10^{11}$  cycles for carbon steels and austenitic SSs from inelastic and elastic strain relationships, which were correlated with ultimate tensile strength. The log-log plots of the elastic strain amplitudes vs. fatigue life data were represented by a bilinear curve. In the high-cycle regime, the elastic-strain-vs.-life curve had a small negative slope instead of a fatigue limit.<sup>213</sup> For carbon steel data at room temperature and  $371^\circ\text{C}$  ( $700^\circ\text{F}$ ) and fatigue lives extending up to  $4 \times 10^7$  cycles, Manjoine and Johnson obtained an exponent of  $-0.01$ . The fatigue  $\varepsilon$ - $N$  data used in this report at room temperature and with fatigue lives up to  $10^8$  cycles yielded a fatigue life exponent of approximately  $-0.007$  for both carbon and low-alloy steels. Because the data are limited, the more conservative exponent value (i.e.,  $-0.01$ ) obtained by Manjoine and Johnson<sup>213</sup> was used in the initial edition of NUREG/CR-6909 report. In the high-cycle regime, the applied stress amplitude was expressed by the relationship

$$S_a = E\varepsilon_a = C_2N^{-0.01}. \quad (28)$$

In the initial edition of the NUREG/CR-6909, Eq. 28 was used to extend the best-fit mean air curves beyond  $10^6$  cycles (in the high-cycle regime); thus, the mean stress-life curves exhibited a small negative slope instead of the fatigue limit predicted by the modified Langer equation. The selection of a smaller value for the fatigue life exponent to extend the best-fit curve was based on evaluation of thermal fatigue data, which are bounded by Eq. 28. However, the high-cycle thermal fatigue data are limited, and the data do not consider mechanical fatigue (i.e., vibration).

---

\*W. J. O'Donnell, "Proposed Extension of ASME Code Fatigue Design Curves for Carbon and Low-Alloy Steels from  $10^6$  to  $10^{11}$  Cycles for Temperatures not Exceeding  $700^\circ\text{F}$ ," presented to ASME Subgroup on Fatigue Strength, December 4, 1996.

As discussed earlier in this report, the classical fatigue limit for ferrous alloys is a consequence of performing fatigue tests at constant cyclic stress or strain range and determining the threshold range below which cracks cannot propagate beyond microstructural barriers and fatigue failures do not occur. Miller and O'Donnell<sup>222</sup> discussed the causes that lead to elimination of the fatigue limit, including the introduction of transitory cyclic processes or time-dependent mechanisms that permit a previously nonpropagating crack to grow across microstructural barriers. The authors argued that the most probable significant condition for engineering plants designed to last beyond  $10^6$  cycles is the introduction of very low cyclic stress vibrations at high mean stress levels, with or without other mechanisms such as corrosion or time-dependent mechanisms. Therefore, in this report, to better accommodate the vibration data (e.g., Ref. 221), the extension of the fatigue stress or strain-life curves beyond  $10^6$  cycles is based on the more conservative Eq. 27 rather than Eq. 28, i.e., an exponent of -0.05 is used. The value of constant  $C_1$  was determined from the value of strain amplitude at which the slope of the curve expressed by Eq. 27 is the same as that of the fatigue  $\epsilon$ -N curve expressed by Eq. 24 for carbon steels or Eq. 25 for low-alloy steels.

- *The fatigue design air curves for carbon and low-alloy steels were extended beyond  $10^6$  cycles using Eq. 27, which is consistent with the methodology used to develop the fatigue design air curve for carbon and low-alloy steels in the 2011 Addenda of ASME Code Section III.*

### 3.1.11 Fatigue Design Curves

Although the two equations for the ASME Code mean air curves for carbon and low-alloy steels (i.e., Eqs. 7 and 8) are significantly different (because the mean stress correction is much larger for the low-alloy steels), the differences between the curves are much smaller when mean stress corrections are considered. Thus, ASME Code, Section III provides one common fatigue design air curve for both carbon and low-alloy steels. The ASME Code fatigue design air curves for carbon and low-alloy steels were obtained from the best-fit curves in air (i.e., Eqs. 7 and 8, respectively) by first correcting for mean stress effects by using the modified Goodman relationship, followed by reducing the mean-stress adjusted curves by factors of 2 on stress or 20 on cycles, whichever was more conservative. The discussions presented in Section 7.5 of the original edition of NUREG/CR-6909 indicated that the current ASME Code requirement of a factor of 20 on cycles, to account for the effects of material variability and data scatter, specimen size, surface finish, and loading history, was conservative by at least a factor of 1.7 for these steels. To reduce this conservatism, separate fatigue design air curves based on the ANL models for carbon and low-alloy steels were developed using factors of 12 on life and 2 on stress. The fatigue design air curves developed following this approach for carbon and low-alloy steels are shown in Fig. 35. The difference between the design air curves based on the ANL models and the ASME Code design air curve is due to the difference in the factor on life used to obtain these curves i.e., 20 for the ASME Code curve and 12 for the ANL curves. In addition, for the carbon steel design air curve, the conservatism in the high-cycle regime was corrected in the ANL models.

The ASME Code fatigue design air curve for carbon and low-alloy steels with ultimate tensile strength (UTS) less than 552 MPa (80 ksi) included an extension of the design curve to  $10^{11}$  cycles, which was proposed by W. J. O'Donnell and was based on Eq. 27 in this report. In the initial edition of NUREG/CR-6909, the fatigue design air curves developed based on the ANL fatigue  $\epsilon$ -N models were extended in the high-cycle regime beyond  $10^6$  cycles using Eq. 28 instead of Eq. 27. However, as discussed in Section 3.1.10, and to better accommodate the field vibration data, the extension of the fatigue design curves beyond  $10^6$  cycles is based on Eq. 27. The values of stress amplitude ( $S_a$ ) vs. cycles for the ASME Code Section III fatigue

design air curve with O'Donnell's extension, and the design curve based on Eq. 27 and the ANL fatigue life models from Eq. 24 for carbon steels and Eq. 25 for low-alloy steels, are listed in Table 4. The corresponding fatigue design air curves are shown in Figs. 36 and 37, respectively, for carbon and low-alloy steels. The values of stress amplitude vs. cycles presented in the initial edition of NUREG/CR-6909 for the fatigue design air curves based on the ANL fatigue  $\epsilon$ -N models and Eq. 28 are presented in Table 5 for comparison.

- *Separate fatigue design air curves were developed for carbon and low-alloy steels. These curves were developed from the ANL models using factors of 12 on life and 2 on stress. The results indicated that the ASME Code Section III fatigue design air curve for carbon and low-alloy steels for ultimate tensile strengths less than 552 MPa (80 ksi) was conservative with respect to the existing fatigue  $\epsilon$ -N data, particularly for carbon steels. In this report, the extension of the fatigue design air curves beyond  $10^6$  cycles was based on Eq. 27 instead of Eq. 28 used in the initial revision to NUREG/CR-6909.*

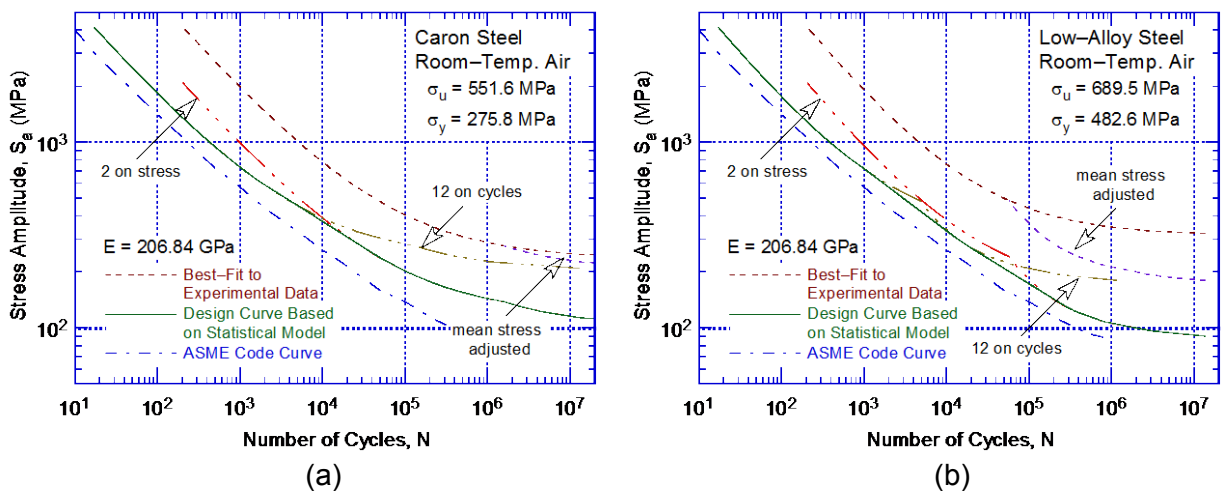


**Figure 35. Fatigue design curves based on the ANL model for (a) carbon steels and (b) low-alloy steels in air.**

**Table 4. Fatigue design curves for carbon and low-alloy steels including proposed updated extension to  $10^{11}$  cycles.**

Cycles	Stress Amplitude (MPa/ksi)			Cycles	Stress Amplitude (MPa/ksi)		
	ASME Code Curve	Eqs. 24 & 27 Carbon Steel	Eqs. 25 & 27 Low-Alloy Steel		ASME Code Curve	Eqs. 24 & 27 Carbon Steel	Eqs. 25 & 27 Low-Alloy Steel
1 E+01	3999 (580)	5355 (777)	5467 (793)	2 E+05	114 (16.5)	176 (25.5)	141 (20.5)
2 E+01	2827 (410)	3830 (556)	3880 (563)	5 E+05	93.1 (13.5)	154 (22.3)	116 (16.8)
5 E+01	1896 (275)	2510 (364)	2438 (354)	1 E+06	86.2 (12.5)	142 (20.6)	106 (15.4)
1 E+02	1413 (205)	1820 (264)	1760 (255)	2 E+06		130 (18.9)	98 (14.2)
2 E+02	1069 (155)	1355 (197)	1300 (189)	5 E+06		120 (17.4)	94 (13.6)
5 E+02	724 (105)	935 (136)	900 (131)	1 E+07	76.8 (11.1)	115 (16.7)	91 (13.2)
1 E+03	572 (83)	733 (106)	720 (104)	2 E+07		110 (16.0)	88 (12.7)
2 E+03	441 (64)	584 (84.7)	576 (83.5)	5 E+07		105 (15.2)	84 (12.2)
5 E+03	331 (48)	451 (65.4)	432 (62.7)	1 E+08	68.5 (9.9)	101 (14.7)	81 (11.8)
1 E+04	262 (38)	373 (54.1)	342 (49.6)	1 E+09	61.1 (8.8)	90 (13.1)	72.3 (10.5)
2 E+04	214 (31)	305 (44.2)	276 (40.0)	1 E+10	54.4 (7.9)	81 (11.7)	64.4 (9.3)
5 E+04	159 (23)	238 (34.5)	210 (30.5)	1 E+11	48.5 (7.0)	72 (10.4)	57.4 (8.3)
1 E+05	138 (20.0)	201 (29.2)	172 (24.9)				

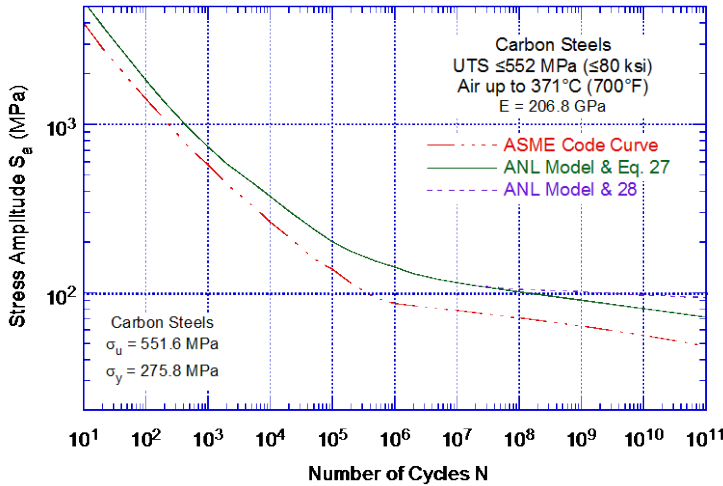


**Figure 36.** Fatigue design curve for carbon steels in air. The curve developed from the ANL model is based on factors of 12 on life and 2 on stress.

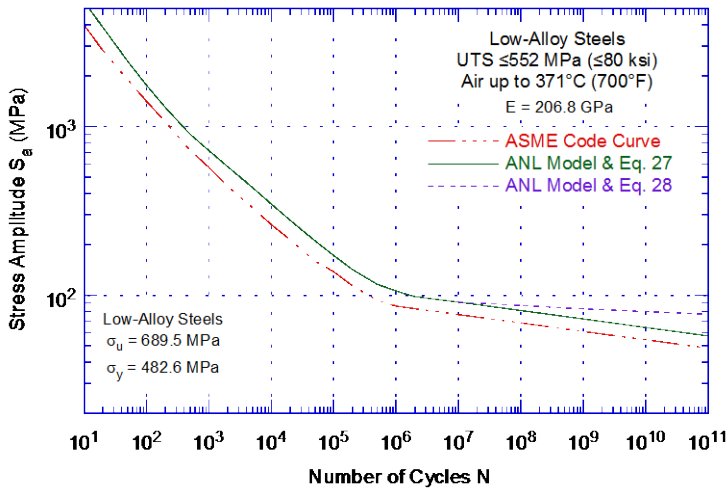


**Figure 37.** Fatigue design curve for low-alloy steels in air. The curve developed from the ANL model is based on factors of 12 on life and 2 on stress.

**Table 5. Fatigue design curves for carbon and low-alloy steels and the extension to 10<sup>11</sup> cycles proposed in the initial revision to NUREG/CR-6909.**

Cycles	Stress Amplitude (MPa/ksi)			Cycles	Stress Amplitude (MPa/ksi)		
	ASME Code Curve	Eqs. 24 & 28 Carbon Steel	Eqs. 25 & 28 Low-Alloy Steel		ASME Code Curve	Eqs. 24 & 28 Carbon Steel	Eqs. 25 & 28 Low-Alloy Steel
1 E+01	3999 (580)	5355 (777)	5467 (793)	2 E+05	114 (16.5)	176 (25.5)	141 (20.5)
2 E+01	2827 (410)	3830 (556)	3880 (563)	5 E+05	93 (13.5)	154 (22.3)	116 (16.8)
5 E+01	1896 (275)	2510 (364)	2438 (354)	1 E+06	86 (12.5)	142 (20.6)	106 (15.4)
1 E+02	1413 (205)	1820 (264)	1760 (255)	2 E+06		130 (18.9)	98 (14.2)
2 E+02	1069 (155)	1355 (197)	1300 (189)	5 E+06		120 (17.4)	94 (13.6)
5 E+02	724 (105)	935 (136)	900 (131)	1 E+07	76.5 (11.1)	115 (16.7)	91 (13.2)
1 E+03	572 (83)	733 (106)	720 (104)	2 E+07		110 (16.0)	90 (13.1)
2 E+03	441 (64)	584 (84.7)	576 (83.5)	5 E+07		107 (15.5)	88 (12.8)
5 E+03	331 (48)	451 (65.4)	432 (62.7)	1 E+08	68.3 (9.9)	105 (15.2)	87 (12.6)
1 E+04	262 (38)	373 (54.1)	342 (49.6)	1 E+09	60.7 (8.8)	102 (14.8)	83 (12.0)
2 E+04	214 (31)	305 (44.2)	276 (40.0)	1 E+010	54.5 (7.9)	97 (14.1)	80 (11.6)
5 E+04	159 (23)	238 (34.5)	210 (30.5)	1 E+011	48.3 (7.0)	94 (13.6)	77 (11.2)
1 E+05	138 (20.0)	201 (29.2)	172 (24.9)				

## 3.2 Wrought and Cast Austenitic Stainless Steels and Weld Metals

### 3.2.1 Experimental Data

The relevant fatigue  $\epsilon$ - $N$  data used to evaluate wrought and cast austenitic SSs in air include the large JNES database;<sup>136</sup> data developed at ANL<sup>45</sup> and GE;<sup>14,15</sup> results of Keller,<sup>63</sup> and the data<sup>64,65,70,73</sup> compiled by Jaske and O'Donnell<sup>61</sup> for developing fatigue design criteria for pressure vessel alloys. The database is composed of 770 tests from which 622 data points were obtained; 332 tests (267 data points) on Type 304 SS, 315 tests (244 data points) on Type 316 SS, 96 tests (77 data points) on SS weld metals (34 tests (23 data points) on Type 304 SS and 62 tests (54 data points) on Type 316 SS weld metals), and 37 tests (34 data points) for CF-8M grade of cast austenitic SSs. Both low-carbon and high-carbon grades of Types 304 and 316 SS are included in the database. Out of these, 432 data points were obtained at room temperature, 7 data points were obtained at 100-200°C, and 183 data points were obtained at 250-325°C. Another 70 data points obtained at temperatures of 400°C and above were not included in the present reanalysis to verify the fatigue  $\epsilon$ - $N$  expression for austenitic SSs in air because they were outside of the temperature range experienced in LWRs. As discussed in Section 3.2.4, the fatigue  $\epsilon$ - $N$  data for austenitic SSs shows some temperature dependence above 460°C. A summary of the points included in the updated database used for the present analyses, as categorized by material type and test environment, is presented in Table 6. Other material information such as chemical composition, heat treatment, and room temperature tensile properties of the various types and heats of materials is given in Appendix B.

**Table 6. Sources of the fatigue  $\epsilon$ - $N$  data on wrought and cast austenitic stainless steels in an air environment.**

ANL Mat. ID	Material Heat Designation <sup>a</sup>	Carbon Content (wt.%)	Test Temperature (°C)	No. of Data Points	Source	Applicable Reference
<u>Type 304 Stainless Steels</u>						
1	304-1	0.050	288	10	JNES (Tokimasa)	136
2	304-30, 31	0.050	25	10, 4	JNES (Yamanaka),	136
3	304-3H	0.060	25	8	JNES (Enomoto),	136
4	304-4B	0.050	25	10	JNES (Kitigawa)	136
5	304-5B	0.060	25	3	JNES (Sakamoto)	136
6	304-6B	0.060	25	11	JNES (Tsunenari)	136
7	304-7B	0.059	25	10	JNES (Kasahara)	136
8	304-8B	0.060	25	6	JNES (Ichihara)	136
10	304-10, 10H	0.060	25, 300, 100	2, 7, 2	JNES (Usami)	136
11	304-11H	0.070	25	7	JNES (Yamanaka)	136
12	304-12	-	25	11	JNES (Nishijima)	136
13	304-13	0.026	21	10	Jaske & O'Donnell	64
14	304-14	0.026	21	9	Jaske & O'Donnell	64
15	304-15	-	21	6	Jaske & O'Donnell	63
16	304-16	0.060	21	8	Jaske & O'Donnell	70
17	304-17	-	21	6	Jaske & O'Donnell	65
18	304-18	0.020	27	8	Jaske & O'Donnell	73
20	304-G	0.060	25, 260	9, 9 <sup>b</sup>	GE	14,15
21	304-A2	0.060	288	4	ANL	45
22	304-21, 21T	0.060	25, 325	2, 7	JNES (Kanasaki, Tsutsumi)	136

ANL Mat. ID	Material Heat Designation <sup>a</sup>	Carbon Content (wt.%)	Test Temperature (°C)	No. of Data Points	Source	Applicable Reference
23	304-32	0.070	300	3	JNES (Endo)	136
24	304-35	0.070	25, 289	8, <sup>c</sup> 5	JNES (Hirano)	136
26	304HP-1	0.050	25	6	JNES (Nishijima)	136
27	304HP-2	0.060	25	17, <sup>c</sup> 14 <sup>c,d</sup>	JNES (Nishijima)	136
28	304L-E	0.039	150,300	5, 11	Solomon	58-60
29	304L-1	0.017	25	5	JNES (Hirano)	136
30	304L-G	0.022	260	7	GE	14,15
31	304L	0.013	25	9	JNES (Suzuki)	136
<u>Type 316 Stainless Steels</u>						
32	316-1H	0.055	25, 290	7, 8	JNUFAD (Tokimasa)	210
33	316-2	0.050	25	6	JNES (Kaneo)	136
34	316-3H	0.040	25	6	JNES (Ikemoto)	136
35	316-4	0.060	21	4	Jaske & O'Donnell	63
38	316-7	-	21	8	Jaske & O'Donnell	61
39	316-8	-	22	3	Jaske & O'Donnell	61
40	316-9	-	21	5	Jaske & O'Donnell	61
41	316-10	-	21	4	Jaske & O'Donnell	61
42	316-12T, 25T	0.060	325, 25	7, 5	JNES (Kanasaki, Tsutsumi)	136
45	316-25, -25, -27T	0.040, 0.060	25, 325, 25	4, 6, 6	JNES (EFT, PLEX)	136
46	316-26T	0.057	25	10 <sup>e</sup>	JNES (EFT)	136
47	316-1H, 316L-1H	0.055, 0.015	25, 290	7, 7	JNES (Tokimasa)	136
48	316N-1	0.010	25, 288	25 <sup>b</sup> , 18 <sup>b</sup>	JNES (Yamauchi, Matsuno, Tokimasa)	136
50	316N-3H	0.012	25, 290	7, 7	JNES (Tokimasa)	136
51	316N-6	0.007	25	12	JNES (Higuchi)	136
52	316N-7	0.008	25, 290	25, 14	JNES (Utsunomiya, Nagata, Higuchi, Kanasaka, Ogawa)	136
53	316N-8	0.011	25, 289	5, 8	JNES (Hirano)	136
54	316N-A	0.013	22, 288, 320	12, 6, 3	ANL	45
<u>Stainless Steel Weld Metals</u>						
55	304HP-WM-1	0.058	25	7 <sup>d</sup> , 10	JNES (Nishijima)	136
56	304-WM-2	0.034	25	6	JNES (Kanasaki)	136
57	316-WM	0.020	25	6 <sup>f</sup>	JNES (EFT)	136
58	316N-WM-1	0.018	25, 290	13, 11	JNES (Ogawa, Nagata)	136
59	316N-WM-2	0.017	25, 289	10, 7	JNES (Hirano)	136
60	316N-WM-3	0.002	25	7	JNES (Kanasaki)	136
<u>Cast Austenitic Stainless Steels</u>						
61	CF-8M-1	0.053	325	12	JNES (Tsutsumi)	136
62	CF-8M-2	0.050	25	10	JNES (Hirano)	136
63	CF-8M-3	0.050	25	6	JNES (Kanasaki)	136
68	CF-8M-8	0.064	288	5 <sup>b</sup>	ANL	45
69	CF-8M-9	0.065	288	1 <sup>b</sup>	ANL	45

<sup>a</sup> The last letter at the end of the material heat designation refers to the following: H = hourglass specimens, T = tube specimens, and B = bending tests.

<sup>b</sup> Includes thermally aged specimens.

<sup>c</sup> Half the tests performed on hourglass specimens.

<sup>d</sup> Tests performed in axial load-control using a sinusoidal waveform.

<sup>e</sup> Five tests each performed on solid cylindrical specimens and tube specimens.

<sup>f</sup> Tests performed on tube specimens.

The fatigue  $\epsilon$ - $N$  data for Types 304, 304L, 316, and 316NG SSs in air at temperatures between room temperature and 400°C are shown in Fig. 38. The best-fit air curve based on the updated ANL fatigue life model (Eq. 29 in Section 3.2.6) and the mean-data air curve from ASME Code Section III prior to the 2009b Addenda are included in the plots in this figure. The results indicate that the fatigue lives of Types 304, 304L, and 316 SS are comparable and show excellent agreement with the ANL model with respect to the mean data air curve. The fatigue lives of Type 316NG are slightly higher than those for Types 304, 304L, and 316 SS at high strain amplitudes. However, all of the data are evenly distributed within the scatter band along the ANL mean air curve for austenitic SSs. Some of the tests on Type 316 SS in room-temperature air were conducted in load-control mode at stress levels in the range of 190–230 MPa. The data are shown as triangles in Fig. 38, with strain amplitudes of 0.1–0.12% and fatigue lives in the range of  $7 \times 10^4$  to  $3 \times 10^7$  cycles. For these tests, the strain amplitude was calculated only as elastic strain rather than also including the portion of the strain from plastic loading. When plastic strain was considered, based on cyclic stress-vs.-strain correlations for Type 316 SS,<sup>45</sup> actual strain amplitudes for these tests ranged from 0.23 to 0.32%. Therefore, these results were excluded from the analysis of the fatigue  $\epsilon$ - $N$  data to develop the model for estimating the fatigue lives of these steels in air so as not to interject an inconsistent bias in the evaluation.

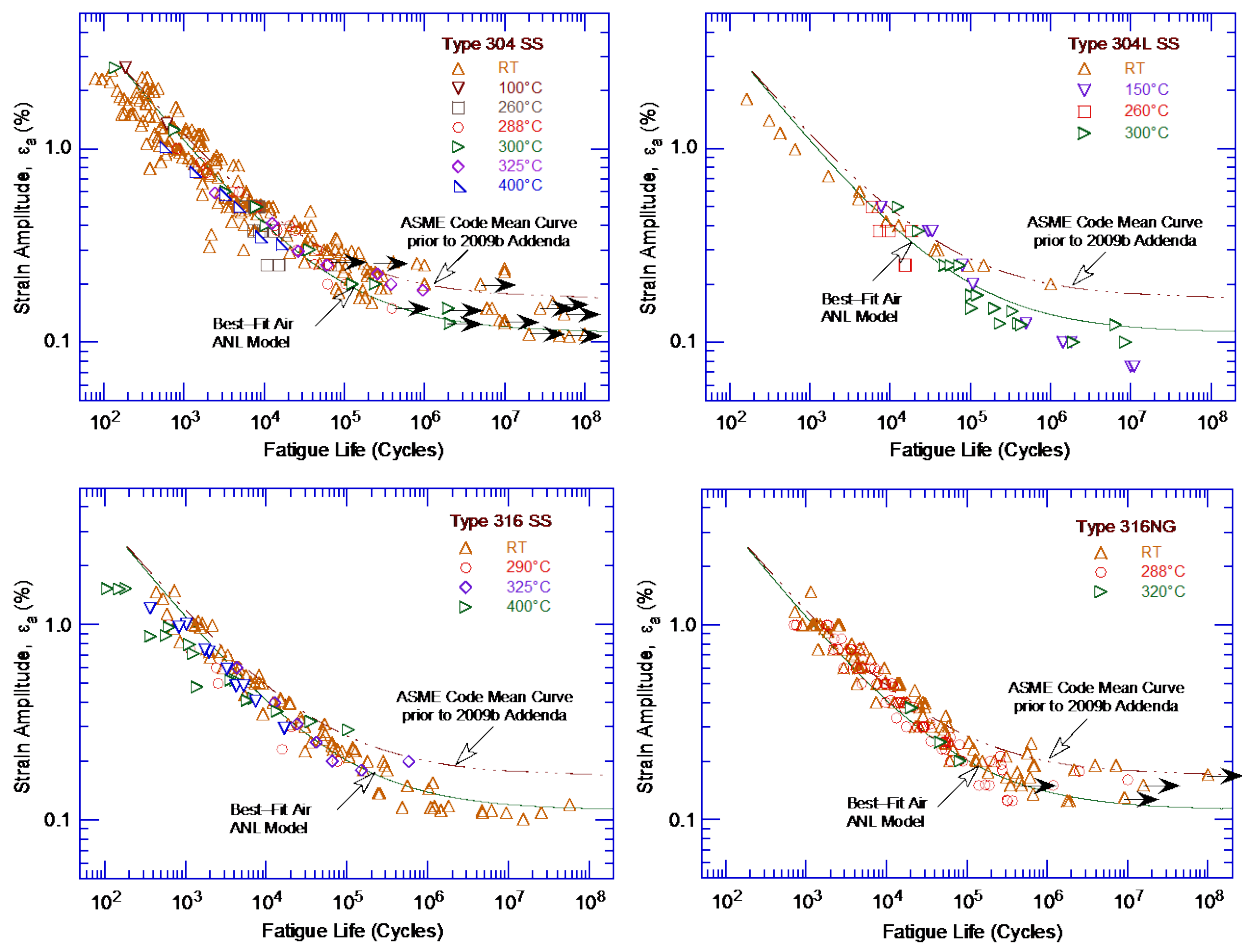


Figure 38. Fatigue  $\epsilon$ - $N$  behavior for Types 304, 304L, 316, and 316NG SS austenitic stainless steels in air at various temperatures up to 400°C (Refs. 13,42-47, 61,136).

The results in Fig. 38 indicated that the mean-data air curve in Section III of the ASME Code prior to the 2009b Addenda was not consistent with the existing fatigue  $\epsilon$ - $N$  data for austenitic SSs. At strain amplitudes less than 0.3% [stress amplitudes less than 585 MPa (84.9 ksi)], the ASME Code mean air curve predicted significantly longer fatigue lives than those observed experimentally for several heats of austenitic SSs with compositions and tensile strengths within the ASME specifications. The difference between the ASME Code Section III mean air curve and the best-fit of the available experimental data was caused by differences in the tensile strengths of the steels. The ASME Code Section III mean air curve represents SSs with relatively high tensile strengths; the fatigue  $\epsilon$ - $N$  data obtained during the last 30 years were obtained on SSs with lower tensile strengths. Furthermore, for the mean air curve from Section III of the ASME Code prior to the 2009b Addenda, the  $10^6$ -cycles fatigue limit (i.e., the stress amplitude at a fatigue life of  $10^6$  cycles) was 389 MPa, which is greater than the monotonic yield strength of austenitic SSs most commonly used (approximately 303 MPa). Consequently, the fatigue design air curve for austenitic SSs in Section III of the ASME Code did not include a mean stress correction for fatigue lives below  $10^6$  cycles. Studies by Wire et al.<sup>223</sup> and Solomon, et al.,<sup>58</sup> on the effects of residual stress on fatigue lives demonstrated that mean stress decreased the  $10^6$ -cycles fatigue limits of materials; the extent of these effects depended on the cyclic hardening behavior of the materials and the resultant decreases in strain amplitudes developed during load-controlled cycling. Strain hardening is more pronounced at high temperatures (e.g., 288-320°C) or at high mean stress values (e.g., greater than 70 MPa); therefore, as observed by Wire et al. and Solomon et al., fatigue lives for load-controlled tests with mean stress were actually increased at high temperatures or large values of mean stress. In both studies, under load controlled conditions, mean stress effects were observed at low temperatures (150°C) or at relatively low mean stress values (less than 70 MPa).

Wire et al.<sup>223</sup> performed fatigue tests on two heats of Types 304 SS to establish the effects of mean stress under both strain controlled and load controlled conditions. The strain-controlled tests indicated “an apparent reduction of up to 26% in strain-amplitude occurred in the low and intermediate cycle regime ( $<10^6$  cycles) for a mean stress of 138 MPa.” However, the results were affected by both mean stress and cold work. Although the composition and vendor-supplied tensile strengths for the two heats of Type 304 SS were within ASME Code specifications, the measured mechanical properties showed much larger variations than indicated by the vendor properties. Wire et al. stated, “at 288°C, yield strength varied from 152-338 MPa. These wide variations are attributed to variations in [cold] working from the surface to the center of the thick cylindrical forgings.” After separating the individual effects of mean stress and cold work, the Wire et al. results indicated a 12% decrease in strain amplitude for a mean stress of 138 MPa. These results were consistent with the predictions based on conventional mean stress models such as the Goodman correlation.

The current ASME Code Section III fatigue design air curve (i.e., 2009b Addenda or later editions of the ASME Code) is based on the ANL model presented in Eq. 29. This curve is consistent with the extensive fatigue  $\epsilon$ - $N$  data analyzed in this report. Additional details of the analysis are presented in Section 3.2.6.

- *The ASME Code Section III fatigue design air curve is now based on the ANL model and is consistent with the existing fatigue  $\epsilon$ - $N$  data for austenitic SSs.*

### 3.2.2 Specimen Geometry and Type of Loading

The influence of specimen geometry (hourglass vs. gauge length specimens) on the fatigue lives of Types 304 and 316 SS is shown in Fig. 39. At temperatures up to 300°C, specimen geometry had little or no effect on the fatigue lives of austenitic SSs; the fatigue lives of hourglass specimens were comparable to those of gauge specimens.

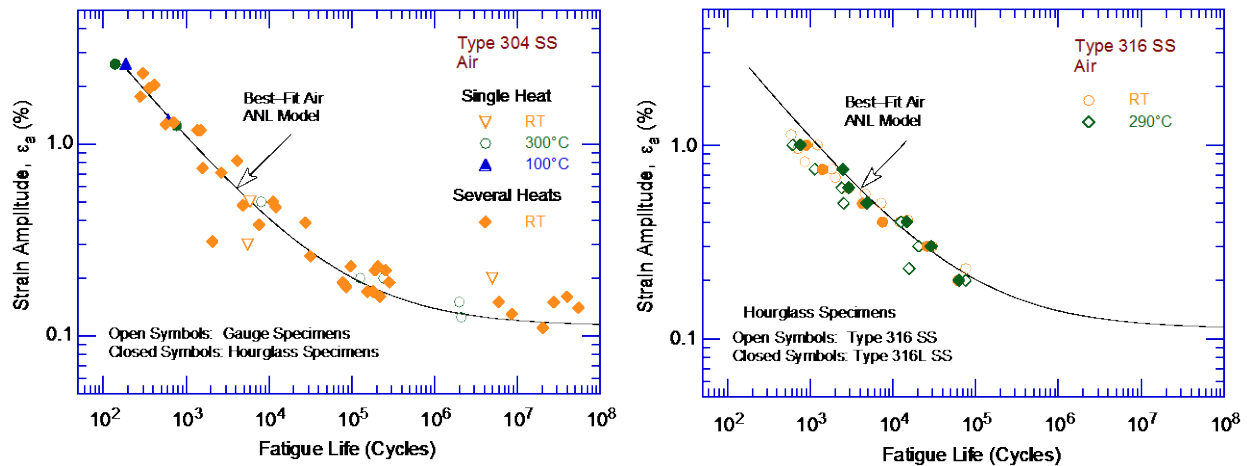


**Figure 39. Influence of specimen geometry on fatigue lives of Types 304 and 316 stainless steels (JNUFAD data).**

Figure 40 shows the results of strain-controlled bending fatigue tests tested on rectangular bar specimens of Type 304 SS in room-temperature air. Although all of the fatigue tests were performed at high strain amplitudes (i.e., producing fatigue lives less than  $10^4$  cycles), the bending-test data were evenly distributed along the ANL mean data air curve for austenitic SSs.

- *Fatigue  $\epsilon-N$  data obtained on hourglass specimens, straight gauge specimens, or bending test specimens may be used to develop the fatigue design air curves.*

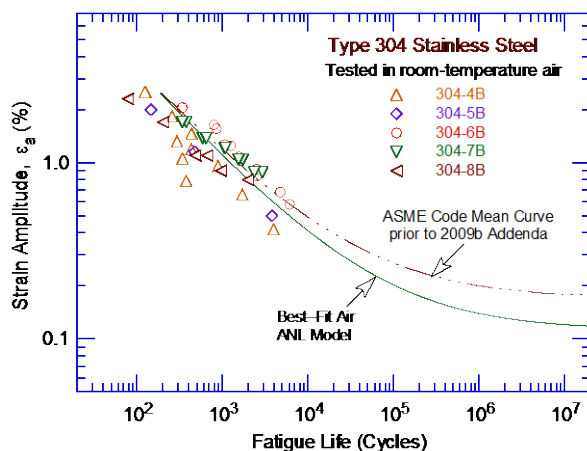


**Figure 40. Influence of bending loading on fatigue lives of Types 304 and 316 stainless steels (JNUFAD data).**

### 3.2.3 Strain Rate

A statistical analysis of the fatigue  $\epsilon$ - $N$  data presented in Ref. 45 indicated that the fatigue lives of austenitic SSs in an air environment decreased with decreasing strain rate at temperatures between 400 and 430°C. However, studies at EdF in France indicated that variations in strain rate in the range of 0.4–0.008%/s had no effect on the fatigue lives of SSs at temperatures up to 400°C.<sup>57</sup> Thus, for the fatigue data analysis presented in this report, strain rate effects on fatigue lives in air were considered insignificant.

- *Effects of strain rate on the fatigue lives of austenitic SSs in air were considered insignificant.*

### 3.2.4 Temperature

The fatigue lives of austenitic SSs in air at temperatures between room temperature and 400°C are plotted in Fig. 38. The results indicated that the fatigue lives of Types 304, 304L, 316, and 316NG SS did not show any dependence on temperature from room temperature up to 400°C. These results are consistent with the observation of Amzallag et al. (Ref. 57).

Additional fatigue data at temperatures between 427 and 456°C are plotted in Fig. 41.<sup>61-63</sup> The results indicated that the fatigue  $\epsilon$ - $N$  data at temperatures between 400 and 460°C were evenly distributed along the ANL best-fit air curve. Furthermore, for austenitic SSs, DSA is typically observed at temperatures of 500–600°C.<sup>206</sup> Therefore, based on these results, the fatigue  $\epsilon$ - $N$  data for austenitic SSs in air was represented by a single curve for temperatures from room temperature up to 450°C.

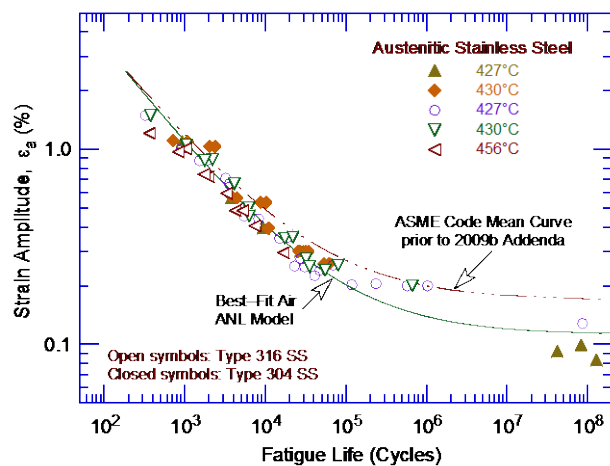


**Figure 41.**  
**Influence of temperature on fatigue lives of austenitic stainless steels in air (Ref. 61-63).**

However, studies at GE by Solomon et al. indicate that temperature influenced the fatigue limit of austenitic SSs because of differences in the secondary hardening behavior of the material.<sup>60</sup> Secondary hardening is the transformation of retained austenite to martensite causing an increase in hardness. This frequently occurs in high alloy steels due to precipitation of carbides during the tempering process. For a heat of Type 304L SS, the fatigue limit was higher at 300°C than at 150°C because of significant secondary hardening at 300°C.

- *Temperature had no significant effect on the fatigue lives of austenitic SSs in air at temperatures from room temperature up to 450°C. Variations in fatigue lives due to the effects of secondary hardening behavior were accounted for in the factor applied on stress that was applied to obtain the design air curve from the mean data air curve.*

### 3.2.5 Cyclic Strain Hardening Behavior

Under cyclic loading, austenitic SSs exhibited rapid hardening during the first 50–100 cycles; as shown in Fig. 42, the extent of hardening increased with increasing strain amplitude and decreasing temperature and strain rate.<sup>45</sup> The initial hardening was followed by a softening and saturation stage at high temperatures and by continuous softening at room temperature.

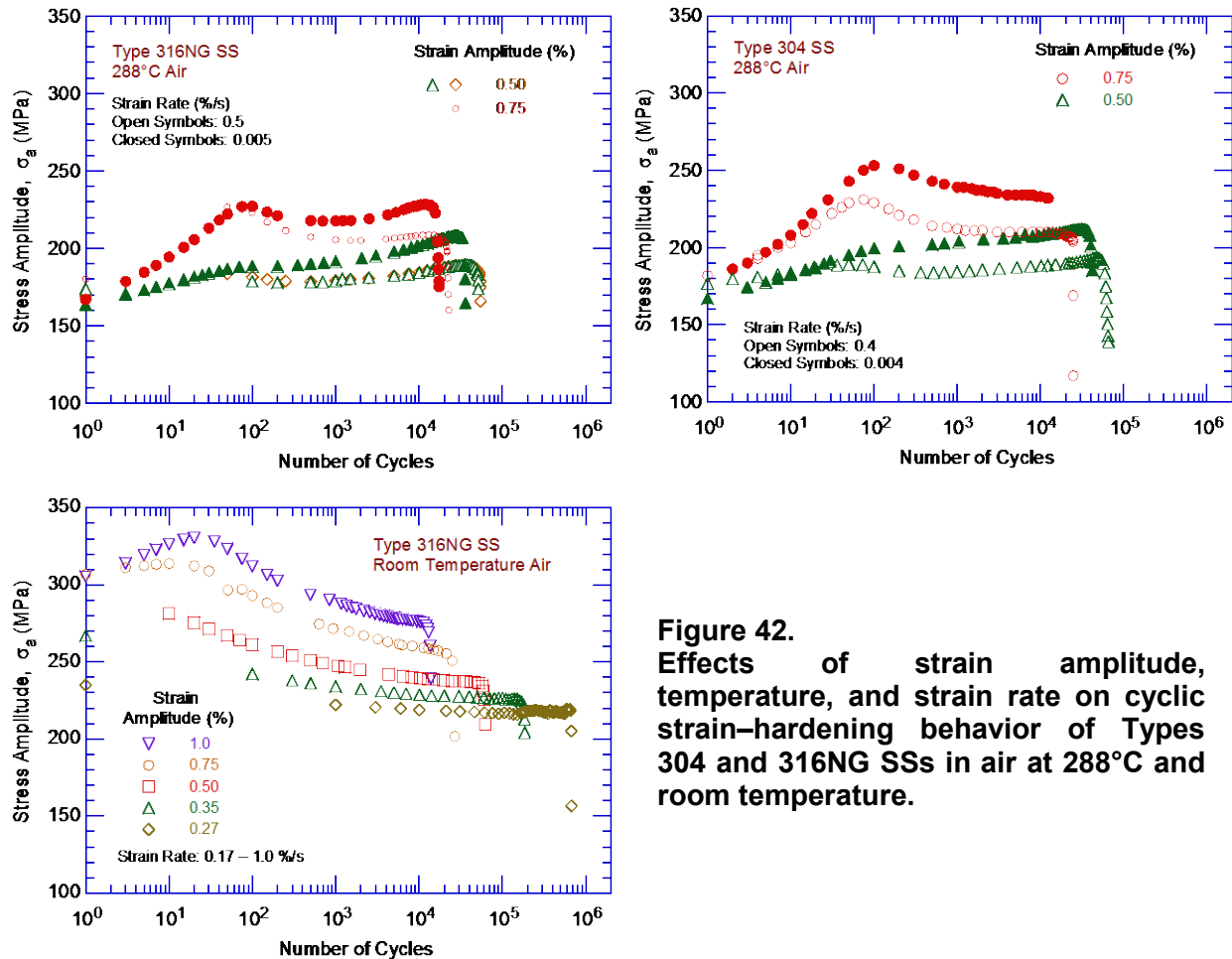


**Figure 42.** Effects of strain amplitude, temperature, and strain rate on cyclic strain-hardening behavior of Types 304 and 316NG SSs in air at 288°C and room temperature.

The cyclic stress–vs.–strain curves for Types 316, 304, and 316NG SS at room temperature and 288°C are shown in Fig. 43; cyclic stress corresponds to the value at half-life at a strain rate of 0.4%/s. For the various steels, cyclic stresses increased in magnitude in the following order: Types 316NG, 304, and 316.<sup>45</sup>

- *Cyclic strain hardening behavior influenced the fatigue lives of SS materials; variations in fatigue lives due to such effects were accounted for in the factor of 2 on stress that was applied to obtain the design air curve from the mean data air curve.*

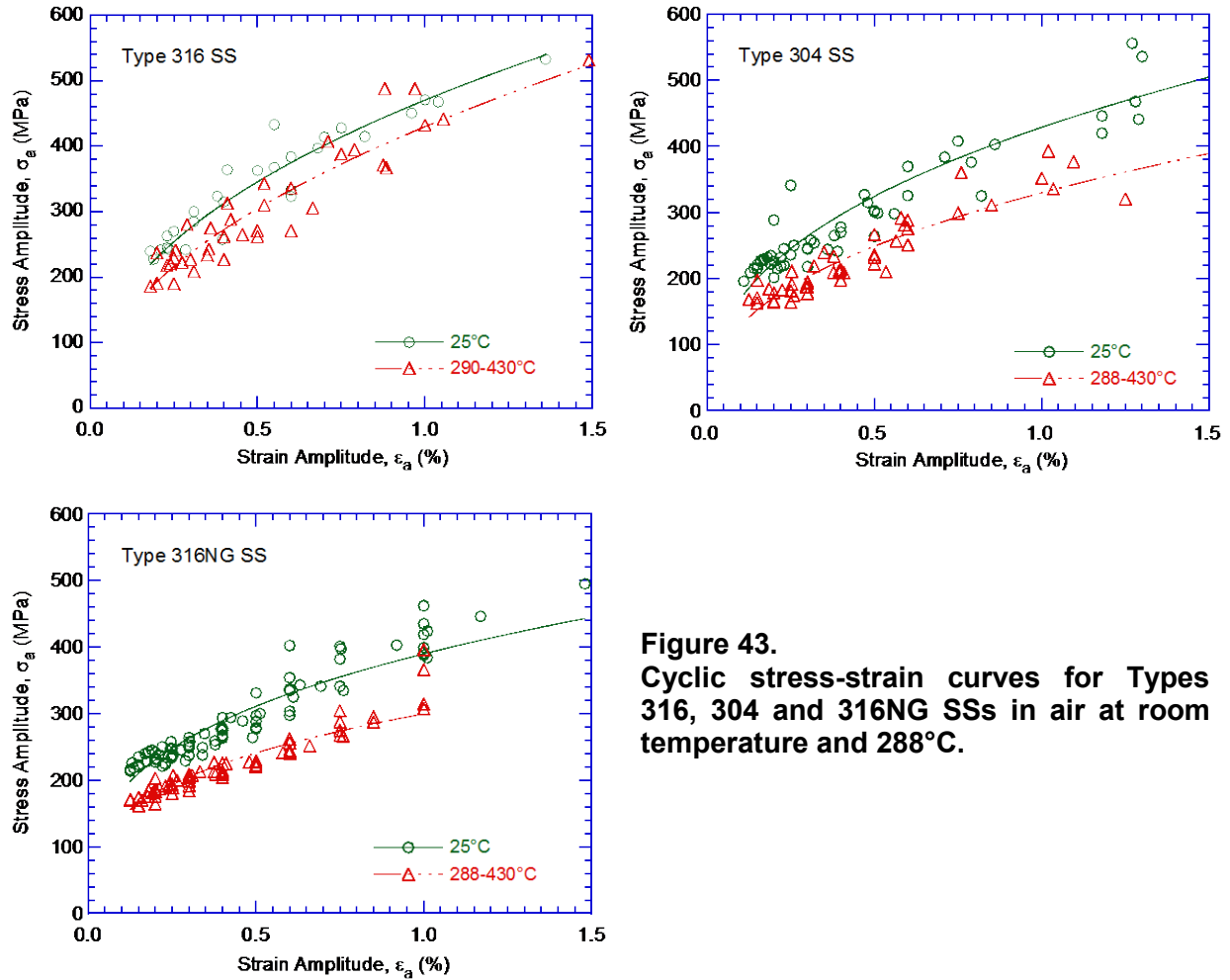


**Figure 43.**  
**Cyclic stress-strain curves for Types 316, 304 and 316NG SSs in air at room temperature and 288°C.**

### 3.2.6 Fatigue Life Model

In the initial revision of NUREG/CR-6909,<sup>137</sup> an updated version of the PVRC database was used to develop the best-fit mean air curve for austenitic SSs. The sources were listed in Table 1 of the report. The data were obtained on smooth specimens tested under strain-controlled conditions with fully reversed loading (i.e.,  $R = -1$ ) in compliance with consensus standard approaches used for the development of such data. The database consisted of 520 tests on Types 304, 316, 304L, 316L and 316NG SSs; approximately 220 of the tests were for Type 304 SS; 150 tests were for Type 316 SS; and 150 tests were for Types 316NG, 304L, and 316L SSs. The austenitic SSs used in these studies complied with the compositional and strength requirements of ASME Code specifications. The best-fit methodology described in Section 3.1.6 for carbon and low-alloy steels was also used for the analysis of the fatigue  $\epsilon$ - $N$  data for austenitic SSs.

Several different best-fit mean  $\epsilon$ - $N$  curves for austenitic SSs were previously proposed in the literature. Examples include Jaske and O'Donnell,<sup>61</sup> Diercks,<sup>224</sup> Chopra,<sup>45</sup> Tsutsumi et al.,<sup>34</sup> and Solomon and Amzallag.<sup>225</sup> These curves differ by up to 50%, particularly in the  $10^4$  to  $10^7$  cycles regime. The constant  $C$  in Eq. 6 (related to the fatigue limit of the material) varied from a value of 0.110 proposed by Tsutsumi and 0.112 by Jaske and O'Donnell to a value of 0.167 proposed in the original ASME Code Section III mean air curve. The differences primarily

occurred because different databases were used in developing these models for the mean  $\epsilon$ -N curves. The analyses by Jaske and O'Donnell and by Diercks were based on Jaske and O'Donnell's data.

Tsutsumi et al. used the JNUFAD data, which are included in the JNES database.<sup>136</sup> In the initial revision of NUREG/CR-6909, the updated PVRC data were analyzed to develop the ANL model for austenitic SSs; the updated PVRC data included the JNUFAD database. In addition, unlike the earlier ANL reports that proposed separate expressions for high-carbon and low-carbon grades of SSs, a single expression was developed for the fatigue  $\epsilon$ -N behavior of austenitic SSs. The model assumed that fatigue lives in air were independent of temperature and strain rate. Consistent with the models proposed by Tsutsumi<sup>34</sup> and by Jaske and O'Donnell,<sup>61</sup> the value of the constant C in the modified Langer equation (Eq. 6) was lower than that in earlier reports (i.e., 0.112 instead of 0.126). The proposed curve yielded an  $R^2$  value of 0.851 when compared with the updated PVRC data; the  $R^2$  values for the mean curves derived by Tsutsumi et al., Jaske and O'Donnell, and the ASME Code were 0.839, 0.826, and 0.568, respectively.

In air at temperatures up to 400°C, the fatigue lives for Types 304, 304L, 316, 316L, and 316NG SSs were represented by the expression:

$$\ln(N) = 6.891 - 1.920 \ln(\epsilon_a - 0.112) \quad (29)$$

where  $\epsilon_a$  is applied strain amplitude (%). The experimental values of fatigue lives and those predicted by Eq. 29 for austenitic SSs in air are plotted in Fig. 44. The predicted lives showed good agreement with the experimental values; for most tests, the differences between the experimental and predicted values were within a factor of 3. For some tests, the observed fatigue lives at low strain amplitudes (i.e., amplitudes that yielded fatigue lives greater than  $5 \times 10^4$  cycles) were significantly longer than the predicted values.

- *The ANL fatigue life model for austenitic SSs represents mean values of fatigue lives in air. The effects of parameters (such as mean stress, surface finish, size and geometry, and loading history) known to influence fatigue lives were accounted for in the factors of 12 on life and 2 on stress that were applied to the mean data air curve to obtain the fatigue design air curve.*

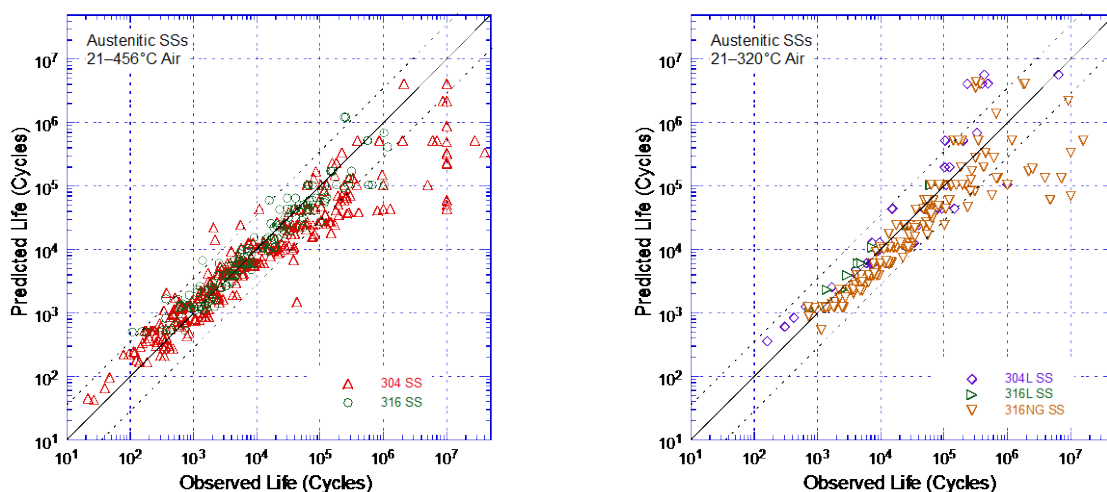


**Figure 44. Experimental and predicted fatigue lives (using the ANL model) for austenitic SSs in air.**

### 3.2.7 Heat-to-Heat Variability

The effects of material (heat-to-heat) variability and data scatter were included in the fatigue model to ensure that the design curves describe the available test data adequately, and adequately describe the fatigue lives of the much larger number of heats of materials found in the field compared to the limited numbers of heats tested in the laboratory. As mentioned earlier for carbon and low-alloy steels, heat-to-heat variability and data scatter in the fatigue  $\epsilon$ -N data for austenitic SSs were also evaluated by considering the best-fit curves determined from tests on individual heats of materials or loading conditions as samples of the much larger population of heats of materials and service conditions of interest. The fatigue lives of each of the heats or loading conditions were characterized by the value of the constant A in Eq. 6. The values of A for the various data sets were rank-ordered, and median ranks were used to estimate the cumulative distribution of A for the population. The distributions were fit to lognormal curves. The estimated cumulative distributions of constant A in the ANL model for fatigue lives of heats of wrought and cast austenitic SSs included in the initial revision of NUREG/CR-6909 and those included in this report are shown in Fig. 45. Note that the new updated database used in this report consisted of 622 data points; a significant increase (74%) compared to the 357 data points used in the initial revision of NUREG/CR-6909. The data were obtained on 5 types of austenitic SSs, 4 types of associated SS weld metals, and one type of cast austenitic SS. There are a total of 86 different heats of these materials.

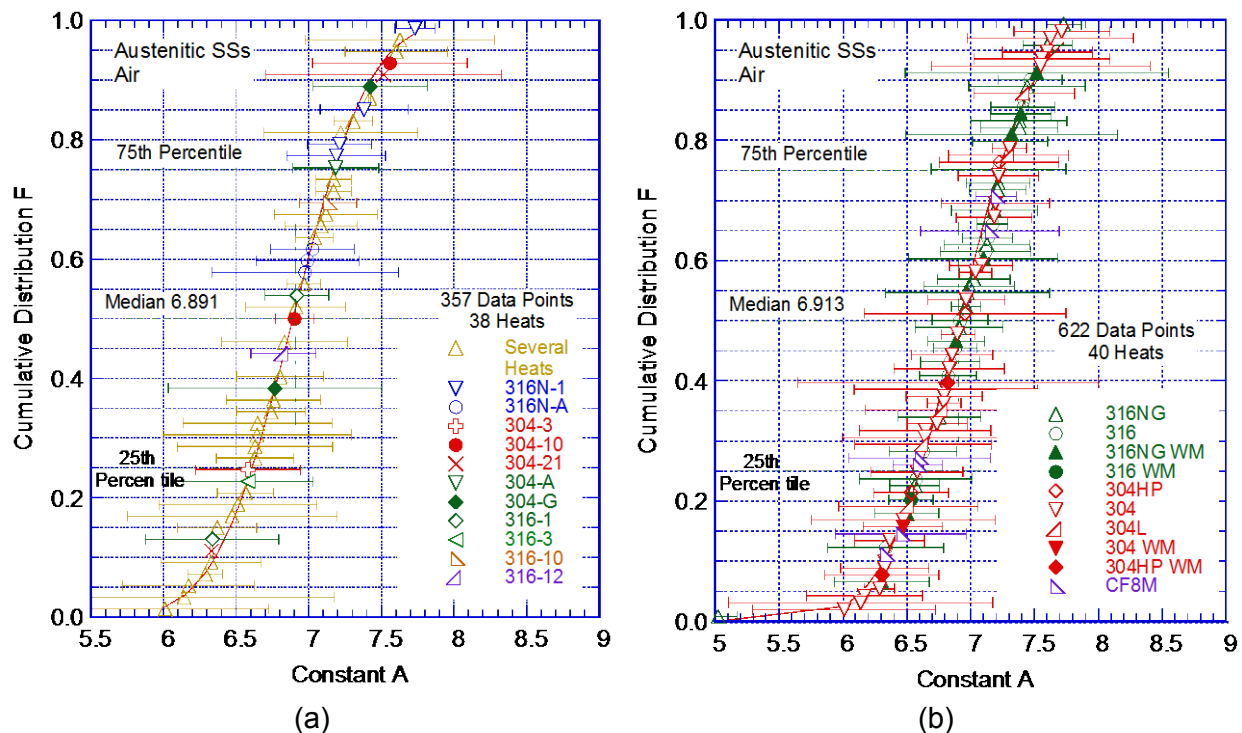


Figure 45. Estimated cumulative distribution of constant A in the ANL model for fatigue lives for heats of austenitic SSs in air included in (a) the initial revision of NUREG/CR-6909 and (b) those included in this report.

The results of the reanalysis indicated that the ANL fatigue model presented in the initial revision of NUREG/CR-6909 for predicting fatigue lives of austenitic SSs in air was adequate and remains representative of the updated (larger) database. Despite the significant increase in data, the reanalysis of the much larger updated database yielded an insignificant change in the median value of the constant A in Eq. 6. The constant A increased from 6.891 to 6.917. In

addition, Fig. 45 indicates that the various heats of wrought austenitic SSs and the associated SS weld metals were evenly distributed about the median value of constant A. The few heats of CF-8M cast austenitic SS were in the 15<sup>th</sup> – 30<sup>th</sup> percentile of the data, i.e., the fatigue lives of the heats of CF-8M were lower than the average values for austenitic SSs. However, this does not necessarily indicate that cast CF-8M materials have marginally lower fatigue lives than the average wrought SS material. This behavior is representative for this specific sample. Additional fatigue  $\epsilon$ -N data are needed on cast austenitic SSs to better establish the typical fatigue behavior of cast SS materials.

The values of the constant A that describe the 5<sup>th</sup> percentile of the statistical distributions produced a fatigue  $\epsilon$ -N curve that bounded the fatigue lives of 95% of the heats of austenitic SSs. A Monte Carlo analysis was performed to address the data uncertainties in the median value and standard deviation of the sample used for the analysis. For austenitic SSs, the values for A that provided bounds for the portion of the population and the confidence that was desired in the estimates of the bounds are summarized in Table 7. From Fig. 45, since the reanalysis did not change the constant A significantly, the median value of the constant A for austenitic SSs was not changed in this report. Thus, the median value of A for the sample remains 6.891. From Table 7, the 95/95 value of the factor to account for material variability and data scatter is 2.3 on life. This factor is needed to provide reasonable confidence that the resultant lives are greater than those observed for 95% of the SS materials of interest.

**Table 7. Values of constant A in the ANL fatigue life model for austenitic SSs and the factors on fatigue lives for austenitic SSs in air as a function of confidence level and percentage of population bounded.**

Confidence Level	Percentage of Population Bounded (Percentile Distribution of A)				
	95 (5)	90 (10)	75 (25)	67 (33)	50 (50)
	<u>Values of Constant A</u>				
50	6.205	6.356	6.609	6.707	6.891
75	6.152	6.309	6.569	6.668	6.851
95	6.075	6.241	6.510	6.611	6.793
	<u>Factors on Life</u>				
50	2.0	1.7	1.3	1.2	1.0
75	2.1	1.8	1.4	1.2	1.0
95	2.3	1.9	1.5	1.3	1.1

- *The mean data air curve for austenitic SSs used to develop the fatigue design air curve represented the average fatigue behavior; heat-to-heat variability was included in the subfactor that was applied to the mean data air curve to obtain the fatigue design air curve to account for “data scatter and material variability.”*

### 3.2.8 Fatigue $\epsilon$ -N Behavior of Cast Austenitic Stainless Steels

Available fatigue  $\epsilon$ -N data<sup>29,34,43,45</sup> indicated that the fatigue lives of cast CF-8M SSs in air were similar to those of wrought austenitic SSs. The fatigue  $\epsilon$ -N data for CF-8M cast austenitic SS in air, at temperatures between room temperature and 325°C, are plotted in Fig. 46. The results indicated that the fatigue lives of cast SSs were evenly distributed along the ANL best-fit curve for the mean data for wrought austenitic SSs.

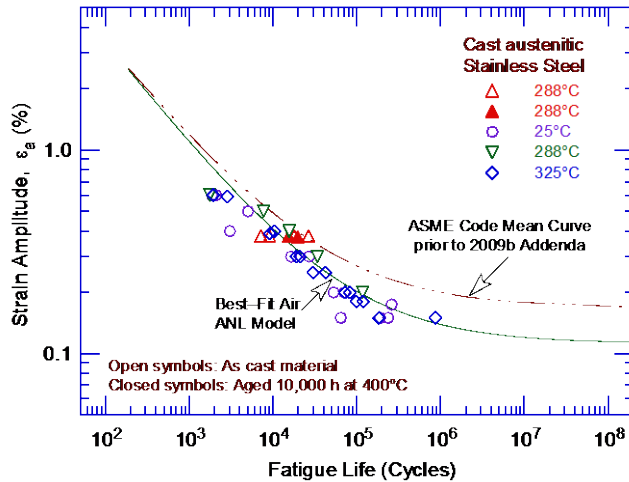


**Figure 46.** Fatigue  $\epsilon$ - $N$  behavior for several heats of CF-8M cast austenitic SSs in air at various temperatures.

The effects of thermal aging at 250–400°C on the fracture toughness properties of cast austenitic SSs are well established. Fracture toughness decreased significantly after thermal aging because of the spinodal decomposition of the ferrite phase to form a Cr-rich  $\alpha'$  phase.<sup>229-232</sup> The cyclic-hardening behavior of cast austenitic SSs was also influenced by thermal aging.<sup>45</sup> The spinodal decomposition of the ferrite phase during thermal aging at 400°C strengthened the ferrite phase and increased cyclic hardening. At 288°C, cyclic stresses of cast SSs aged for 10,000 h at 400°C were higher than for unaged material or wrought SSs. The existing data were too sparse to establish the effects of thermal aging on strain-rate effects on the fatigue lives of cast SSs in air.

- *The fatigue mean data air curve for wrought austenitic SSs may be used for cast austenitic SSs.*

### 3.2.9 Fatigue $\epsilon$ - $N$ Behavior of Weld Metals

Available fatigue  $\epsilon$ - $N$  data for Types 304, 340HP (i.e., high purity), 316, and 316NG weld metals in air at room temperature are plotted in Fig. 47. The results indicated that the fatigue lives of SS weld metals were slightly lower than the mean  $\epsilon$ - $N$  air curve for austenitic SSs in the low-cycle fatigue regime (i.e., fatigue lives less than  $10^4$  cycles), and generally longer in the high-cycle regime. However, the weld metal data were within the scatter band for the various grades and heats of austenitic SSs.

- *The limited fatigue  $\epsilon$ - $N$  air data indicate that the mean data air curve for wrought austenitic SSs may be used for SS weld metals.*

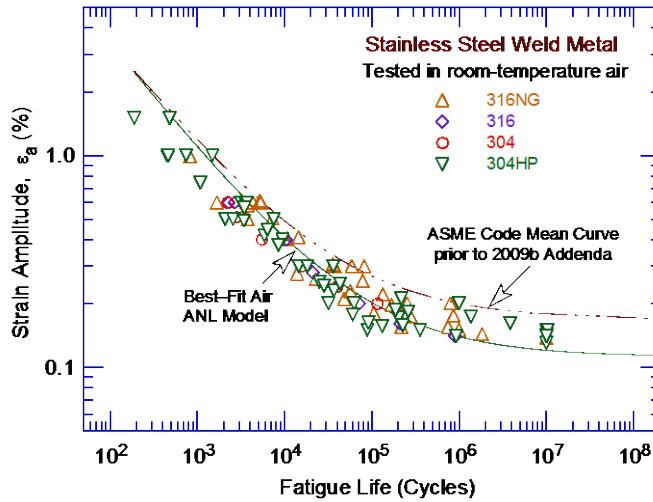


Figure 47. Fatigue  $\epsilon$ -N behavior for austenitic SS weld metals in air at room temperature.

### 3.2.10 Surface Finish

Fatigue tests were conducted on Types 304 and 316NG SS specimens that were intentionally roughened in a lathe, under controlled conditions, with 50-grit sandpaper to produce circumferential scratches with an average surface roughness of  $1.2 \mu\text{m}$ .<sup>46</sup> The results are shown for Types 316NG and 304 SS in Figs. 48a and b, respectively. For both steels, the fatigue lives of the roughened specimens were a factor of approximately 3 lower than those of the smooth specimens.

- *The effect of surface finish was included as part of the “surface finish and environment” subfactor that was applied to the mean data air curve to obtain the fatigue design air curve for austenitic SSs.”*

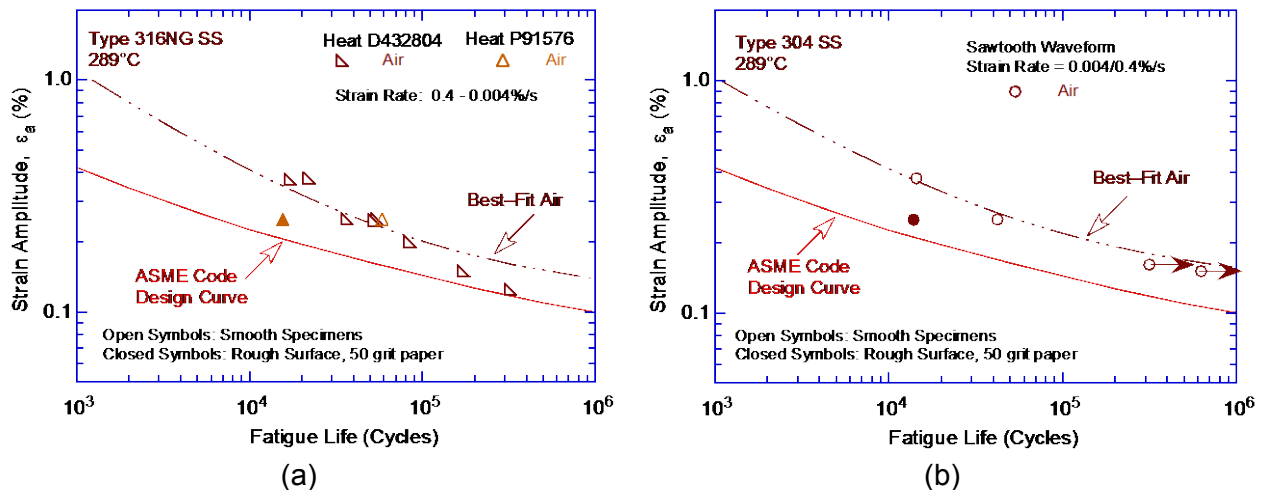


Figure 48. Effects of surface roughness on fatigue lives of (a) Type 316NG and (b) Type 304 SSs in air (Ref. 46).

### 3.2.11 Fatigue Design Curve

As discussed in Section 3.2.1, the ASME Code mean–data that were used to develop the current ASME Code Section III fatigue design air curve were not consistent with the existing fatigue  $\epsilon$ – $N$  data. Therefore, a fatigue design air curve that was consistent with the existing database was derived from the ANL model (Eq. 29) by following the same procedure that was used to develop the ASME Code Section III fatigue design air curve. The discussions presented in Section 5.5 indicated that the current ASME Code Section III requirement for a factor of 20 on cycles to account for the effects of material variability and data scatter, specimen size, surface finish, and loading history was conservative by at least a factor of 1.7. Therefore, to reduce this conservatism, an fatigue design air curve based on the ANL model for austenitic SSs (Eq. 29) was developed by correcting for mean stress effects using the modified Goodman relationship and then lowering the mean–stress–adjusted curve by a factor of 2 on stress and 12 on cycles, whichever was more conservative. The resulting fatigue design air curve and the fatigue design air curve in ASME Code Section III prior to the 2009b Addenda were presented in the original revision of NUREG/CR-6909. The two fatigue design air curves were identical beyond  $10^8$  cycles. In 2009, the new fatigue design air curve based on the ANL model for austenitic SSs was adopted into Mandatory Appendix I of Section III of the ASME Code. Both of the ASME Code Section III air fatigue design air curves are shown in Fig. 49, and the values of stress amplitude vs. cycles for the current and the proposed design air curves are given in Table 8. In 2005, a new fatigue design air curve was also proposed for austenitic SSs and Alloy 600 and 800 materials by the ASME Section III Subgroup on Fatigue Strength.<sup>125</sup>

- *A new fatigue design air curve for austenitic SSs that is consistent with the existing data was developed from the ANL model using factors of 12 on life and 2 on stress. This curve is the same as the ASME Code Section III fatigue design air curve implemented in 2009.*

**Table 8. The ASME Code fatigue design curves for austenitic SSs in air.**

No. of Applied Cycles	Stress Amplitude MPa (ksi)		No. of Applied Cycles	Stress Amplitude MPa (ksi)	
	ASME Code Design Curve	ASME Code Design Curve Prior to 2009		ASME Code Design Curve	ASME Code Design Curve Prior to 2009
1 E+01	6000 (870)	4881 (708)	2 E+05	168 (24.4)	248 (35.9)
2 E+01	4300 (624)	3530 (512)	5 E+05	142 (20.6)	214 (31.0)
5 E+01	2748 (399)	2379 (345)	1 E+06	126 (18.3)	195 (28.3)
1 E+02	1978 (287)	1800 (261)	2 E+06	113 (16.4)	157 (22.8)
2 E+02	1440 (209)	1386 (201)	5 E+06	102 (14.8)	127 (18.4)
5 E+02	974 (141)	1020 (148)	1 E+07	99 (14.4)	113 (16.4)
1 E+03	745 (108)	820 (119)	2 E+07		105 (15.2)
2 E+03	590 (85.6)	669 (97.0)	5 E+07		98.6 (14.3)
5 E+03	450 (65.3)	524 (76.0)	1 E+08	97.1 (14.1)	97.1 (14.1)
1 E+04	368 (53.4)	441 (64.0)	1 E+09	95.8 (13.9)	95.8 (13.9)
2 E+04	300 (43.5)	383 (55.5)	1 E+10	94.4 (13.7)	94.4 (13.7)
5 E+04	235 (34.1)	319 (46.3)	1 E+11	93.7 (13.6)	93.7 (13.6)
1 E+05	196 (28.4)	281 (40.8)	2 E+10		

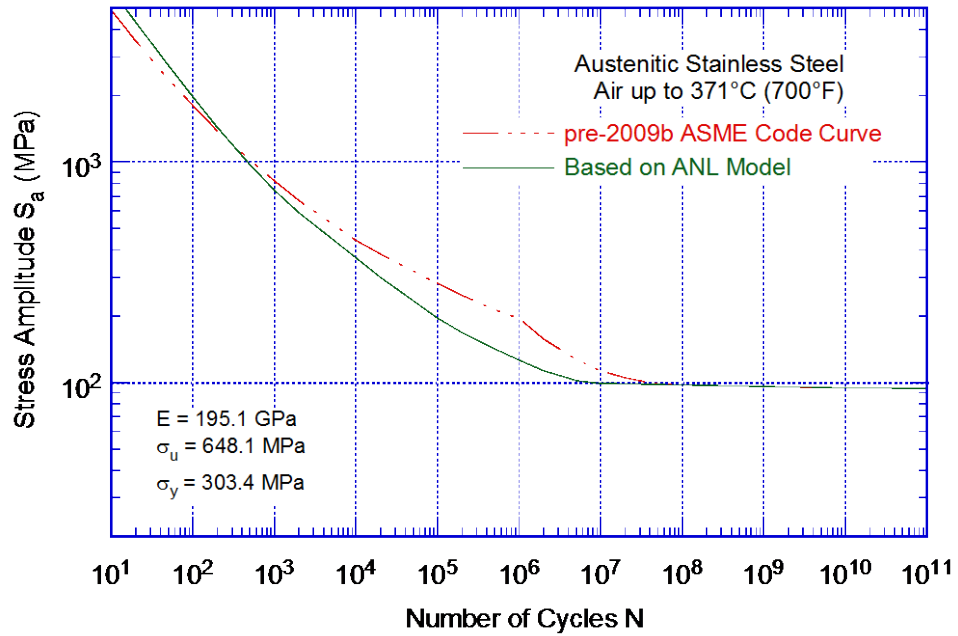


Figure 49. Fatigue design curves for austenitic SSs in air.

### 3.3 Ni-Cr-Fe Alloys and Weld Metals

The relevant fatigue  $\epsilon$ -N data for Ni-Cr-Fe alloys and their welds in air environments include the data compiled by Jaske and O'Donnell<sup>61</sup> for developing fatigue design criteria for pressure vessel alloys; the JNES database from Japan, which included studies at MHI, IHI, and Hitachi;<sup>39,136,210</sup> studies at Bettis Atomic Power Laboratory,<sup>70</sup> Knolls Atomic Power Laboratory,<sup>67,68</sup> NASA,<sup>73</sup> Battelle's Columbus Laboratories<sup>69</sup> and GE;<sup>14,71,72</sup> work sponsored by EPRI at Westinghouse Electric Corporation;<sup>66</sup> and the tests performed by Van Der Sluys et al.<sup>75</sup> The database was composed of 588 tests from which 559 data points were obtained; 191 data points for 17 heats of Alloy 600, 17 data points for 3 heats of Alloy 690, 23 data points for 2 heats of Alloy 800, 196 data points for 7 heats of Alloy 718; and 140 tests of Ni-Cr-Fe weld metals from which 132 data points were obtained for 1 heat of Alloy 690 weld metal, 5 heats of Alloy 82 weld metal, 4 heats of Alloy 182 weld metal, and 6 heats of other Ni-Cr-Fe weld metals. Out of these, 427 data points were obtained from tests conducted at room temperature, 40 data points were obtained from tests conducted at 260–316°C, and 92 data points were obtained from tests conducted at 427°C. A summary of the sources included in the updated database used for this report, as categorized by material type and test environment, is presented in Table 9. Other material information such as chemical composition, heat treatment, and room temperature tensile properties of these Ni-Cr-Fe alloys and associated weld metals is given in Appendix B.

**Table 9. Sources of the fatigue  $\epsilon$ -N data on Ni-Cr-Fe alloys and their weld metals in an air environment.**

ANL Mat. ID	Material Heat Designation <sup>a</sup>	Yield Strength (MPa)	Test Temperature (°C)	No. of Data Points	Source	Applicable Reference
<u>Alloy 600</u>						
1	Alloy 600-1	310	25	12	JNES (Higuchi)	136
2	Alloy 600-2	294	25	9	JNES (Nakao),	136
3	Alloy 600-3	-	25	6	JNES (Hirano),	136
4	Alloy 600-4	289	25	6	JNES (Hirano)	136
5	Alloy 600-5	264	25	11	JNES (Hirano)	136
6	Alloy 600-6	303	25	6	JNES (Kanasaki)	136
7	Alloy 600-7	253	24, 93, 204, 316	5, 5, 10, 7	KAPL (Dinerman)	67
8	Alloy 600-8	-	24	8 <sup>a</sup>	KAPL (Mowbray)	68
9	Alloy 600-9	-	24	10 <sup>a</sup>	KAPL (Mowbray)	68
10	Alloy 600-10	-	24	8 <sup>a</sup>	KAPL (Mowbray)	68
11	Alloy 600-11	-	24	13 <sup>a</sup>	KAPL (Mowbray)	68
12	Alloy 600-12	-	24	7 <sup>a</sup>	KAPL (Mowbray)	68
13	Alloy 600-13	-	24, 316	9, 9	EPRI (Jacko)	66
14	Alloy 600-14	-	21	19	Bettis (McGowan&Faber)	70
15	Alloy 600-15	386	260	6	GE (Hale)	14
16	Alloy 600-16	-	21	15	Jaske & O'Donnell	61
17	Alloy 600-17	-	24, 83	5, 5	Jaske & O'Donnell	61
<u>Alloy 690</u>						
20	Alloy 690-1	280	25	6	JNES (Kanasaki)	136
21	Alloy 690-2	-	25	5	PVP (Higuchi)	39
22	Alloy 690-3	-	315	6	PVP (Van der Sluys)	75
<u>Alloy 800</u>						
25	Alloy 800-1	-	21	7	BMI (Jaske et al.)	69
26	Alloy 800-2	-	427	6, 10	BMI (Jaske et al.), GE (Conway)	69,71
<u>Alloy 718</u>						

ANL Mat. ID	Material Heat Designation <sup>a</sup>	Yield Strength (MPa)	Test Temperature (°C)	No. of Data Points	Source	Applicable Reference
30	Inconel 718-1	-	21	18	ASME Data File	210
31	Inconel 718-2	-	21	4	J. Miller (J of Mat.)	72
32	Inconel 718-3	-	24, 427	17, 31	ASME Data File	61
33	Inconel 718-4	-	24, 427	30, 10	ASME Data File	61
34	Inconel 718-5	-	21, 427	34, 4	ASME Data File	61
35	Inconel 718-6	-	27, 427	12, 8	ASME Data File, NASA (Natchigall)	61,73
36	Inconel 718-7	-	22, 427	5, 23	ASME Data File	61
<u>Ni-Cr-Fe Alloy Weld Metals</u>						
38	Alloy 690 WM	431	25	6	JNES (Kanasaki)	136
39	Alloy 62	-	24	9 <sup>a</sup>	KAPL (Mowbray)	68
40	Alloy 82-1	-	24	8 <sup>b</sup>	KAPL (Mowbray)	68
41	Alloy 82-2	-	24	8 <sup>a</sup>	KAPL (Mowbray)	68
42	Alloy 82-3	-	24	17 <sup>a</sup>	KAPL (Mowbray)	68
43	NiCrFe WM-1	-	24	9	Higuchi, Iida	SGFS 1988
44	Arcaloy 8N12	-	24	6 <sup>a</sup>	KAPL (Mowbray)	68
45	NiCrFe WM-2	-	25	9, 5	JNUFAD (Higuchi, Nakao)	210
46	Alloy 82-4	322	260	7	KAPL (Mowbray)	68
47	Alloy 182-1	-	25	13	PVP (Higuchi)	39
48	Alloy 182-2	456	290	7	JNES (Higuchi)	136
49	Alloy 182-3	405	25	5	JNES (Nakao)	136
50	Alloy 182-4	409	25	6	JNES (Kanasaki)	136
51	Alloy 82-5	339	315	5	PVP (Van der Sluys)	75
52	Alloy 152	-	25	6	PVP (Higuchi)	39
53	Alloy 132	-	25	6	PVP (Higuchi)	39

<sup>a</sup> Tests performed under bending fatigue.

<sup>b</sup> Six tests performed under bending fatigue and four under rotating bending.

### 3.3.1 Experimental Data

The fatigue  $\epsilon$ - $N$  data for Alloys 600, 690, and 800 in air at temperatures between room temperature and 427°C are shown in Fig. 50, and those for Alloys 62, 82, 132, 152, 182, and other Ni-Cr-Fe alloy weld metals in air at temperatures between room temperature and 315°C are shown in Fig. 51. The fatigue  $\epsilon$ - $N$  data for Inconel 718 in air at room temperature and 427°C is shown in Fig. 52. Fatigue CUF evaluations for Ni-Cr-Fe alloy components were performed using the fatigue design air curve for austenitic SSs because there is not a separate curve for Ni-Cr-Fe materials in Section III of the ASME Code. Therefore, the best-fit air curve for austenitic SSs based on the ANL model (Eq. 29 in Section 3.2.6) is included in these three figures. The results indicate that, although the data for Alloys 690 and 800 are limited, the fatigue lives of these alloys were comparable to those of Alloy 600 (Fig. 50). The fatigue  $\epsilon$ - $N$  data for Ni-Cr-Fe alloy weld metals indicated that the fatigue lives of the various weld metals were comparable, although the data for Alloy 82 at 260 to 315°C showed significant scatter

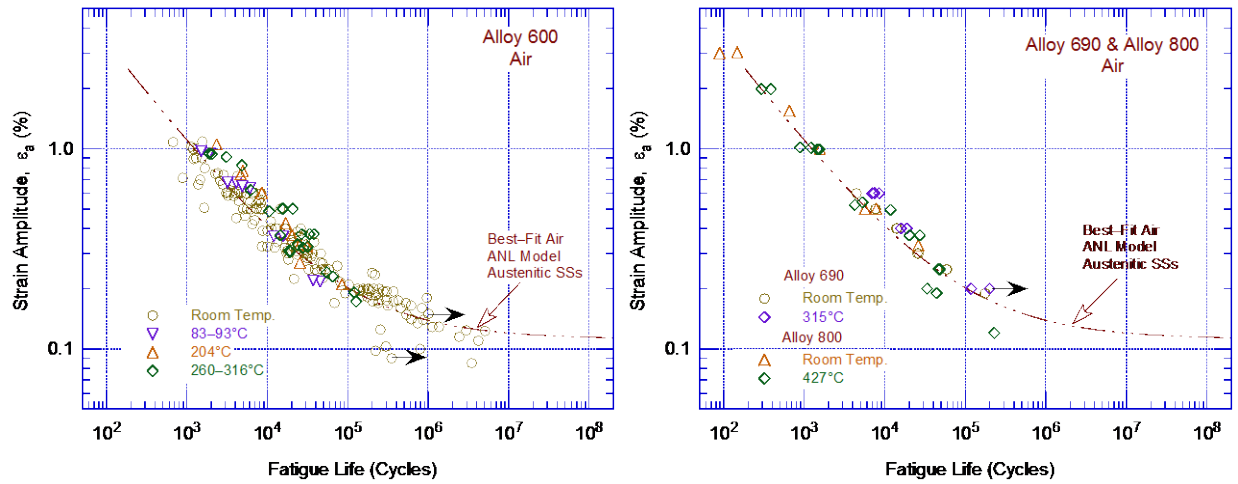


Figure 50. Fatigue  $\epsilon$ -N behavior for Alloys 600, 690 and 800 in air at temperatures between room temperature and 315°C (Refs. JNUFAD data, 61,66-75).

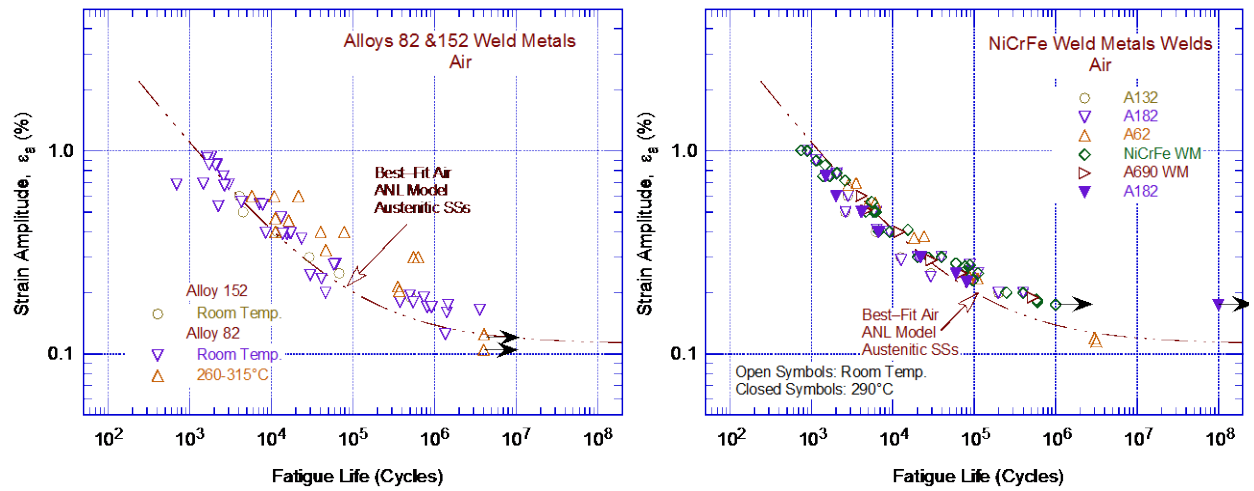


Figure 51. Fatigue  $\epsilon$ -N behavior for Alloys 62, 82, 132, 152, and 182 welds in air at various temperatures (Refs. JNUFAD data, 61,66-75).

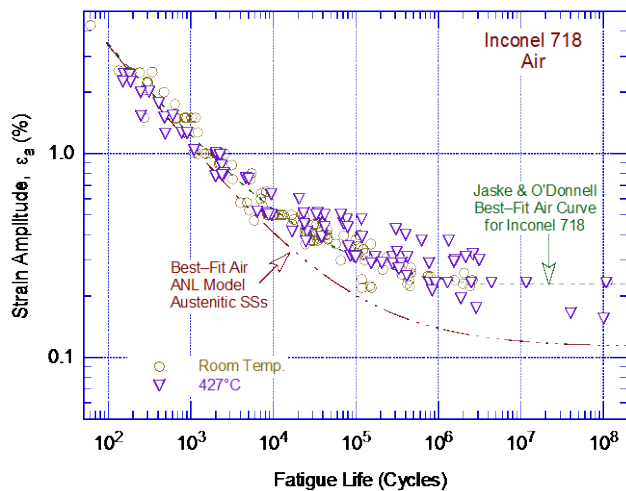


Figure 52. Fatigue  $\epsilon$ -N behavior for Inconel 718 in air at room temperature and 427°C (Refs. 61,72,73,136,210).

(Fig. 51). The fatigue lives of the Ni-Cr-Fe alloy weld metals were comparable to those of the wrought Alloys 600 and 690 in the low-cycle regime (i.e., less than  $10^5$  cycles) and were slightly superior to the lives of wrought materials in the high-cycle regime. The results also indicated that the fatigue limit for the weld metals was higher than that for wrought materials. Overall, the available fatigue  $\epsilon$ - $N$  data indicated that the fatigue lives of Ni-Cr-Fe alloys was represented by the fatigue design air curve for austenitic SSs; however, fatigue evaluations for Ni-Cr-Fe weld metals were conservative under this assumption.

The fatigue  $\epsilon$ - $N$  data in Fig. 52 indicate that the fatigue lives of Inconel 718 were longer than those for austenitic SSs or other Ni-Cr-Fe alloys and their weld metals, particularly at strain amplitudes less than 0.5% (i.e., in the high-cycle regime). The fatigue limit for Inconel 718 was much higher than that of austenitic SSs. Therefore, fatigue analyses for Inconel 718 that used the fatigue design air curve for austenitic SSs yielded conservative estimates of fatigue usage. To avoid this conservatism, a separate fatigue design air curve is appropriate for Inconel 718. Jaske and O'Donnell proposed the following expression for fatigue lives of Inconel 718 in air,

$$\ln(N) = 6.859 - 2.0 \ln(\epsilon_a - 0.210). \quad (30)$$

The Jaske and O'Donnell best-fit air curve for Inconel 718 is also shown in Fig. 52.

The available fatigue  $\epsilon$ - $N$  data for Ni-Cr-Fe alloys also indicated that, unlike austenitic SSs that do not show temperature dependencies of fatigue lives under LWR operating conditions, the fatigue lives of Alloy 600 were generally longer at high temperatures compared to those at room temperature, particularly for Alloy 82 weld metal (Fig. 51a).<sup>66-68</sup> A similar behavior was observed for Inconel 718 (Fig. 52). However, limited data for Alloy 690 (Fig. 50b) and Alloys 62, 132, 182, and 690 weld metals (Fig. 51b), indicated little or no effects of temperature on their fatigue lives. The existing data were insufficient to adequately determine the effect of strain rate on the fatigue lives of Ni-Cr-Fe alloys.

Overall, the results indicated that the best-fit mean air curve for austenitic SSs represented slightly conservative estimates of the fatigue lives for Ni-Cr-Fe alloys in the high-cycle regime (fatigue lives greater than  $5 \times 10^4$  cycles), particularly for Ni-Cr-Fe alloy weld metals. However, the best-fit mean data curve for austenitic SSs yielded very conservative estimates of fatigue lives for Inconel 718 for fatigue lives greater than  $10^4$  cycles. To reduce this conservatism, the fatigue behavior of Inconel 718 should be represented by a separate fatigue  $\epsilon$ - $N$  curve.

- *For Ni-Cr-Fe alloys and their welds, the ANL fatigue life air model proposed in this report for austenitic SSs (Eq. 29) was either consistent or conservative with respect to the fatigue  $\epsilon$ - $N$  data.*

### 3.3.2 Fatigue Life Model

For Ni-Cr-Fe alloys, fatigue evaluations are based on the fatigue design air curve for austenitic SSs because there is not a separate curve for Ni-Cr-Fe materials in Section III of the ASME Code. However, the rather limited fatigue  $\epsilon$ - $N$  data for Ni-Cr-Fe alloys (such as Alloys 600, 690, and 800 and their welds) were consistent with the best-fit mean air curve for austenitic SSs for fatigue lives less than  $10^4$  cycles. The data also showed longer fatigue lives than the estimated values for fatigue lives greater than  $10^4$  cycles. The data were comparable or slightly conservative with respect to the ANL model for austenitic SSs, e.g., Eq. 29. Estimates of the cumulative distribution of Constant A in the fatigue  $\epsilon$ - $N$  curve for the various heats of Alloys 600, 690, and 800, and their associated weld metals, yielded a median value of 7.129. This value was slightly greater than the value of Constant A derived for austenitic SSs. In other

words, the fatigue lives of these Ni-Cr-Fe alloys were approximately 25% greater than those for austenitic SSs. Based on these findings, the current ASME Code Section III fatigue design air curve for austenitic SSs, which is the same as the ANL model presented in Fig. 49 and Table 8, adequately represented the fatigue  $\epsilon$ -N behavior of Ni-Cr-Fe alloys and their welds.

However, the fatigue design air curve for austenitic SSs yielded very conservative estimates of fatigue lives for Inconel 718. A detailed analysis of the cumulative distribution of Constant A for the various data sets available for Inconel 718 was not performed because the Constants B (the slope of the curve) and C (the constant associated with the fatigue limit) in the fatigue  $\epsilon$ -N curve were significantly different than those for austenitic SSs. For Inconel 718, the slope of the fatigue  $\epsilon$ -N curve was flatter and the fatigue limit (i.e., fatigue life at  $10^6$  cycles) was higher.

- *The ASME Code Section III fatigue design air curve for austenitic SSs, which is the same as the ANL air model for austenitic SSs, may also be used for Ni-Cr-Fe alloys and their welds. The current design fatigue air curve for austenitic SSs yielded conservative estimates of fatigue lives for Inconel 718.*

